PhD-FSTM-2023-017
The Faculty of Science, Technology and Medicine

DISSERTATION

Defence held on 11/01/2023 in Esch-sur-Alzette

to obtain the degree of

DOCTEUR DE L'UNIVERSITÉ DU LUXEMBOURG

EN CHIMIE

by

Nicolas BELLOMO
Born on 31 January 1992 in Ottignies-Louvain-la-Neuve (Belgium)

REMOTE PLASMA CHEMICAL VAPOUR DEPOSITION FOR GAS DIFFUSION LAYER AND PROTON EXCHANGE MEMBRANE SYNTHESIS FOR FUEL CELLS

Dissertation defence committee

Dr Marc Michel, dissertation supervisor
Doctor, Luxembourg Institute of Science and Technology
Dr Andreas Michels, Chairman
Professor, Université du Luxembourg
Dr Stéphanie Roualdès-Boutevin
Maitre de conférences, Université de Montpellier 2
Dr Vincent Ball
Professor, Université de Strasbourg
Dr Jérôme Polesel
Doctor, Luxembourg Institute of Science and Technology
Dr Renaud Leturcq
Doctor, Luxembourg Institute of Science and Technology

TABLE OF CONTENTS

Chapter III Prototype design for proton exchange membrane deposition

GENERAL INTRODUCTION

This manuscript summarizes the work that has been accomplished during the last four years and is declined into three chapters. The first chapter talks about the literature review and state of the art before entering the description of the work that has been done with the deposition of perfluorinated films for gas diffusion layer applications, in the second chapter, and a prototype design for proton exchange membrane deposition in the third chapter.

This first chapter aims at giving a general outlook of the context in which the present thesis took place. Several topics have been investigated and are discussed throughout this work.

In the first chapter we discuss the circular economy based on hydrogen, chemical vapour deposition (CVD), gas diffusion layers (GDL), proton exchange membrane fuel cells (PEMFC) which are essential topics to understand the work that has been accomplished since the start of this PhD cycle in 2018.

The hydrogen circular economy is the starting point and talks about the context of climate change and the drastic changes that our society needs to manage in order to reduce the impact of the human race on the environment, the objective set by the European union, how hydrogen can be incorporated in our society to reduce greenhouse gases emission. In the scientific field, researchers are focusing on improving the various component of the devices used to make the hydrogen economy a reality as well the means of component production.

In this context the PhD was oriented toward the synthesis of material via chemical vapour deposition (CVD). CVD's are convenient techniques to produce solid materials that can easily be scaled up. The first chapter gives an outlook about CVD's. We give a specific attention to plasma CVD's and remote plasma processes. In this thesis we used remote plasma CVD to produce elaborated gas diffusion layers and proton exchange membranes which are components of paramount importance in fuel cells.

We move on to discuss gas diffusion layers for proton exchange membrane fuel cells (PEMFC) which are essentials for the proper running of PEMFC. This part is subdivided in three parts, focusing on the support of diffusion, the treatments of the support of diffusion and the microporous layer.

And the last part of the first chapter discusses fuel cells which are devices that convert the chemical energy of hydrogen into electrical energy and find a large array of applications to power our society. Other devices exist also based on hydrogen but will not be extensively discussed in this work. A specific focus is given on proton exchange membranes synthesized via chemical vapour deposition.

The second chapter relates to the elaboration of efficient gas diffusion layers for fuel cell applications. A specific piece of chemical vapour deposition machinery called PRODOS was used for this purpose. With this machine and CVD technique we developed a know-how on how to deposit perfluorinated material with tuneable hydrophobic and crystalline properties. Tetrafluoromethane (CF_4) and methane (CH_4) activated via remote plasma were used to achieve the present results of this thesis. This chapter is divided in two parts, the first one relates to the deposition of thin films on silicon wafers for the study of physico-chemical properties of the deposited material while the second part relates to the hydrophobization of commercial carbon cloths for application as gas diffusion layer in fuel cells. Ten films were produced with varying deposition process parameters such as plasma power, CF_4/CH_4 ratio, and substrate temperature to investigate the physico-chemical properties. We then proceeded to characterize them using water contact angle to study hydrophobicity, step height profilometry (measurement of the films thicknesses), atomic force microscopy to investigate films roughness's, scanning electron microscopy to image the deposition morphologies, X-ray photoelectron spectrometry to investigate the films elemental composition and X-ray diffraction for the study of crystallinity. This first part gives an interesting insight of the depositions with one sample in particular that has peculiar crystalline and hydrophobic properties. Later on, two sets of deposition parameters were selected to be deposited on carbon cloth as support of diffusion. These carbon cloths with depositions were characterized with regard to gas diffusion layer properties and application and a characterization methodology has been developed. Characterizations include scanning electron microscopy to investigate the films morphology when deposited on carbon cloths, helium ion microscopy with secondary ion mass spectrometry to visualize the films wrapped around the carbon cloths, environmental scanning electron microscopy to visualize the behaviour of water on the carbon cloths, fuel cell testing in test bench with reference membrane electrode assembly to study the behaviour of a fuel cell with our gas diffusion layers and conductive atomic force microscopy to map the conductivity of the carbon cloth with the depositions. Interesting results with important correlations between them are found.

In the third chapter we describe the setting up of a prototype CVD tool developed during the course of this PhD and the results associated with it regarding the synthesis of proton exchange membranes. Initially, the project was focusing on the synthesis of such materials using the PRODOS via the copolymerization of a CF_4/CH_4 gas mixture with Perfluoro(4-methyl-3,6-dioxaoct-7-ene)sulfonyl fluoride (PSEPVE). Unfortunately, this approach has always been unsuccessful due to the limitations of the PRODOS system. In order to overcome these limitations and the inability of the PRODOS to copolymerize the dually injected species, a prototype was set up based on the PRODOS itself. In the third chapter we describe the evolution of the setting up of the prototype to replace the PRODOS for

the synthesis of proton exchange membranes. Various versions were set up in an evolutive way based on the results obtained with one version and the other. The objective pursued to assess the relevance of a prototype version is the copolymerization of perfluoro(3-oxapent -4-ene) sulfonyl fluoride (also abbreviated PSVE) and hexafluoro-1,3- butadiene (HFBD). This last chapter focuses on the design of a prototype, the characterization of the films is not deeply investigated. Characterizations of the gaseous phase with optical emission spectroscopy, XPS and TOF-SIMS characterization of the films, were used to improve the prototype until a third and last upgrade was finally obtained with extremely promising perspectives.

Chapter I

Literature review and state of the art

1 THE HYDROGEN CIRCULAR ECONOMY

1.1 A LONG-AWAITED TECHNOLOGY PARADIGM

The potential of hydrogen is not new, industries have been producing it on large scale ever since 1920 for ammonia synthesis which was used in the manufacturing of explosives and fertilizers[1]. But hydrogen can also be used to convert chemical energy into electrical energy in devices called "fuel cells". Back in the 1800s, Sir William Groove conceptualized the first fuel cell by combining hydrogen and oxygen to produce electricity, that point in history is considered to be the starting point of these technologies[2]. Further development continued in the 20th century, but it is only in 1959 that Francis Thomas Bacon demonstrated the first fully operational fuel cell, efficient enough to be licensed and adopted by NASA in particular to be used in the 1960s as part of the Gemini and Apollo manned space programs[3]. A large-scale conception of hydrogen implemented as an ecologically clean energy system arose in the 1970s as response from the scientific community to the increasing scarcity of resources of hydrocarbon fuel (oil, gas and coal) and the energy crisis of that period[4].

Many factors can account for the delay in the implementation of large hydrogen use in our society. The first one would be the safety issues associated with it in the light of the Hindenburg zeppelin disaster in 1937. Hydrogen being highly flammable (ignition can occur with a volumetric ratio of 4% in air)[5] general public opinion, politics and industrials have always been hesitant about it due to the potential hazards.

A second concern is the storage of hydrogen. While standard fuels such as diesel and gasoline have a high volumetric energy density and low gravimetric energy density, hydrogen is the other way around and needs to be stored under high pressure or in its liquid form to be used (see figure 1). Hence, hydrogen is a light fuel but can require large tanks which can be problematic for portable devices use or to fuel cars.

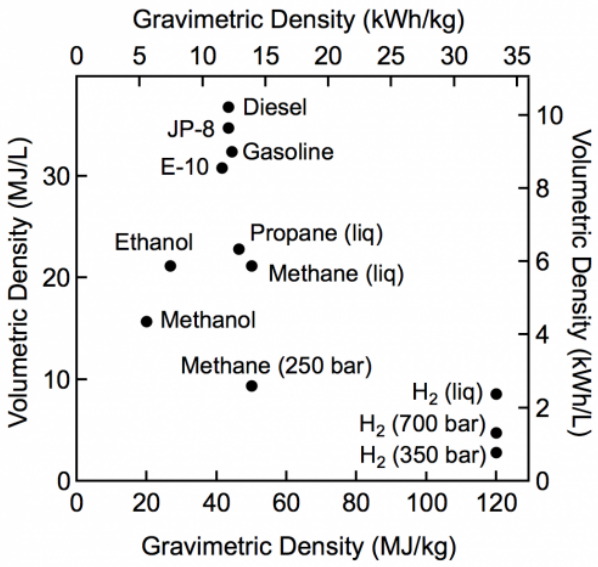

Figure 1 Diagram showing the gravimetric and volumetric energy density of common fuels[6]

The last concern that I would mention here is the cost of implementing hydrogen infrastructure and devices. Since the industrial era, our society was only evolving by developing the, now, world spread use of fossil fuels without any concurrences. Technologies only based on fossil fuels have been developed and are implemented in all the aspect of our society. The cost of switching from a fossil-based society to a sustainable one will without any doubt cost a large amount of money.

1.2 A SHIFT AND INCREASE IN HYDROGEN PRODUCTION

While being the most abundant molecule in the universe, hydrogen (H_2) cannot be found in its pure form on earth and needs to be produced from a primary source of energy. As of today, approximately 96% of all hydrogen is produced from traditional fossil sources, with steam reforming of natural gas (48%), naphtha reforming (30%) and coal gasification (18%)[7]. Hence, as of today the production of hydrogen is far from being green. This is about to change, the only sector of society that did not give up on hydrogen was the scientific community and many alternatives already exist.

First of all, it is important to notice that since hydrogen cannot be mined or found anywhere on earth (recent studies found out that it is not entirely true), it is considered as a secondary source of energy. This implies that hydrogen needs to be produced by other means, the first one being the reforming or gasification of fossil sources as mentioned previously.

One of the main developments that aim at producing industrial quantities of green hydrogen is the use of electrolysers. To make it simple, an electrolyser works as a reverse fuel cell, electrical current is used to produce hydrogen and oxygen from water (equation 1). Just as fuel cells, there are three main categories of electrolysis cells and they differ in the type of ion transported through the electrolyte[8]:

- Alkaline electrolysis.
- Polymer electrolyte (or proton exchange) membrane electrolysis.
- High-temperature steam electrolysis.

$$H_2O \xrightarrow{I} {}^1/_2\, O_2 + H_2$$

Equation 1 Overall reaction of water electrolysis

Since the electrolysis of water requires an electrical input, the electricity must come from renewable sources such as solar, wind or even nuclear (not completely sustainable but worth mentioning) in order to produce green hydrogen. Hydrogen would then act as an energy carrier or secondary energy source and would be produced when an excess of electricity is produced (during sunny or windy days) compared to the electrical grid demand. Hydrogen would then be reconverted in electricity when the grid electrical demand increases or when the production of electricity decreases. Electrolysis energy conversion is extremely efficient. Alkaline electrolysis has a commercial efficiency approaching 47.5 kWh kg^{-1} H_2 (70% conversion efficiency) but recently a group published a paper showing a 40.4 kWh kg^{-1} H_2 which is 82% conversion efficiency.[9] Solid oxide electrolysers have an efficiency mounting to 90-100% efficiency while proton exchange membrane electrolysers approximate 70-90%.[10]

Biomass gasification has been extensively studied for the production of hydrogen. A gasifier is an industrial type of reactor where the biomass is injected at the top and subsequently undergo a drying phase, a pyrolysis and the gasification to produce gases (H_2, CO, CO_2,CH_4, tar) in ratios that would vary depending on the type of biomass used, the gasifying agent (mainly steam, CO_2, O_2 or supercritical water) and the process parameters (Figure 2)[11,12]. It is also worth noting that from the gasification, ashes remain at the bottom of the gasifier, these ashes are interesting fertilizers as they have a large specific area and contain all the minerals included in the original biomass.

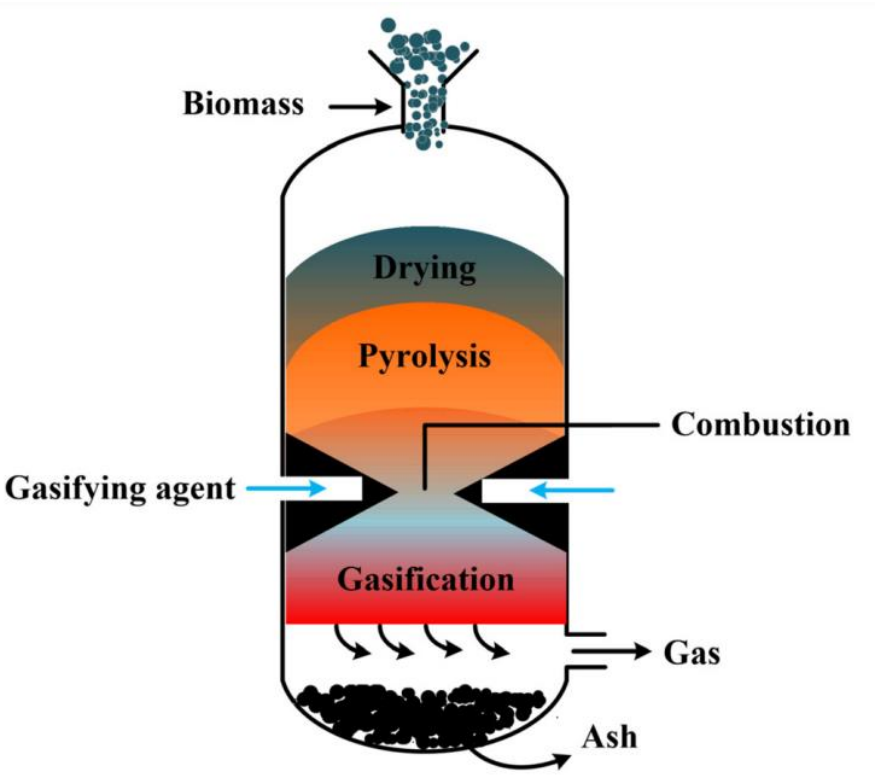

Figure 2 Schematic representation of an industrial type of biomass gasifier for the production of hydrogen (or syngas)[12]

Biomass has the advantage of being almost endless as so many substrates can be used and requires absolutely nothing from human input beside collecting and bringing to a gasifier. Many studies have shown the variety of biomass that can be used but the most interesting would be any type of organic waste (wastewater plant sludges, crops residues, food residues etc...). In the author's opinion, no human production should be invested in producing such biomass to be injected in gasifier. Indeed, just as with biofuels we could produce crops or wood to feed gasifiers, but this should not be considered as organic wastes already exist in tremendous amount across the planet and are either destroyed or disposed of while they could be used to produce energy (hydrogen).

Photocatalysis has also been considered a good mean of producing hydrogen. In this context, there would be no production of electricity with solar panel to subsequently produce hydrogen with an electrolyser but instead the sunlight would directly produce hydrogen. Water naturally splits at 2500 K, which is a temperature that is too high to be sustainable and the needs in thermal energy would be too compelling which is why a photocatalyst using sunlight is a cheap alternative. Currently, two means of production of hydrogen with photocatalysis exist, the direct scission of water into H_2 and O_2 and the photo reforming of organic compounds.[13]

Another interesting approach would be to make use microorganism's and their enzymatic array as many species have been found to produce hydrogen from biomass. Gray and Gest[14] classified them as "Obligatory anaerobic" such as *Clostridium sp.,* "facultative aerobic" that degrade formic acid into hydrogen such as *Enterobacter aerogenes* and "photosynthetic" which produce hydrogen through photosynthesis such as eucaryotic *green algaes* or prokaryotic *cyanobacteria's.*[15]

Earlier it was mentioned that hydrogen cannot be found in its molecular form on earth, it is not entirely true. Recently geologists have discovered natural sources of this compound in continental shallow wells[16,17] in Mali while drilling for water[18], in oil and gas explorations in Kansas (USA)[19] and in rock mines[20,21]. H_2-enriched natural gases were monitored in the Kola peninsula in Russia leaking from caves[20,22]. Hydrogen has also been observed in sedimentary basins in Russia[23], USA[24] and Brazil[25]. The extraction of this hydrogen could also be considered to supply the energy sector[26].

As you can imagine from those examples of hydrogen production, a broad range of solutions are available. All of them could become predominant and would produce its fair share of hydrogen to power our society, more interesting ways can be found in the literature and many reviews have been written on the subject which I invite you to read[27,28]. When green hydrogen will be produced in industrial quantity, we can imagine a circular economy that will power part of the society and be based on hydrogen (Figure 3).[29]

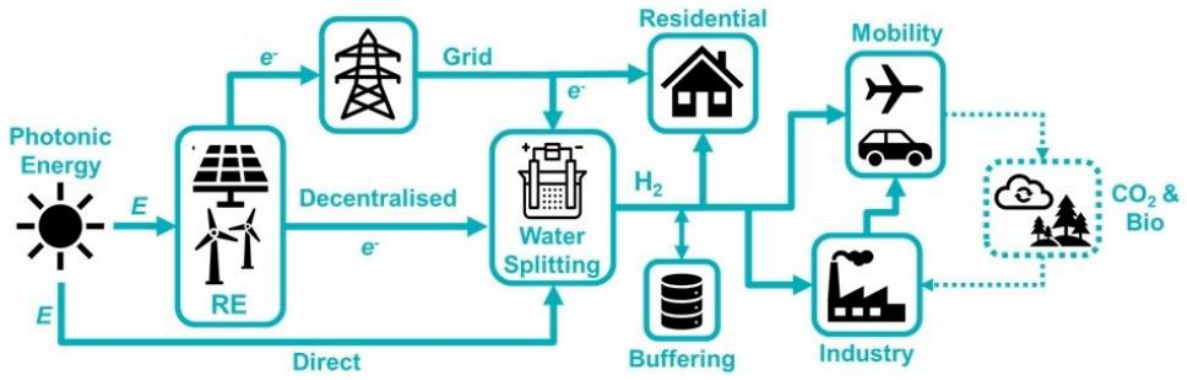

Figure 3 Simplified schematic description of an integrated hydrogen based chemical-energy system.[29]

1.3 THE HYDROGEN TRANSITION: A GEOPOLITICAL CONCERN

The political world has been slow to spark an interest in the energy transition but due to the increasing alarming warning of the IPCC and natural disasters, they slowly adopt a long-term strategy in which

the hydrogen economy will play a significant part. The recent events due to the 24th of February invasion of Ukraine by the Russian army and the economic sanctions that fell shortly after were also a huge warning sign. As the European Union import a large portion of its oil and gas from Russia, the issue of having reliable fossil fuels suppliers was also raised.

The twenty-seven countries of the European Union (EU) consumed in term of primary energy source, for the year 2020, approximately 58.6 Exajoules. From this, 35% come from petroleum products, 24% from natural gas, 17% renewable energy, 13% nuclear energy and 12% solid fossil fuels (mainly coal). The EU is able to produce around 42% of its own energy which means that 58% is imported.[a]

In the context of climate change, the European commission addressed a working document on 14th of July 2021 to the European parliament called "Fit for55". This package contains a set of legislative proposals that aim at cutting greenhouse gases emissions by at least 55% by 2030 compared to 1990 levels and net neutrality by 2050.

This package can be articulated around 3 pillars to be tackled: Energy, transportation and emission reductions. Each pillar is subdivided in propositions to tackle some of the worrisome greenhouse gases sources.

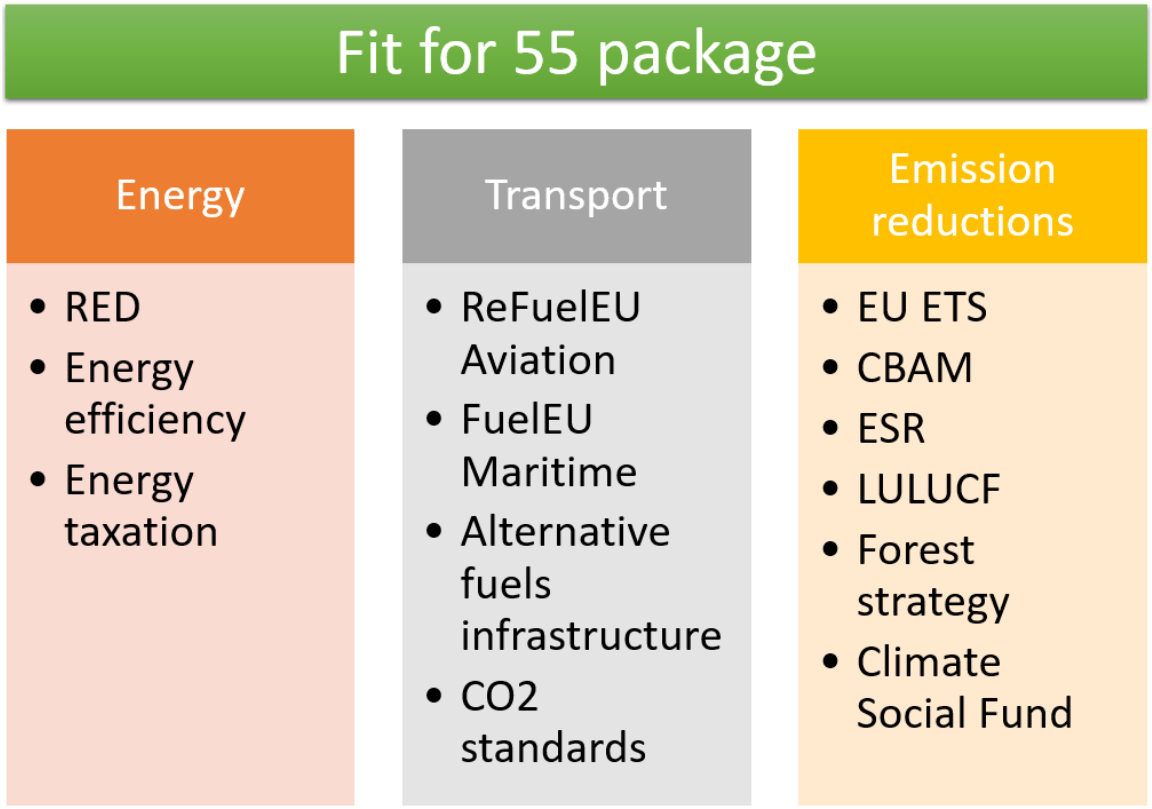

Figure 4 Overview of legislative proposals included in the "fit for 55" package. RED = renewable energy directive, EU ETS = EU emissions trading system, CBAM = carbon border adjustment mechanism, ESR = effort sharing regulation, LULUCF = land use, land use change and forestry regulation.

In Energy we can find:

- Renewable energy directive: the EU plans on substantially increase its share of renewables in its energy mix. The fit for 55 package ambition to reach a total of 40% of energy from renewable sources by 2030. The development of low emitting greenhouse gases sources of energy will include, wind, solar, hydroelectric, tidal, geothermal, heat pumps, biofuels renewable part of wastes. Moreover, hydrogen used in the industry should come 35% from renewables by 2030 and 50% by 2035.
- Energy efficiency: the goal of this directive is to reduce the use of energy within the European Union. By 2030 countries will have to cut by 36% the final energy consumption and 39% for the primary energy consumption. The three major sectors concerned are buildings, industry and transportation.
- Energy taxations: As of now, stationary greenhouse gases emissions are dominated by the energy sector with 77% of overall GHG emissions, 11% for agriculture, 9% for industrial processes and 3% for waste management. The overall directive aims at higher taxation for more polluting sources, the goal is to incentive consumers, producers and users to adopt sustainable practices. Coal, gas and petroleum products will be taxed the highest. Maritime and aviation fuels are now subject to taxation. There will be no distinction anymore between the type of use of fuels and electricity (commercial vs non-commercial or business vs non business use). And the tax base will be continuously adjusted annually based Eurostat consumer prices figures.

In transportation pillar:

- Fuel in aviation and maritime transport: at the moment, aviation represents 14.4% of transport emissions in the EU and maritime transport represents 13.5%. Aircraft fuel suppliers will have to supply up to 63% of sustainable fuel by 2050, airlines departing from the EU will be forced to refuel aircraft with the fuel necessary for the flights and airports will be accountable to provide infrastructure to deliver, store and refuel with sustainable aviation fuels. Airbus, one of the two major civil plane manufacturers with Boeing, placed their bet on manufacturing the first fully fuelled with hydrogen commercial plane. Maritime transports will be required to decrease by 75% their greenhouse gases emissions by 2050.
- Alternative fuel infrastructures: Transport is responsible for 25% of GHG emissions in the EU, road transport accounting for 71% of it. The goal set for this legislation is to increase refuelling station infrastructure throughout the EU. To increase the hydrogen, liquified methane and

electric refuelling stations within the EU territory to avoid distance anxiety. The number of electric vehicles and alternative fuels vehicles will increase drastically in the next year. The European parliament voted on the 2nd of June 2022 to ban sales of new petrol and diesel cars by 2035. The electric recharging stations would be installed on average 60 km from each other's by 2030 for cars and 2035 for trucks. Hydrogen refuelling stations will be installed at least 200 km from each other's along the roads. Liquified methane are to be set up along the mains roads in the EU to allow such types of vehicles to circulate.

- CO_2 emissions standards for cars and vans: 15% of all GHG emissions in the EU are due to the use of cars and vans. The standards for CO_2 emissions will decrease by 55% from 95 g(CO_2)/km for cars and 50% from 147 g(CO_2)/km for van by 2030 and down to 0% for both in 2035 resulting in a complete ban voted by the European parliament of CO_2 emitting road vehicles for the same year.

Emission reductions pillar:

- EU ETS (Emissions Trading System): This system implemented in 2005 is based on the "cap and trade" principle for large installations, aviation companies and maritime transport. This means that greenhouse gases emissions allowance can be traded on the EU carbon market. Basically, this means that large GHG emitters buy the right to emit these gases from low carbon emitters and the price is regulated by the offer/demand like trading stocks. The gases that are covered are CO_2, N_2O and PFCs, reducing the emissions of those gases in specific industries will provide money from the exchange of allowances to further decrease the emissions, and force the large emitters to decrease their emissions to cut off their cost. In the "fit for 55" package, the reform includes a faster reduction of the cap to -4.2% annually compared to -2.2% annually which means that emitters will gradually pass the cap faster and more companies have to cut their GHG emissions.
- Carbon Border Adjustment Mechanism (CBAM): This system works in parallel with the ETS and aim at controlling the emitters outside of the EU that are importing in the EU. In this context CBAM certificates are bought by emitters importing in the EU to compensate the ETS they would have to pay for if they were located in the EU, this would render the competitiveness to produce in countries with less strict environmental countries nil. The imports that are covered are Iron/steel, cement, fertilisers, aluminium and electricity.
- ESR (Effort Sharing Regulation): While the ETS focused on companies, the ESR focuses on member states, citizens and activities which include road transport, agriculture, buildings, small industries and wastes. Similarly to ETS, each member state have a cap that they are not to cross and that gradually decreases with a target set for 2030 at -40%. Countries are granted

annual locations that they must not overpass, and similarly to ETS they can trade allowances between countries, it can borrow allowance from the next year or the other way round.

- LULUCF (Land Use, Land Use Change and Forestry regulation): This regulation aims at involving carbon sinks in the equation of reducing GHG emissions. Since 2018, the EU member state must ensure that emissions from land use and forestry are compensated by an equivalent removal of CO_2 which is set at the removal of 225 Mt. This rule will stay in place until 2026 when the target will be raised to 310 Mt. This removal of CO_2 from the atmosphere is accounted for in member states carbon emission balance.
- Social climate fund: This fund is allocated to support the people and businesses most impacted by the new measure taken with the "fit for 55" package. This fund will help to tackle energy poverty and improve access to zero and low emission mobility and transport in the EU. With an estimate of 39 million energy poor people, 59 billion € will be funded to member states to help vulnerable households, micro-enterprises and vulnerable transport users.

With this package of legislations, it is the hope to drastically cut carbon footprint from the EU member states and place the climate change as a top priority challenge to tackle. Green hydrogen will play a significant role in this transition in terms of energy supplier for transportations and decarbonisation of key industrial sectors using hydrogen in their processes.

In 2022, the unjustified declaration of war from the Russian federation to Ukraine also played a significant part in motivating a transition toward green energies. Indeed, the EU realised that they were completely dependent on Russian gas, oil and coal. Hence a transition for diversification of partner suppliers has been on the move. On the 18th of May 2022, a new plan based on Fit for 55 called *REPowerEU* was published by the European commission to boost even further the pace of transition with a specific target to be independent from Russian fossil energy by 2027 in which the production and use of green hydrogen plays an even more significant role. This new initiative plans the investment of €300 billion by 2030. Out of those €300 bn, €27 bn are planned to fund the development of infrastructures for hydrogen.

As these lines are being written, the first companies were selected to receive an initial public funding for a total of €5.4 bn (Figure 5).

Figure 5 List of the companies that will receive an initial investment fund totalizing €5.4 bn for the development of infrastructures of hydrogen in Europe. 35 companies with activities in one or more Member States, including small and medium-sized enterprises ('SMEs') and start-ups, will participate in 41 projects. (15 of July 2022).

The aim of the European Union is to develop the infrastructures for the industrial and societal use of hydrogen throughout Europe. This initial public investment is expected to generate €8.8 bn in private investment.[b] The idea is to implement a roll-out from R&D to end users and to start the development of hydrogen circular economy. An interesting paper by Oxford economics[30], a think tank, has linked public fundings to private fundings and how initial investments are important to start the roll-out of private investments. As the initial fundings are clearly aimed at companies and their activities we can expect research funds for hydrogen technologies to come in the next years.

Since the hydrogen economy is a hot topic, every part of the development of it in our society is highlighted. The development of infrastructures, the fuel cells/electrolyzers efficiency, hydrogen storage and all the aspects of the hydrogen economy development are of the utmost importance. While, as we saw, the first bricks are being laid on the wall for the hydrogen infrastructures, the scientific community has the responsibility to keep up the pace with research to keep developing and rendering the hydrogen circular economy safe, efficient and competitive. This is where this thesis is taking place, at the crossroad between chemical vapour synthesis and hydrogen technologies. Throughout this PhD we strove to produce highly efficient materials to be used in fuel cells by using

state of the art chemical vapour deposition synthesis. These processes have an important future in industry as they can easily be scaled-up.[29,31–34] The combination of a scalable industrial tool and the production of fuel cells components naturally becomes highlighted. We will see later in this chapter that CVD can be used for the development of proton exchange membrane but in this thesis we focused on the synthesis of proton exchange membrane and the elaboration of gas diffusion layers using CVD.

2 GAS DIFFUSION LAYERS

Proton exchange membrane fuel cell (PEMFC) technology is one of the many alternative solutions currently under development for energy delivery by academics, governmental and industrial organization. PEMFC are devices that can turn chemical energy into electricity in one step. The most widely used fuel as of today is hydrogen which deliver water as the sole waste of such devices, making an eco- friendly power delivery system. PEMFC are set up following the diagram in Figure 6 and work as follows.

Hydrogen is fed at anode where the oxidation takes places, the electrons are retrieved via conducting materials to an outer circuit as electrical current. Protons are transported through the membrane to the cathode where they react with oxygen to produce water as a waste. As depicted in Figure 6, fuel cells are devices with a stack of various components with precise roles organized in a planar symmetry around the proton exchange membrane (also referred as polyelectrolyte).

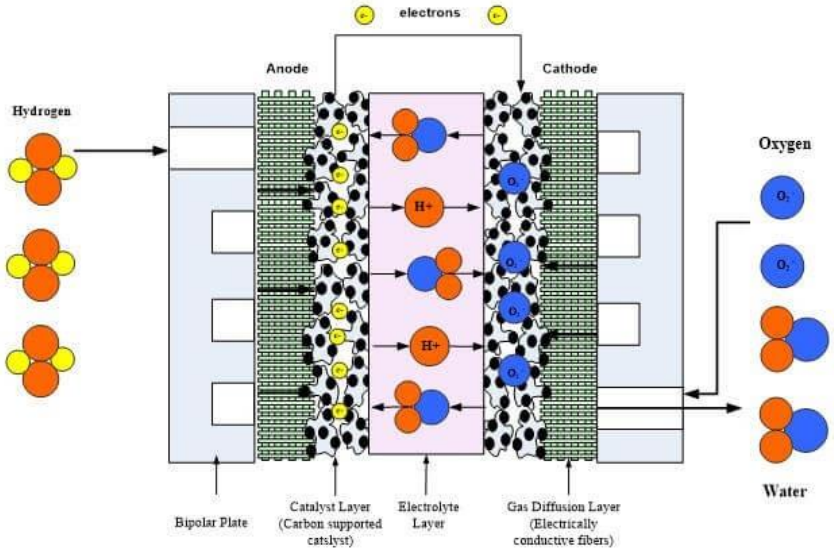

Figure 6 Schematic representation of a working fuel cell with all its layers (Bipolar plate, gas diffusion layer, catalytic layer and electrolyte layer)[35]

From left to right, we have a bipolar plate, gas diffusion layer, a catalyst layer (anode), the electrolyte membrane, the second catalyst layer (cathode), the second gas diffusion layer and the second bipolar plate. The bipolar plates act as channels to inject the reactant gases into the fuel cell, the CL's are responsible for carrying out the chemical reaction of oxidation and reduction, the membrane facilitates the transport of proton from the anode to the cathode while electrically insulating one from the other. The GDL is responsible for bringing the gases to the catalyst layers while evacuating the generated water on the cathode side.

2.1 SUPPORTS OF DIFFUSION

GDL's are commonly made out of a support of diffusion, a hydrophobic treatment or a microporous layer. The support of diffusion can be used as a GDL, but their performances are in general not optimized compared to the several treatments that exist and have been investigated. This subchapter discusses the various support of diffusion and properties required for their use in fuel cells.

Basic support can be classified as woven supports including carbon cloths that are produced by the weaving of carbon fibres. Non-woven supports that include carbon paper that are produced by suspension of carbon fibres followed by the evaporation of the solvent and carbon felts that are produced by calcination of a precursor polymer felt (Figure 7).

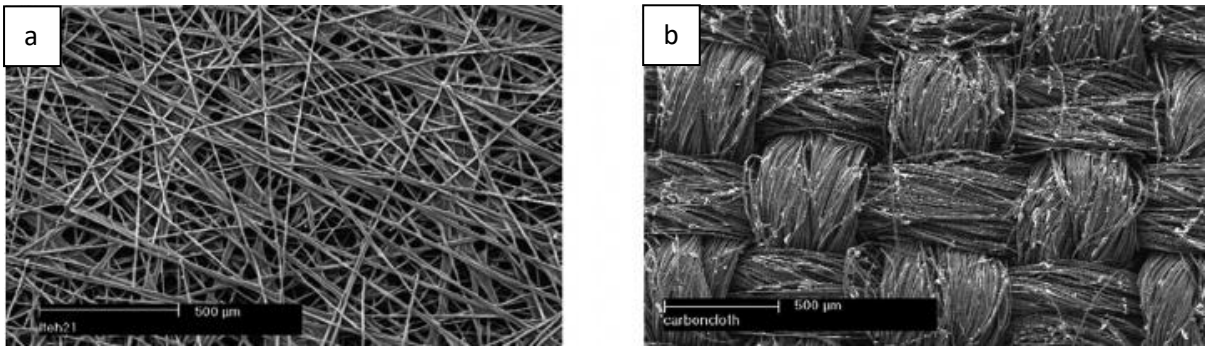

Figure 7 Scanning electron microscopy top view imaging of (a) commercial Toray 060 carbon paper and (b) E-Tek carbon cloth[36].

Supports of diffusion must have the following function and associated properties listed in Table 1

Table 1 List of function and properties for supports of diffusion. [37]

Function	**Property**
Electron transport	Electrical contact

Heat transport	Thermal conductivity
Reaction gas transport	Pore size distribution and gas permeability
Corrosion stability	Purity, surface stability and chemistry
Bridging to bipolar plates	Bending stiffness and compressibility
Water management	Hydrophobicity

They must be electrically conductive because they bind the catalytic layer (where the electrons are generated) to the bipolar plate (where the electron are collected for the outer circuit). For this reason, many support of diffusion are made out of carbon fibres based material such as polyacrylonitrile (PAN)[38].

Electrical resistivity is commonly measured following two methods, the two points probe (2-pp) or four points probe (4-pp) methods. In the 2-pp method, two electrodes are used as both current and voltage sensing probe while for the 4 pp a known current is injected between two probes and the resulting voltage drop is measured with the two other probes. *Ex-situ* measurements are the most common, but resistivity can also be assessed *in-situ.*

The electrical conductivity of the support of diffusion is dependent on the compression factor as is shown in Figure 8 for various thickness of carbon fibres paper manufactured by Toray. The importance of the compression factor makes in-situ measurements more relevant.

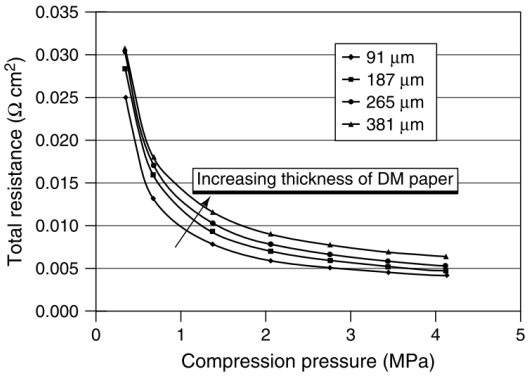

Figure 8 Total resistance vs compression pressure for Toray carbon paper of various thicknesses

The redox reaction taking place within a fuel cell is exothermic, this extra heat must be evacuated, or the temperature of the cell may uncontrollably increase. High temperature can dehydrate the electrolyte and contribute to performance losses, alter the reactions kinetic and affect the durability of the MEA. The supports of diffusion must be able to evacuate the extra heat generated to work under stable conditions[39].

The support of diffusion must be able to effectively deliver the different gases to the catalytic layer. As shown in Figure 7, carbon paper and carbon cloth are highly porous, but Utaka et al.[40] measured the coefficient of diffusion, for oxygen, to be in the order of $6{,}5.10^{-6}$ $m^2.s^{-1}$ in the case of paper structure and 12.10^{-6} $m^2.s^{-1}$ in the case of cloths structures. The authors also suggested that the knowledge of porosity alone was not enough to characterize the diffusion coefficient but the structure of the material such as the tortuosity was also important.

The performances of fuel cells based on the diffusion support has not been studied extensively in the literature. Usually, research groups study the performance of the support with either a hydrophobic treatment or a microporous layer.

2.2 HYDROPHOBIC TREATMENT

The supports of diffusion may undergo a hydrophobic treatment for optimal use. On the cathode side, the water is produced and requires to be evacuated [38]. This type of treatment prevents the flooding of the catalyst layers, at the cathode side due to the production of water and at the anode where the humidified gases arrive and the retro diffusion of water through the membrane can flood the anode.

In general, the gas diffusion layers are treated with aqueous solutions in a suspension of fluorinated polymer. Polytetrafluoroethylene (PTFE) or fluorinated Ethylene Propylene (FEP) are the most widely reported. These treatments aim at improving water management of the cell but are also known to decrease the electrical conductivity of the support of diffusion, as studied by Yoon et al.[41] who investigated the impregnation of carbon paper with (heptadecafluoro-1,1,2,2-tetrahydrodecyl) triethoxysilane.

The most widespread method for diffusion support hydrophobization is impregnation. The carbon cloth or carbon paper is soaked in a solution of suspended fluoropolymer (or other) with the desired concentration before being rinsed to remove excess polymer and dried in an oven to remove the solvent. Mathias et al. [38] showed that a further thermal treatment at 350°C increase the adhesion of the polymer to the surface. The authors also suggested that a slow drying process allows for a better dispersion of the hydrophobic material at the surface.

Other methods have also been investigated such as pulverization or brushing which are interesting for a one-sided treatment. Plasma treatment are preferred when one desire to conformally coat the

carbon fibres, as shown by Lee et al. where the authors used a plasma treatment of CHF_3 on a commercial carbon cloth (Figure 9)[42]. A similar process has been used in this thesis.

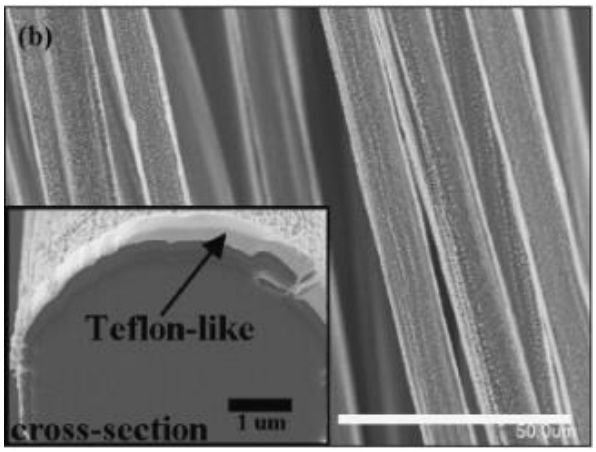

Figure 9 Electron microscopic images of carbon cloth treated with CHF_3 in plasma conditions[42]

One might think that the higher the content in fluorinated material the better the water management but Lim et al.[43] and Yan et al.[44] showed that there was an optimal loading at 10 wt % for a Toray TGP-H090 carbon paper. Increasing further the loading proved to clog the macropores of the support of diffusion and blocked the evacuation of water as well as increasing the electrical resistance.

2.3 MICROPOROUS LAYERS

The most common way to improve the properties of the GDL is to add another layer to the support called the microporous layer (MPL) (Figure 10). This MPL placed in contact with the CL is usually made of a mix of carbon black mixed with polytetrafluoroethylene (PTFE). This hydrophobic treatment allows the passage from macroporous to microporous substrate for the catalyst layer. This increases the electrical contact between the CL and the GDL, moreover the hydrophobicity allows for a better evacuation of water out of the fuel cell to prevent the flooding of the catalyst. On the cathode side the water is generated hence the importance to apply a hydrophobic treatment on the cathodic GDL, though a hydrophobic treatment can also be useful on the anodic side as retro diffusion of water during high humidity runs can also flood the anode.

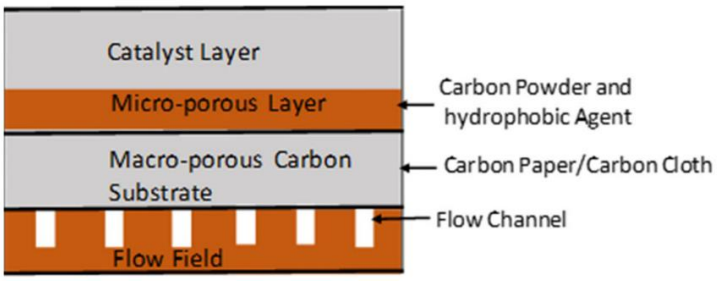

Figure 10 Detailed view of layers with focus on the gas diffusion layer between the catalyst layer and the bipolar plate (flow field in the figure)

The literature reported several ways of improving the fuel cell performance through the application of diverse treatments to the GDL. Weng et al. explored the hierarchisation of PTFE loading from the CL to the GDL in 3 layers and achieved better performance under low humidity[45]. Kitahara et al. used GDL with different hydrophilic (PVA-based)/hydrophobic (PTFE based) content on the cathode and anode side to increase the ability of the membrane to retain water as well as promoting the evacuation water [46]. The authors later studied the performance of PEMFC with a double MPL made of a layer of hydrophilic material (PVA) in contact with the cathode and coated with a layer of PTFE, they found out that the PVA was effective to maintain the humidity of the membrane without humidifying the reactive gases [47]. Leeuwner et al. used graphene foam as a microporous layer and found it was very efficient at retaining water on the cathode side under low humidity conditions and also demonstrated excellent durability of their system [48]. Velayutham et al. studied the upgrading of carbon cloths with an MPL with different PTFE content and found out that a 35% PTFE loading gave the best PEMFC performance [49]. Latorrata et al. replaced PTFE with Perfluoropolyether in the MPL on carbon cloth support, they found that there was an increase in PEMFC performances from conventional PTFE loaded MPL at 80°C and 60% relative humidity[50]. The authors further investigated other fluorinated polymers, such as perfluoroalcoxy, fluorinated ethylene propylene, fluorinated polyurethane on Perfluoropolyether and showed that fluorinated ethylene propylene had the best properties[51]. Ong et al. replaced PTFE with polyvinylidene fluoride on a carbon cloth support and managed to reduce mass transport losses in PEMFC test performance at a current density higher of ca. 0.3 $A.cm^{-2}$ [52]. Kong et al. used Li_2CO_3 pore forming agent and discovered that pore size distribution was more important than the total porosity[53].

3 POLYMER ELECTROLYTE MEMBRANE FUEL CELL (PEMFC)

A fuel cell is an electrochemical cell that convert the chemical energy of a fuel (often hydrogen but methanol, ethanol and ammonia have also been studied[54,55]) and an oxidizing agent (oxygen or air) into electrical energy via redox chemical reactions. The basic unit of a fuel cell is an electrolyte sandwiched between two electrodes. The fuel is oxidized with a catalyst at the anode to produce electrons and a charge carrier that can interact and be transported through the electrolyte while the electrons are collected and used in an outer circuit. An oxidant reacts then with the charge carrier and the electrons with the help of a catalyst to produce water as a waste. The principle of fuel cells based on hydrogen work in reverse of the water electrolysis seen earlier in this manuscript.

With Hydrogen: $H_2 + {}^1/_2\, O_2 \rightarrow H_2O$ [56]

With methanol: $CH_3OH + {}^3/_2\, O_2 \rightarrow CO_2 + 2H_2O$ [55]

With ammonia: $2NH_3 + {}^3/_2\, O_2 \rightarrow N_2 + 3H_2O$ [57]

Several types of fuel cell exist and are classified based on their electrolytes. Depending on the electrolyte used, several parameters can change in the fuel cell such as the working temperature, the catalyst used on the electrodes, the reaction taking place at the anode and the cathode, the charge carrier. Table 2 reproduced from Lucia et al. [58] sums up these differences.

Table 2 Tabular summary of the different fuel cell that have been described in the literature, their main differences and their respective electrode reactions[58]

Characteristics	**Polymer electrolyte**	**Alkaline**	**Phosphoric acid**	**Molten carbonate**	**Solid oxide**
Electrolyte	Hydrated polymeric proton exchange membrane (e.g. Nafion®)	Sodium or potassium hydroxide solution	Immobilized phosphoric acids in SiC	Sodium or Potassium carbonate supported by a ceramic matric ($LiAlO_2$)	Perovskite (ceramics)

Operating temperature [°C]	40-80	65-220	~200	650	600-1000
Electrodes	Carbon	Platinum	Carbon	Nickel alloy	Perovskite and perovskite/metal cermet
Catalyst	Platinum	Platinum	Platinum	Nickel alloy	Perovskite and perovskite/metal cermet
Charge carrier	H^+	OH^-	H^+	CO_3^{2-}	O^{2-}
Anode reaction	$H_2 \rightarrow 2H^+ + 2e^-$	$H_2 + 2OH^- \rightarrow 2H_2O + 2e^-$	$H_2 \rightarrow 2H^+ + 2e^-$	$H_2 + CO_3^{2-} \rightarrow H_2O + CO_2 + 2e^-$ $CO + CO_3^{2-} \rightarrow 2CO_2 + 2e^-$	$H_2 + O^{2-} \rightarrow H_2O + 2e^-$ $CO + O^{2-} \rightarrow CO_2 + 2e^-$
Cathode reaction	$O_2 + 4H^+ + 4e^- \rightarrow 2H_2O$	$O_2 + 2H_2O + 4e^- \rightarrow 4OH^-$	$O_2 + 4H^+ + 4e^- \rightarrow 2H_2O$	$O_2 + CO_2 + 4e^- \rightarrow 2CO_3^{2-}$	$O_2 + 4e^- \rightarrow 2O^{2-}$

In a PEMFC, molecular hydrogen is supplied to the anode, where it splits into protons and electrons, as typically catalysed by a Pt or Pt alloys. Proton migration across the membrane supplies the cathode, where the kinetically limiting ORR occurs to yield water, as also catalysed conventionally by a Pt-based alloy) (Figure 11a). A number of other reviews discuss the development of high performance electrocatalysts for these reactions.[59–61] Membrane performance (e.g. delivering protons) represents a critical function in PEMFC efficiency and they therefore must possess excellent proton conduction and electron insulation properties. They must also be durable to cell operational conditions (e.g. applied potential under acidic pH; potentially for degradation via peroxide formation etc.). Conventional materials are composed of a polymer or co-polymer, of which several examples are known,[62–64] with the current dominant market product being Nafion® (e.g. from Dupont®).

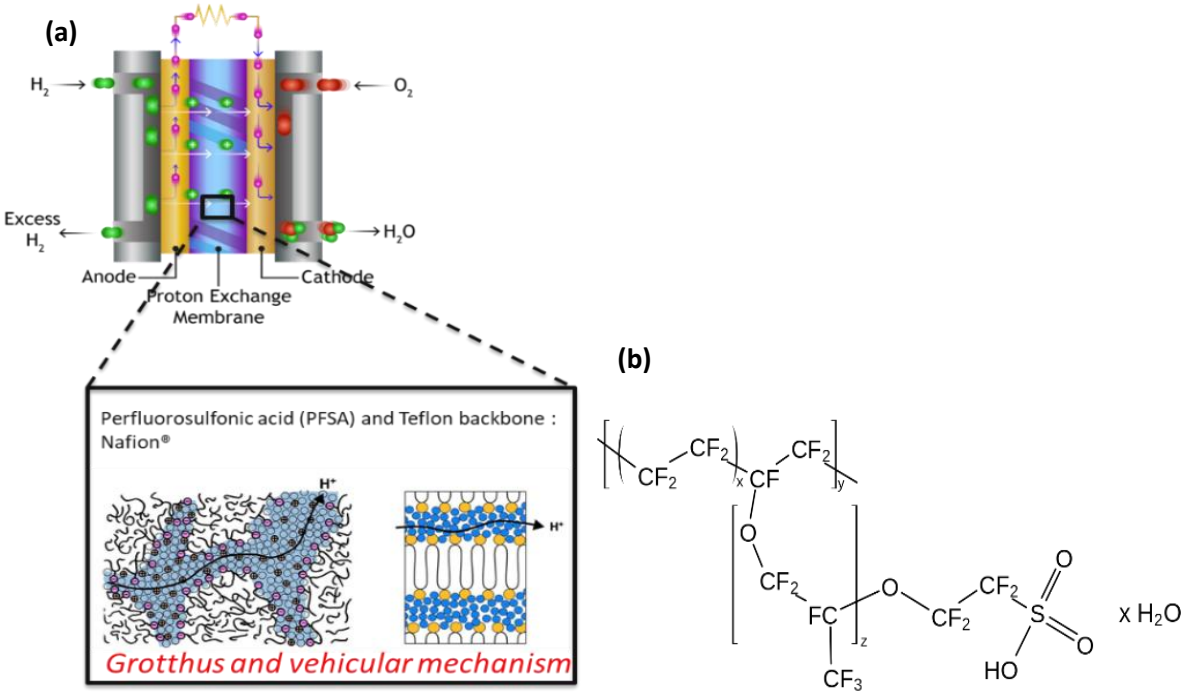

Figure 11 (a) Schematic representation of a working PEM fuel cell with proton transport through the membrane. Reproduced with permission from Prof. C. Frank (Stanford Uni) and Dr. M. Millikin (Editor at Green Car Congress). (b) Generalised molecular structure of Nafion® - a polytetrafluoroethylene backbone (as defined by x and y repeats) featuring pendant chain (z = repeat number) as terminated with a sulfonate end group.

Chemically, Nafion® is a copolymer of tetrafluoroethylene and perfluoro-sulfonic acids pendant chains (Figure 11b). While the polytetrafluoroethylene crystallizes and creates hydrophobic clusters, the perfluoro-sulfonic acid creates hydrophilic channels that fill with water (Figure 11a). Pure water, being non-electronically conductive but proton conductive, facilitates charges separation. Protons cross the membrane following a Grotthuss or a Vehicular mechanism; the former proceeding via proton hopping from one water molecule to the next from a stationary oxygen atom to a neighbouring oxygen atom; the latter proceeding via proton attachment to a water molecule which is transported through the membrane via transitional diffusion (Figure 12).[65–67] The Vehicular mechanism occurs when water molecules move freely (i.e. when polyelectrolyte membranes are highly hydrated). The Grotthuss mechanism can also occur at lower humidity with water molecules bonded to acidic groups [68].

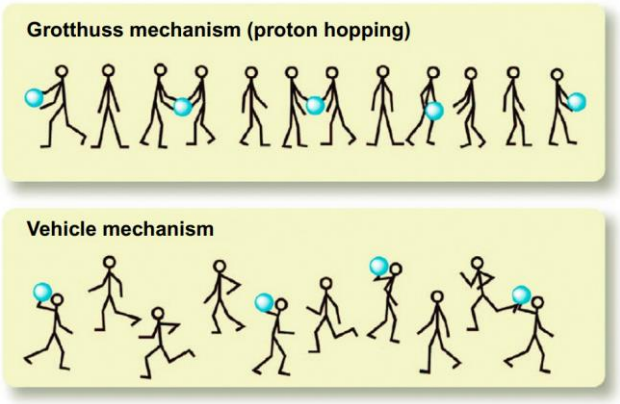

Figure 12 Simplified representation of the Grotthuss and Vehicular transport of protons. Reproduced with permission from Ref [69].

Polyelectrolytes have mainly been produced through wet processes [70], bringing several drawbacks including swelling, shrinkage, agglomeration, and wastage whilst typically being costly and multistep. The development and application of innovative approaches to overcome these drawbacks are naturally of significant interest. A relevant approach is CVD, which uses gaseous precursors that are capable of reacting on various surfaces. As will be discussed in the following sections, polymer electrolyte membranes produced via CVD have scope to provide significant performance improvement and advantages over the current benchmarks.

3.1 PROTON EXCHANGE MEMBRANES OBTAINED VIA CHEMICAL VAPOUR DEPOSITION

Ennajdaoui *et al.* reported on the production of a polymeric membranes from trifluoro-methane sulfonic acid (CF_3SO_3H) and styrene precursors by PECVD.[71] The plasma input power (W) and mass flow of precursors (%F) were modulated and classified based on the factor X, defined as $\frac{W}{\%F}$. The authors observed that the rate of sulfonic acid group introduction, for the same %F, increased with W until reaching a maximum at W = 5. The increase in sulfonation rate before the peak was attributed to a higher incorporation of $–SO_3H$ in the film, whilst after the peak, sulfonate functionality was broken down by the high-power input, with %F playing a lesser role. The highest conductivity (1.69 $mS.cm^{-1}$) was observed for the thin film with the highest sulfonic acid loading (i.e. W = 5 and %F = 10). In the same conductivity measurements conditions, Nafion®117 had a conductivity of 70 $mS.cm^{-1}$. The authors also studied the gas permeation of methanol through the membranes with respect to Nafion®117 benchmark. No clear dependence on the X factor was observed but the membranes

synthesized with PECVD showed a much lower gas permeation compared to the benchmark. High crosslinking of PECVD-membranes was proposed for the reason for this.[72]

Jiang *et al.* also studied the deposition of membranes based on styrene and trifluoro-methane sulfonic acid.[73,74] The properties of membranes deposited using continuous PECVD and pulsed plasma enchance CVD (PPECVD) were investigated in an initial reported, followed subsequently by a report focused on the role of duty cycle and trifluoro-methane sulfonic acid flow.[73] The authors studied the ionic exchange capacity (a quantification of ion exchange groups), the water uptake, the conductivity, the activation energy for proton transport and the methanol diffusion permeability by modulating the trifluoro-methane sulfonic acid partial pressure and the duty cycle (DC). Regarding membrane properties, highest ion exchange capacity (IEC), was found for the membrane prepared with a low DC and intermediate trifluoro-methane sulfonic acid partial pressure (1.77 meq g^{-1}). Water uptake was evaluated at 75.4% for the highest water uptake of the samples produced in that report. As comparison, Nafion®-117 was found to have an IEC = 0.93 meq g^{-1} and a water uptake of 34.6%. The membrane had high sulfonic group loadings and high-water uptake properties, with a conductivity at 194.4 mS cm^{-1}. The activation energies were similar to the one of the Nafion®-117 benchmark, but the methanol diffusion permeability showed less permeation for the sample produced by an order of magnitude of 10 or even 100.

Bassil *et al.* reported on a proton exchange membrane derived from the homo-polymerisation of dimethyl allyl phosphonate ($C_5H_{11}O_3P$).[75] The authors investigated the IEC and the conductivity with regards to the power of the glow discharge. The highest conductivity and IEC was obtained for a power of 60 W with 0.08 mS.cm^{-1} and 4.65 $m_{eg}.g^{-1}$ respectively, tested in the same conditions, Nafion®-211 showed 0.28 mS.cm^{-1} and 0.9 $m_{eg}.g^{-1}$. The permeation to methanol was much higher for the Nafion®-211 than for the plasma membranes.

The authors further investigated the PPECVD mode using a duty cycle of 0.5 (t_{off} = 5 ms) to homopolymerize dimethyl allyl-phosphonate.[76] The pulse mode generates comparatively mild conditions that lowers precursor fragmentation, decreasing the crosslinking density as reflected by recorded proton conductivities.[77,78] The authors studied the conductivity from the pulse mode, the continuous mode at 100 W compared with Nafion®-211. They found 0.14 mS.cm^{-1}, 0.11 mS.cm^{-1} and 6.7 mS.cm^{-1} respectively. They went further and showed that the specific resistance was actually lower for the membranes deposited via CVD because the thickness of the membrane was much lower (in the order of 1µm compared to 50 µm for Nafion®-211) which decrease the overall protonic ohmic losses.

In terms of materials chemistry, interest perfluorocarbon-based membranes (e.g. Nafion®) arises in part from the high chemical inertness, rendering membranes prepared from these polymers typically more durable compared to other systems (e.g. hydrocarbon polymers).[79] Perfluorocarbon-based polymeric membranes were reported by Thery *et al.* based on water and C_4F_8 precursors, with water inserting the ionic exchange functions in the polymer matrix.[80] In this paper, the authors focused on the multistacking of the PECVD films to increase the open circuit voltage (related to the gas crossover, the higher the OCV the lower the gas permeation). The authors correlated film crosslinking and density with the observed properties with higher densities resulting in reduced crossover but lower conductivities. The authors proposed that a membrane synthesised at a power of 300 W was a reasonable compromise leading to a OCV of 600 mV and a conductivity of 25 mS cm^{-1}. To overcome these limitations, multi-layered films were produced while maintaining a total thickness of 10 µm. For a film based on four layers, an OCV of 900 mV was obtained, comparable to Nafion®-211, for a conductivity of 10-30 mS.cm^{-1}.

Wood *et al.* reported on the deposition of poly(maleic anhydride) and poly(trifluoromethyl-maleic anhydride).[81] The water uptake of prepared films was shown to be high (167±7 wt.% and 143±3 wt.% respectively) compared to the one of Nafion® (ca. 30 - 35 wt.%).[82] In plane proton conductivities measured on water-soaked membranes showed competitive conductivity of 50±5 and 90±5 respectively (vs. Nafion® : 80 - 90 mS cm^{-1} under similar conditions). However, when conductivity measurements were performed for these membranes in 97% RH, very low proton conductivity was observed.

Urstöger *et al.* reported on the deposition of a novel ionomer chemistry based on hexa-methyl-di-siloxane (HMDSO) and methacrylic acid (MAA).[83] FTIR and XPS analysis revealed films where –C(O)OH functionality was maintained, with increasing MAA flow leading to high concentrations these groups under mild plasma power conditions. At higher power conditions, O-H bonds were cleaved, believed to lead to an increase in -COOR absorption intensity in FTIR spectra. In plane EIS measurements were carried out on one sample, reaching a conductivity of 1.1 ± 0.1 mS cm^{-1}. Unfortunately, the authors did not provide a comparison with a commercial benchmark.

In another report, Bosso *et al.* described the deposition of hexafluoro-propene (C_3F_6) / acrylic acid (AA) co-polymer films deposited via PECVD.[84] The authors studied the influence of monomer ratio and plasma power on the hydrophilic/hydrophobic functionality and membrane proton conductivity. The authors stated that 40 W is the required minimum power to activate C_3F_6. At lower power input and lower C_3F_6 flow rates, AA is the main component that polymerises to deposit the film. Conductivity of these co-polymer films, based on in plane EIS measurements, as a function of $C{=}O/CF_x$ ratio,

demonstrated that increased carboxylic functionality loading correlated with an increase in conductivity, reaching a maximum of 70 mS cm^{-1} with a polymer film membrane synthesised at 20 W and an AA:C_3F_6 ratio of 6:1.

All the previous reported proton exchange membranes synthesized via chemical vapour deposition made use of glow discharges, but some reported the use of iCVD (see 4.1). Coclite *et al*. reported on the preparation of a copolymer membrane of 1H, 1H, 2H, 2H,-perfluorodecyl acrylate (PFDA) and MAA.[85] The purpose of this study was to reproduce a structural organisation (like Nafion®) combining hydrophobic (PFDA) and hydrophilic (MAA) monomers. The obtained copolymer is notably hard to produce based on liquid phase synthesis, a consequence of the poor miscibility of the two precursors. This demonstrates the advantage of using CVD techniques to access new membrane chemistries.[86] Ranacher *et al.* studied the nanostructure of this copolymer membrane using X-ray diffraction (XRD), XRR and grazing incidence X-ray diffraction (GIXD).[87] It was found pure PFDA material organised into a smectite B type structure (in accordance with previous literature reports).[88–90] In plane EIS measurements were carried out, the conductivity was found to increase with increasing F_{MAA} reaching a peak for 41% F_{MAA} and 55 mS cm^{-1}. After that point, the conductivity tends to decrease due to the loss of organisation in the film. Nafion®-115 was used as a benchmark, presenting a conductivity of 126 mS cm^{-1} under the same experimental conditions.

When it comes to measuring conductivity (e.g. through EIS) of ion exchange membranes deposited via CVD (or indeed from other approaches), experimental set ups reported in the literature vary greatly, which has led to variation in reported Nafion® conductivities. This highlights the importance of having a widely studied benchmark material reference.

4 CHEMICAL VAPOUR DEPOSITION (CVD)

Chemical vapour deposition, commonly abbreviated as CVD is, in a broad sense, the formation of thin solid films on a substrate produced by making chemically react gaseous precursors. By opposition, physical vapour deposition (PVD) such as evaporation and reactive sputtering, involve the adsorption of atomic or molecular species on the substrate.[91] In CVD, the precursors in the gas phase are activated and react at the substrate surface to produce solid materials. These type of processes are interesting regarding their industrial application and could be in the future an essential tool for the production of various component that can be used in fuel cells[29]. These processes have the advantage to be easily scaled-up via Roll-to-Roll (R2R)[32–34] or large Batch to Batch (B2B)[92]

4.1 CVD CLASSIFICATION AND GENERALITIES

Many techniques of CVD exist, are being developed, and are in use at the moment. One way to categorize these techniques is by what type of activation the gases undergo. The main methods used are thermal CVD, high frequency radiation as UV-CVD and plasma enhanced CVD. Table 3 gives a tabular description of commonly known techniques used by different research groups.

Table 3 Examples of CVD techniques, their descriptions, and examples from reported literature

CVD technique	**Description**	**Examples from literature**
Plasma enhanced CVD	A glow discharge is generated inside the process chamber, activating gas-phase precursors, which in turn react together at the surface.	Deposition of Silicon dioxide (SiO_2) from SiH_4 and N_2O,[93,94] or from tetra-ethyl orthosilicate.[95,96]
Metal Organic CVD	Single or polycrystalline films produced from metal organic precursors.	$CuCrO_2$ thin-film crystal growth from Copper bis (2,2,6,6-tetramethyl-3,5-heptanedionate) and Chromium (III) tris(2,2,6,6-

		tetramethyl-3,5-heptanedionate).[97]
Atomic layer deposition (ALD)	Sequential use of reactants, whereby precursors are activated via plasma, heat, ultraviolet etc. to create a covalently bonded monolayer with the surface.	Deposition of alumina using trimethyl aluminium $Al(CH_3)_3$.[98]
Oxidative CVD (oCVD)	Oxidative initiator and polymer precursor(s) vapourised to react at a substrate surface via a step growth polymerisation.	Deposition of polymeric 3,4-ethylenedioxythiophene (PEDOT) and $FeCl_3$ as an oxidizing agent.[99,100]
Hot filament/wire CVD (HWCVD)	Hot filament array induces precursor thermal decomposition above a substrate upon which reactive species adsorb and react.	Fabrication of nanocrystalline diamond using acetone and hydrogen as precursors.[101]
Initiated CVD (iCVD)	Similar to HWCVD, an initiator breaks down (typically a peroxide) and initiate a chain polymerization occurs.	Synthesis of anti-microbial poly(dimethyl-amino-methyl styrene) coating with di-tert-amyl peroxide as initiator[102]
Laser and photo-assisted CVD	High intensity lamps use photons to promote deposition	Deposition of ZrO_2 films from Zirconium (IV) tetra-t-butoxide [103]

CVD is an attractive processing technology to produce thin films and typically relies on a heated substrate and the chemical reaction of gas-phase precursors.[104] CVD represents a wide class of synthetic methods, normally performed in a vacuum reaction chamber, whose working principle is based on the activation in the gas-phase of chemical species carrying the precursors of the thin film. Condensation typically occurs on the substrate surface and subsequent surface chemical reactions with the substrate material (or preceding layer). Numerous iterations of CVD have been described, with previous reviews describing its general use (e.g. see Ref. [105–109]) - these iterations are summarised

in Table 1 above. The potential advantages of CVD processing in comparison to liquid phase syntheses is summarised in Table 2 below:[110,111]

Table 4 Summary of potential advantages of CVD processing and the relevance to PEMFC performance improvement.

CVD Advantage	**Ref.**	**Relevance to PEMFC RDI**
Capability to produce dense and pure-material films	[112–114]	○ Densification important in terms of delivering thinner and higher performance MEAs to stacks
Capability to produce uniform thin films	[115,116]	○ Thin films possible with thicknesses from 10s of nm to a few µm, with good reproducibility ○ Potential to reduce proton ohmic losses (further discussion in Section 3.4.1)
Good adhesion of films to substrates	[117,118]	○ Interaction(s) of catalyst layer (e.g. Pt nanoparticles) ○ Polymer deposited with good adhesion will stabilize nanoparticles and inhibit migration, agglomeration, and/or deactivation [119,120]
Reasonably high deposition rate	[121,122]	○ Important with respect to large scale, rapid industrial production of MEA (e.g. via roll-to-roll)
Non-line-of-sight process	[123,124]	○ Scope to intimately coat complex (e.g. 3D) structures in the catalyst layer leading to improved triple phase boundary (TPB) conditions (further discussion in Section 3.4.3)
Adjustable deposition rates	[110]	○ Lower deposition rates favour epitaxial thin films; a higher deposition rate produces thicker protective films ○ Oriented polymer growth is highly interesting for the proton conduction as it can lead to proton pathways for the transport through the plane[125]
Wide variety of chemical precursors	[126–128]	○ Enables deposition of a large spectrum of materials (e.g. composites) with regard to membrane optimisation (Examples: metal halides, hydrides, organometallics, polymers).

		○ Improvement in Nafion® performance of interest with respect to stability (e.g. through compositing) ○ Desire to move away from fluorinated materials (e.g. with recycling)[129] ○ Scope to produce non-fluorinated membranes (described further in Section 3.2)
Solvent-less process(es)	[111,130,131]	○ Reduces potentiality of shrinkage, agglomeration, swelling, costly solvent and waste

The disadvantages of CVD are also worth highlighting. Current instrumentation is certainly costly which for industrial applications, require a continuous process to decrease manufacturing costs.[132] Most CVD occurs under high vacuum which is challenging with regard to production (e.g. on a batch-to-batch process, impacts of leakages etc.). In order to avoid this issue, roll-to-roll (R2R) processes have been suggested to firstly reduce costs and render production suitable for large scale industrial roll out (e.g. in the context of MEA manufacturer).[34,133,134] Depending on the specific CVD method and precursors used, toxic by-products can be generated in the exhaust system[132], hence the need to thoroughly know a specific process before scaling-up. It is to be noted that this is of increasing concern with respect to the environment and ecological impacts (e.g. global scale use perfluorinated polymers) given limited scope for recycling or appropriate disposal (e.g. incineration requires costly, specialized conditions).[135–137]

4.2 WHAT IS A PLASMA?

In this thesis we exclusively used CVD techniques based on plasma activation. Plasma is the so called "4th state of matter" and is an ionized or partially ionized gas. Heating solids result in the atoms/molecules to break free from the crystal lattice to form a liquid. When the liquid is further heated the atoms/molecules evaporate faster than they condensate which results in a gas formation. When a gas is heated sufficiently enough, the kinetic energy of particles exceeds the ionization energy, the atoms or molecules collide with one another knocking off their electrons, ionizing the gas, a plasma is formed[138]. Plasma can either be natural or artificial,

Table 5 Examples of naturally occurring terrestrial, astrophysical plasmas, and artificial plasmas

Artificial	**Terrestrial**	**Astrophysical**
Plasma display (plasma screen)	Lightnings	Stars
Fluorescent lamps	Magnetosphere	Solar winds
Rocket exhausts and ions thrusters	Ionosphere	Nebulae
Plasma torches	Northern/southern lights	
Inductively coupled plasmas		

Plasma can be characterized by three criterions that are explained and demonstrated below[139]:

Particle density: positive ions can be singly charged or multiply charged. In the case of a singly charged cations, the population of particles is described as follow.

$$n_i = \frac{number\ of\ particles}{volume}$$, $[n_i]$= cm^{-3} or m^{-3}

Electron density: Plasma are in quasi neutral state which means that $n_i \approx n_e$ (where n_e is the electron density) and in the case of multiply charged particles the charge number of positive ions is z and the density of ions with a charge z is indicated as n_z. The density of electrons become:

$$n_e = \sum_z z.n_z$$

One person will speak of a high/low density plasma if $n_e$is large/small.[140]

Degree of ionization, which is defined with the particle's density, and not the charge density, is defined as:

$$\eta_i = \frac{\sum_z n_z}{n_a + \sum_z n_z}$$, with n_a=neutral particle density (atoms, molecules or radicals).

The average kinetic energy (KE), given N particles of mass m and velocity v, the average KE per particle is given by:

$$\langle KE \rangle = \frac{1}{2N} \sum_{i=1}^{N} m_i v_i^2$$

Let's consider thermal equilibrium for which the particles have a Maxwell-Boltzmann distribution of speed:

$f(v) = N\sqrt{\frac{m}{2\pi k_b T}} exp\left(\frac{-1/2 mv^2}{k_b T}\right)$; with k_b the Boltzmann constant, T the temperature.

The average KE becomes:

$$\langle KE \rangle = \frac{\int_{-\infty}^{+\infty} 1/2\, mv^2 f(v) dv}{\int_{-\infty}^{+\infty} f(v) dv}$$

And we obtain:

$\langle KE \rangle = 1/2\, k_b T$, in one dimension

$\langle KE \rangle = 3/2\, k_b T$, in 3D

To investigate quasi neutrality, we assume that a cloud of electrons has moved to a certain area, which builds up a negative charge. A similar ion cloud is electron deficient in a distance $L \approx \delta x$ from the electron cloud (Figure 13).

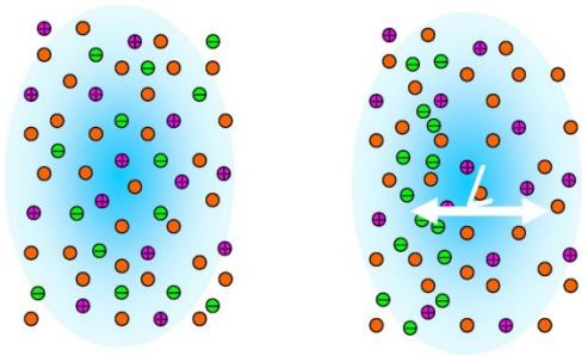

Figure 13 Illustration of charge separation in a plasma[139]

The resulting electrical field is obtained by using the Poisson's equation:

$E_{max} = \frac{e.n_i.\delta x}{\varepsilon_0}$; where ε_0 is the free space permittivity.

The gain in potential energy of an electron after moving through space away from the opposite charge carriers is given by

$$W_{pot} = \int_0^{\delta x} eE\, \delta x = \frac{e^2 n_e (\delta x)^2}{2\varepsilon_0}$$

And since the only energy available for the purpose of moving in space is the thermal energy or KE of the electrons (thermal energy of ions is usually very low compared to electron and is usually neglected in cold plasmas), with an average of $^1/_2\, k_b T_e$ for one dimensional degree of freedom, we obtain:

$\delta x = \left(\frac{\varepsilon_0 k_b T_e}{e^2 n_e}\right)^{1/2} = \lambda_D$, which called the Debye-Hückel length.

The Debye length is an important parameter to characterize plasmas and it provides a measure of the distance over which an individual charged particle can exert an electrical field and felt by other charged particles inside a plasma. The charged particles, which freely move, arrange themselves as to shield the electrostatic field within a distance of the Debye length. We can further extend this Debye-Hückel length to a sphere in which there is N_D electrons

$$N_D = \frac{4}{3}\pi\lambda_D^3 n_e$$

If L is the characteristic dimension of a plasma then, in order to respect the neutrality of it, a first criterion for the definition of plasma is

$L \gg \lambda_D$: **criterion #1**[141]

Since the shielding effect is a result of the collective effect of particles inside the Debye sphere, we also need the number of electrons to be large.

$\frac{4}{3}\pi\lambda_D^3 n_e \gg 1$; **criterion #2**[141]

The reciprocal is called the plasma parameter (g) and is taken in plasma theory as a measure of degeneracy in plasma. And by replacing λ_D by its equation we obtain

$g \propto \frac{n_e^{1/2}}{(k_b T_e)^{3/2}}$ [139]

A non-ideal plasma is very cold and very dense (called strongly coupled plasma) and in such conditions the correlations between plasma particles may become important. An ideal plasma is considered to be $g \ll 1$ (for weakly coupled plasmas) and is called the plasma approximation.

The last concept I would like to expose here is the plasma frequency. As we saw previously the electrical field generated by charges separation is $E_{max} = \frac{e.n_i.\delta x}{\varepsilon_0}$ which accelerates the electrons toward their initial position. As the electrons regain their initial position, they will overshoot the equilibrium position. By using Newton's law, we obtain

$m_e \frac{d^2\delta x}{dt^2} = eE = \frac{n_e e^2 \delta x}{\varepsilon_0} = {\omega_p}^2 \delta x$; where ω_p is the plasma frequency

Collisions between electrons and neutral particles will damp the collective oscillations and diminish their amplitude. If we want the oscillation to be slightly damped, it is necessary for the electron collision with neutrals frequency (γ_{en}) be smaller than the electron plasma frequency.

$\gamma_p > \gamma_{en}$; with $\gamma_p = \frac{\omega_p}{2\pi}$ and this is **criterion #3**[141]

With these criterions we could determine what is necessary to be considered a plasma. Figure 14 shows some typical plasma with their range in temperatures, electron density, frequency as well as their Debye length. In this thesis we focus on the plasmas that are called glow discharges as they are the ones we generate in laboratories to study synthesis of materials.

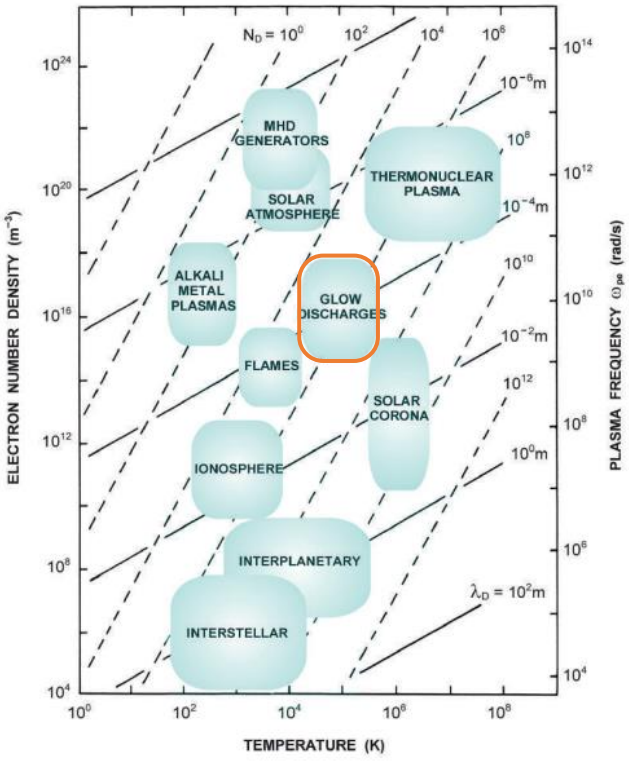

Figure 14 Ranges of temperature and electron density for several laboratory and cosmic plasmas and their characteristic physical parameters: Debye length λ_D, plasma frequency ω_p, and number of electrons N_D in a Debye sphere.

4.3 ARTIFICIAL PLASMA AND GLOW DISCHARGES FOR CVD

The most common way to generate and sustain a low-temperature plasma is by applying an electric field to a neutral gas. Any volume of neutral gas contain a small residual portion of free-electrons and ions.[142] These free charges are accelerated by an electric field and new charged particles are created by collision. This leads to the so called "avalanche" generation of charged particles that is eventually balanced by the charge carriers' losses to reach a steady state glow discharge. Discharges are classified as direct current (DC), alternative current (AC) for capacitively and inductively coupled plasmas or microwaves discharges on the basis of the temporal behaviour of the applied electric field.[143]

4.3.1 DC discharges

In a DC discharge, the voltage applied between two electrodes will reach the *breakdown voltage* of the gas, the discharge can be ignited, and a plasma sustained. The breakdown voltage is proportional on the pd product where p is the gas pressure and d the distance between the electrodes. This is called the Paschen's Law[144,145]. Several regimes of discharges can be observed when one varies the current in a DC glow (Figure 15a). At low current, the discharge is self-sustained, invisible to the eye and is called the Townsend discharge. Increasing the current sees a drop in voltage that is called the break down voltage to reach the subnormal discharge before reaching a threshold called the normal discharge. Further increasing the current sees a drastic increase in voltage that is called the abnormal discharge. Eventually, at very high current the discharge transitions to arcs for what is called the glow-to-arc transition that is characterized by a steep drop in voltage and the occurrence of lightnings between the electrodes.[146] In Figure 15b we can see the typical profile of a DC normal glow discharge. The brightest part of the discharge is the negative glow which is located in between the cathode dark space and the Faraday dark space. The cathode dark space is characterized by its sharp potential drop followed by an increase to reach the negative glow potential. The Faraday dark space is characterized by a steady high potential and low electrical field close to zero. The homogeneous light emitting region is called the positive column which extend up to the anode.[143]

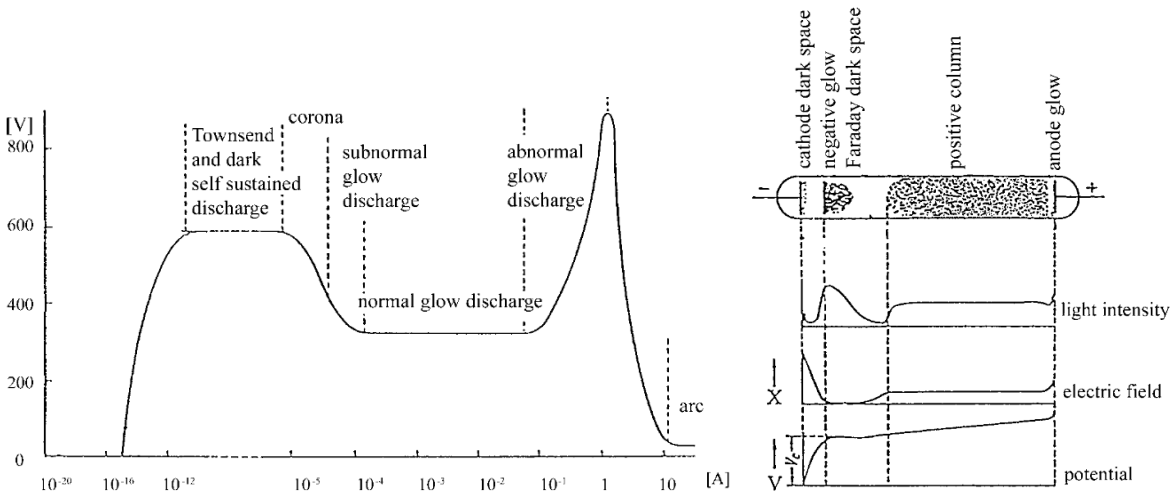

Figure 15 (a) Dependence of voltage vs current and the various kind of Neon DC discharges (1.3 mbar, flat copper electrodes 10 cm², distant with 50 cm); (b) Variation of light intensity, electric field and electric potential along the axis form cathode to the anode.[147]

4.3.2 AC discharges (capacitively coupled and inductively coupled plasma)

Capacitively coupled RF plasma (CCP) are generated by applying a varying voltage between two parallel electrodes plates at a frequency usually comprised between 10-100 MHz (Figure 16)[143,148,149]. In this type of plasma typical electron density range between 10^8-10^{10} cm^{-3} in gas pressure ranging from 10 to 1000 Pa. The electrons temperature is comprised between 1-10 eV and is much higher than the gas temperature (namely ions temperatures) which makes it a non-equilibrium type of plasma. The electron plasma frequency (ω_e) is in the range 0.1-1 GHz which is much higher than the RF power source, which means that the external electric field applied to the plasma is considered static and cannot penetrate deeply into the plasma region due to the skin effect (see previous chapter) and is only applied to the sheath region[149].

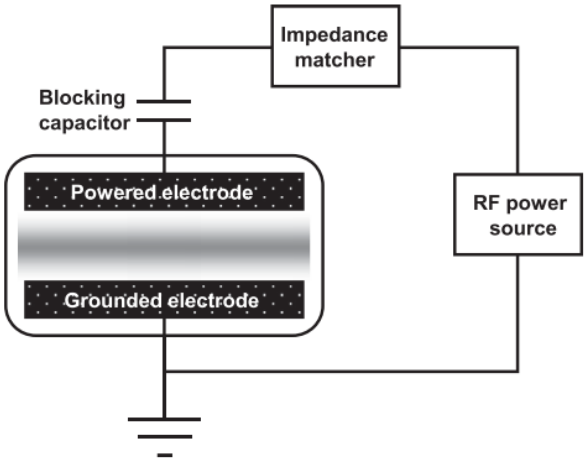

Figure 16 Schematic illustration of a CCP configuration [149]

Inductively coupled RF plasma (ICP) are generated by applying a current to a coil which generate a magnetic field B_{rf}, the alternative current in the coil makes the magnetic varies which according to Faraday's law $E_{ind} = \frac{-\delta B_{rf}}{\delta t}$ of induction, generates an inductive electric field (Figure 17).[143,148–150] The direction of the induced electric field is parallel to the coil and its strength is proportional to the RF current and its frequency. Typical electron density is comprised in the range 10^{10}-10^{12}cm^{-3} (with that, CCP is usually called low density plasma compared to ICP) for gas pressure between 10 and 1000 Pa. As it is the case with CCP, the electrons temperature is between 1 and 10 eV. With an RF power source comprised between 1 and 100 MHz, the induced electric field cannot penetrate deeply into the plasma region due to the skin effect.

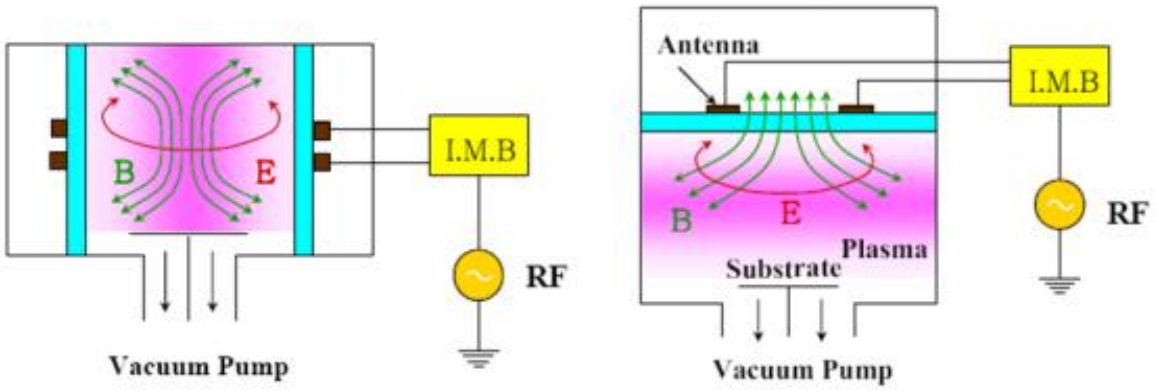

Figure 17 Schematic illustration of ICP reactor with (a) coil antenna and (b) planar antenna

4.3.3 Microwave discharges

Microwave plasmas CVD are different from other plasma techniques because the microwave frequency can oscillate electrons[151]. In the microwave plasma, the microwaves are transferred via a waveguide and is launched to the plasma region through a dielectric window. There exist two main type of microwave plasma configuration, the first one being the Electron Cyclotron Resonance (ECR) and the second the surface wave plasma (Figure 18)[143,149]. In the ECR, the plasma is generated via electron cyclotron wave, which is a circular motion of the electron in a static magnetic field. When the electron cyclotron frequency and the magnetic field strength satisfy the resonance conditions (ECR region) with the frequency of the microwave, a plasma is ignited. For example, a magnetic field of 875 G electron cyclotron frequency of 2.45 GHz which correspond to 12.2 cm. In the absence of external magnetic field, the microwave propagates between the window boundary and the plasma column. The wave is absorbed as an evanescent wave into the plasma.[143] With this latter technique, large surfaces of material can be deposited like silicon film deposition.[152]

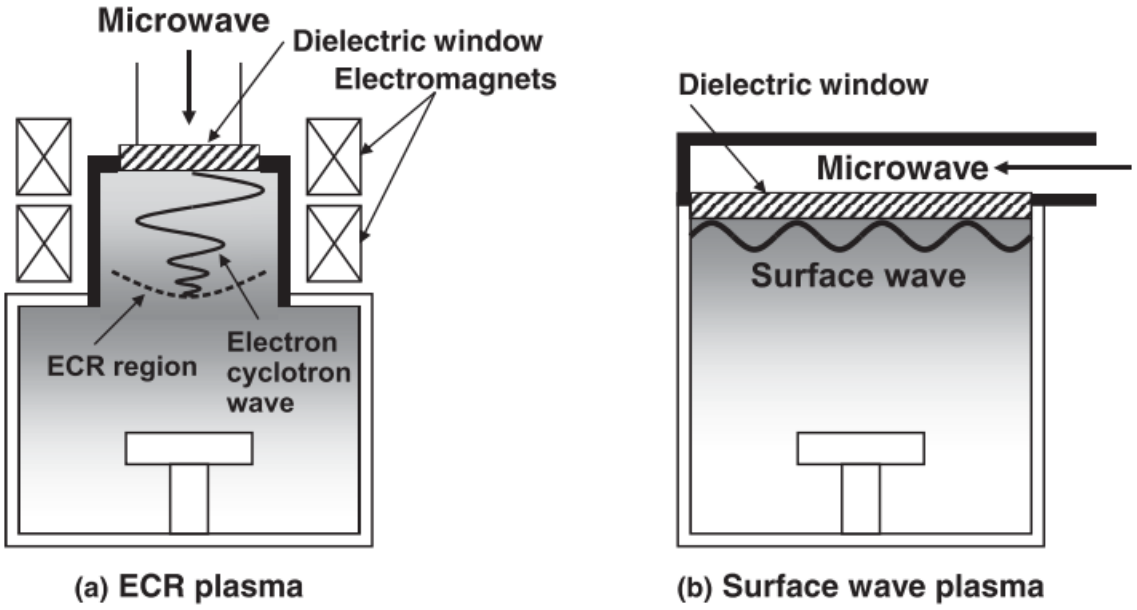

Figure 18 Schematic illustration of microwave plasma configurations: (a) Electron Cyclotron Resonance, (b) surface wave plasma[149]

4.4 REMOTE PLASMA PROCESSES

Plasma promoted CVD can be used with a plasma unit in a remote position from the substrate. The first report of this technique date back to 1985 and was published by the department of physics at the University of North Carolina[153,154]. The group studied the deposition of silicon nitride (Si_3N_4) and silicon oxide (SiO_2) from silane coupled with excited oxygen for the deposition of SiO_2 and excited nitrogen or ammonia for the deposition of Si_3N_4.

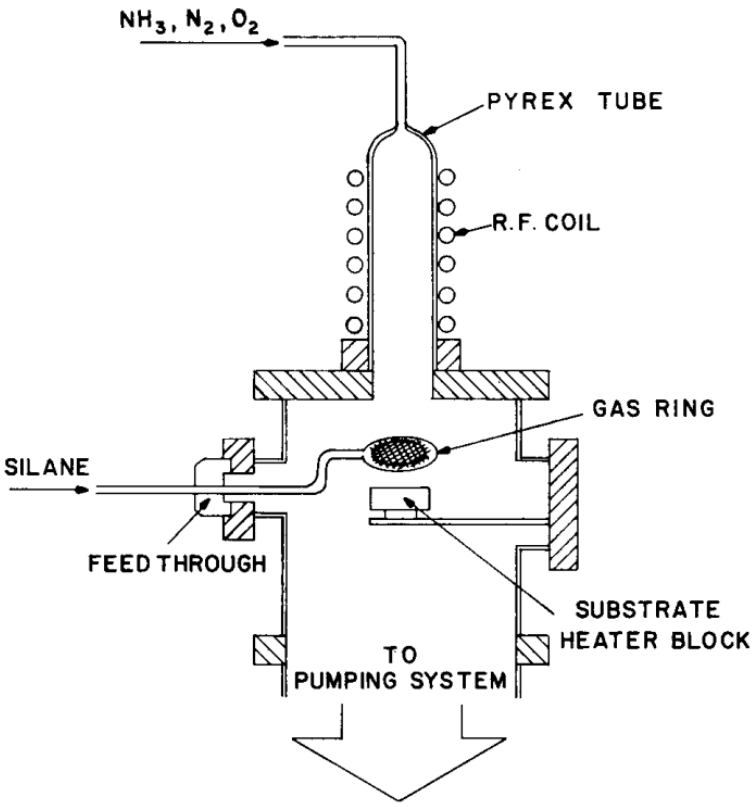

Figure 19 Schematic representation of a remote plasma deposition chamber used by North Carolina University group

In Figure 19, the system designed to deposit Si_3N_4 and SiO_2 with a remote plasma configuration. The chemical reactions are as follow:

$$(NH_3)^* + SiH_4 \rightarrow Si_3N_4$$

$$(N_2)^* + SiH_4 \rightarrow Si_3N_4$$

and

$$(O_2)^* + SiH_4 \rightarrow SiO_2$$

The asterisks (*) indicate which species are inductively activated in the Pyrex tube. There are numerous advantages in using a remote plasma compared to a standard PECVD process. In a standard PECVD process the substrate and the growing film is constantly exposed to electron, ion and photon bombardment which cause the alteration of the film, the occurrence of pinholes and the generation of charges in the film[155]. Remote processes are also dominated by the chemistry of neutral species which make them easier to characterize and control[155–158].

When using remote plasma, one must carefully select what gas will undergo the remote glow discharge activation. One factor in particular, is called the *sticking coefficient,* indeed the radicals (or ions) generated will tend to interact with the wall of the reactor and may not reach the surface of the downstream substrate hence not participating in the deposition[159–163]. The higher the sticking coefficient *S* the more the generated species will tend to stick to the walls of the reactor[164], which is appreciable when the film growth occurs in the discharge (PECVD) but is unwanted when the glow discharge is taking place in a remote location with respect to the substrate position. In general, the *sticky* radicals are the ones that can initiate and propagate a polymerization (Table 6).

Table 6 Radical species and their sticking probability[161,163,165]

Radicals	Si	SiH	SiH_2	SiH_3	CH_3	NH_2	NH	$Si(NH_2)_2$
Sticking probability	~1	~1	0.7 ~1	0.1	0.001	0.01	0	0.05
Lifetime (order)	µs	10 µs		ms	-			

Another aspect to take into consideration are the gas phase reaction that will tend to decrease the number of reactive specie with respect to time and distance from the glow discharge to the substrate. Kushner et al.[159] studied the remote plasma activation of SiH_4 with a discharge feed gas of He/O_2 (95/5) and observed the following profile with respect to the distance from the plasma zone (Figure 20). The figure clearly shows the disappearance of energetic species with the distance from the plasma zone, showing how important the distance from plasma to substrate is important. Pérès et al.[166] suggested a computer model that showed typical inactivation of electrons in a He (100mTorr) remote plasma discharge and studied various reactor configuration, showing that the larger the downstream configuration of the reactor the lower the inactivation rate.

(a)

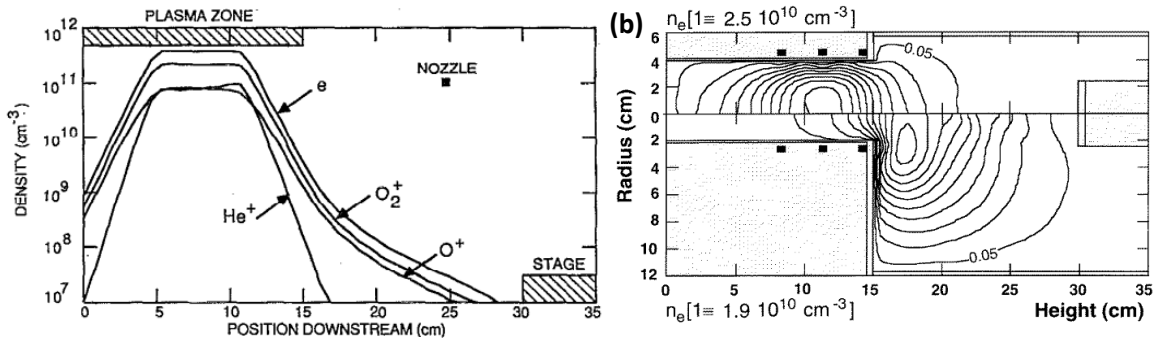

Figure 20 (a) Densities of electrons and select ions as a function of axial position (at r=O) for the base case conditions (He/O2=95/5), 300 mTorr, 210 sccm (e, O_2^+, O^+, He^+)[159]*; (b) The electron density (He, 100 mTorr) for different reactor geometries using the closely coupled coils: (top) R_P/R_D =0.66 and (bottom) R_P/R_D =0.16. Contour labels refer to the fraction of the maximum indicated by each value (with R_P: radius of the plasma zone, R_D: radius of the downstream zone)..*

In remote plasma, what is appreciated is the generation of active species that will flow downstream without interacting much with the reactor walls and will sustain their activation up to reaching the substrate. Hence, most of the time, the feeding gases will be of low polymerizable ability (noble gases, ammonia, oxygen…) and we would avoid gases such as silanes, hydrocarbons etc… In order to produce organic polymers or silicon-based polymers, the polymerizable gases will be injected downstream close to the substrate surface and undergo polymerization upon contact with the activated species coming from the glow discharge (see Figure 19). This type of system allows to retain a clean plasma zone (without too much deposition) and the polymer is deposited on the substrate.

Chapter II

Deposition of perfluorinated films and gas diffusion layer applications

The fine tuning of gas diffusion layers hydrophobic and conductive properties is highly important for the proper running of fuel cells. The application of hydrophobicity on conductive carbon fibres helps at the water management of the fuel cell and prevents its flooding. In this chapter we see the development of a know-how on the deposition of perfluorinated material from methane and tetrafluoromethane. The first part of this chapter sees the deposition of such films on silicon wafers and the thorough studying of the physico-chemical properties of such films. The second part focuses on the deposition of the films on carbon fibres fabric and the characterization with regard to gas diffusion layer application. The major finding was the discovery of a crystalline phase for specific deposition process conditions which gives rise to microstructures both on silicon wafers and carbon fabric. This type of deposition and microstructures helps for the water management by hydrophobizing the carbon cloths while maintaining the conductive behaviour of the carbon cloth.

1 INTRODUCTION

The present chapter relates to the elaboration of efficient gas diffusion layers for fuel cell applications. A specific piece of chemical vapour deposition machinery called PRODOS was used for this purpose. With this machine and CVD technique we developed a know-how on how to deposit perfluorinated material with tuneable hydrophobic and crystalline properties.[167] Tetrafluoromethane (CF_4) and methane (CH_4) activated via remote plasma were used to achieve the present results of this thesis. The first part of the chapter relates to the deposition of thin films on silicon wafers for the study of physico-chemical properties of the deposited material while the second part relates to the hydrophobization of commercial carbon cloths for application as gas diffusion layer in fuel cells.

CF_4 and CH_4 have opposite behaviour in a plasma. While methane has a high deposition rate in the form of an amorphous carbon film in a glow discharge[168], CF_4 is a powerful etching agent[169]. In an etching process, the highly reactive and energetic species from a gas bearing electronegative atoms (typically O_2 or fluorine bearing gases) bombard and react with the substrate surface resulting in the breakdown of the material in smaller volatile molecules.[170] In a remote plasma, the mix of fluorinated gases and a gas with high deposition rate work against each other, producing surface and gas phase reaction preventing the deposition of a film in the plasma chamber and allowing for a longer life-time of a the generated species in the gas phase. The deposition and the etching will act simultaneously but one can give predominance to one or the other by changing the CH_4/CF_4 ratio[171]. In a remote plasma, several steps will take place from the plasma chamber to the remotely located substrate. Due to its etching properties, CF_4 will prevent the deposition of an amorphous carbon film (due to the presence of CH_4) while adding fluorinated atoms in the chemical structure of generated volatile species.[172] Cunge et al. studied the occurrence of gas phase polymerization when fluorinated gases are fed into a plasma and the formation of oligomers.[173,174] Once the species exit the glow discharge activation zone the energy input disappear and the ion bombardment decrease in intensity allowing for deposition to occur.

Numerous studies have focused on the deposition of fluorinated material from glow discharges but only a few focus on the downstream deposition (remote plasma) of such materials. Typical species present in fluorocarbon discharges are the fluorine atom (F) and CF_x radicals (film precursors).[175] The relative amount of these species can be changed by varying parameters (monomer type, discharge power density, gas pressure, flow rate etc..) which will determine the structure of the deposited films. Typically, films grown in the glow discharge will result in a highly crosslinked network of functional

groups (CH_x, CF, CF_2, CF_3). Many of these species do not have a sufficiently long lifetime to be present in the downstream region. Thus, the type of and concentration of film precursors will depend on their formation rate and their lifetime. The species with longest lifetime will be present in the far distance from the plasma (e.g., 25 cm away from the plasma source) which also means that the film growth will be significantly slower downstream than in the glow discharge but it also provides an opportunity for the growth of fluorocarbon films with unique properties.[176,177] Castner et al. studied the remote deposition of tetrafluoroethylene (TFE) and hexafluoroethane (HFE) and observed the deposition of linear -CF_2- polymer chains.[176] The remote deposition of TFE showed a preferential orientation of the chains perpendicular to the substrate surface while HFE were not as highly ordered and oriented parallel to the surface. Martin et al. studied the influence of plasma power and substrate distance for the deposition of C_3F_8 and C_4F_8. The findings were that the lower the plasma power, the more linear the polymer chains and the farther the substrate the more linear the chains for both precursors showing that the film crosslinking decreases with the distance from the plasma.[177]

Deposition of fluorinated materials have attracted much attention due to the unique properties of such films. The reasons for the extensive use of fluorinated coatings are the good adhesion to many organic and inorganic substrate[178], low intermolecular forces, which gives rise to inert surfaces with low free surface energy[179], the biocompatibility[176], the low friction coefficient[180]. These properties find a wide array of industrial applications[181].

The specific purpose for the development of a process to coat surfaces with perfluorinated material finds its roots in the fuel cell field for the gas diffusion layer component. The GDL's are commonly made out of a support of diffusion which undergoes a hydrophobic treatment or the application of a microporous layer. The support of diffusion can be used as a GDL, but their performances are in general not optimized compared to the several treatments that exist and have been investigated. Basic support can be classified as woven supports including carbon cloths that are produced by the weaving of carbon fibres. Non-woven supports that include carbon paper that are produced by suspension of carbon fibres followed by the evaporation of the solvent and carbon felts that are produced by calcination of a precursor polymer felt. The properties of efficient GDL are listed in the following table.

Table 7 List of function and properties for supports of diffusion. [37]

Function	**Property**
Electron transport	Electrical contact
Heat transport	Thermal conductivity

Reaction gas transport	Pore size distribution and gas permeability
Corrosion stability	Purity, surface stability and chemistry
Bridging to bipolar plates	Bending stiffness and compressibility
Water management	Hydrophobicity

The supports of diffusion may undergo a hydrophobic treatment for optimal use. On the cathode side, the water is produced and requires to be evacuated [38]. This type of treatment prevents the flooding of the catalyst layers, at the cathode side due to the production of water and at the anode where the humidified gases arrive and the retro diffusion of water through the membrane can flood the anode.

In general, the gas diffusion layers are treated with aqueous solutions in a suspension of fluorinated polymer. Polytetrafluoroethylene (PTFE) or fluorinated Ethylene Propylene (FEP) are the most widely reported. These treatments aim at improving water management of the cell but are also known to decrease the electrical conductivity of the support of diffusion, as studied by Yoon et al.[41] who investigated the impregnation of carbon paper with (heptadecafluoro-1,1,2,2-tetrahydrodecyl) triethoxysilane.

The most widespread method for diffusion support hydrophobization is impregnation. The carbon cloth or carbon paper is soaked in a solution of suspended fluoropolymer (or other) with the desired concentration before being rinsed to remove excess polymer and dried in an oven to remove the solvent. Other methods have also been investigated such as pulverization or brushing which are interesting for a one-sided treatment. Plasma treatments are preferred when one desire to conformally coat the carbon fibres, as shown by Lee et al. where the authors used a plasma treatment of CHF_3 on a commercial carbon cloth. A similar treatment was used in this thesis but this time with the deposition of CH_4 and CF_4 downstream from the plasma chamber which prevent the substrate from being degraded by the glow discharge.

2 MATERIAL AND METHOD

2.1 PRODOS-200 PVPD™ R&D SYSTEM (AIXTRON SE)

In this chapter the machine used to deposit the samples and carry out the research is the pilot scale PRODOS-200 PVPD™ R&D system (Figure 21a). The system is based on the injection of gases through

a remote plasma unit to undergo activation. The plasma unit is radio frequency (RF) powered inductive (coil) remote plasma source (3000 W, 1.9–3.2 MHz, Model Litmas RPS 3001 from Advanced Energy). The deposition chamber is located downstream from the plasma unit and is equipped with an 8 inches substrate holder. A primary pump keeps the system under a vacuum in the order of tenth of mbar at full capacity. Various gases can be connected to the plasma unit but in this thesis, the depositions were done with a mixture of methane (CH_4) and tetrafluoromethane (CF_4). The activated gas mixture is spread over a showerhead for homogeneous deposition (Figure 21b).

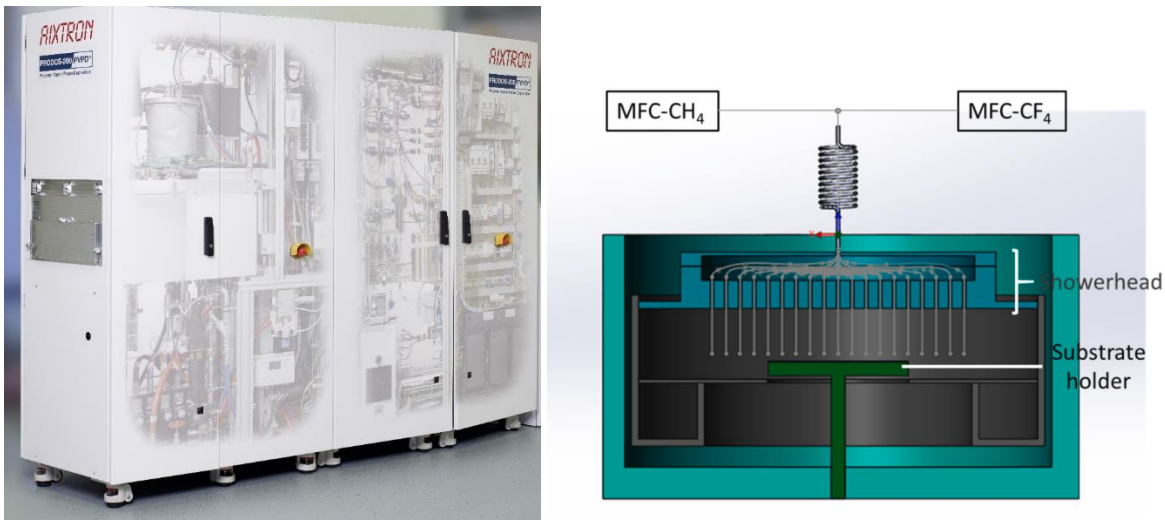

Figure 21 (a) Scheme of the PRODOS-200 PVPD™ R&D system industrial machine, (b) the deposition chamber with the remote inductive plasma unit equipped with a coil[167]

The machine was controlled via the Aixtron software from which here is a short description (Figure 22).

1. The gas injection panel: Used to inject CF_4 and CH_4 to the deposition chamber. Include also a bubbler to vaporize volatile liquids (not used in this manuscript).
2. Liquid injection panel: control the injection of liquids (not used in this manuscript), includes a cannister containing the liquid to be injected through the showerhead, a solvent cannister for the purging of the injection line. An injector with regulated opening time, frequency and the total number of pulses. A trijet™ for the evaporation of the liquid droplets with a regulation of temperature on five levels.
3. The plasma panel: to control the power input settings and the ignition of the plasma unit.
4. Deposition chamber panel: Controls the temperature of the showerhead, the temperature of the deposition chamber walls, the clamping of the substrate on the substrate holder, indicate the temperature of the substrate holder (temperature controlled in a non-displayed panel). The pressure is regulated by the opening of a throttle valve (TV in the panel), an automatic

and fixed mode are available, in the automatic mode, the throttle valve will respond to the measured pressure and vary it's opening to match the desired pressure, in the fixed mode, a fixed throttle valve opening is set.

5. Exhaust and pump panel: controls the temperature of the exhaust pipe (to avoid condensation of species), the sealing of the deposition chamber lid via the double O ring (DOR in the panel) and controls the primary and secondary pumps.

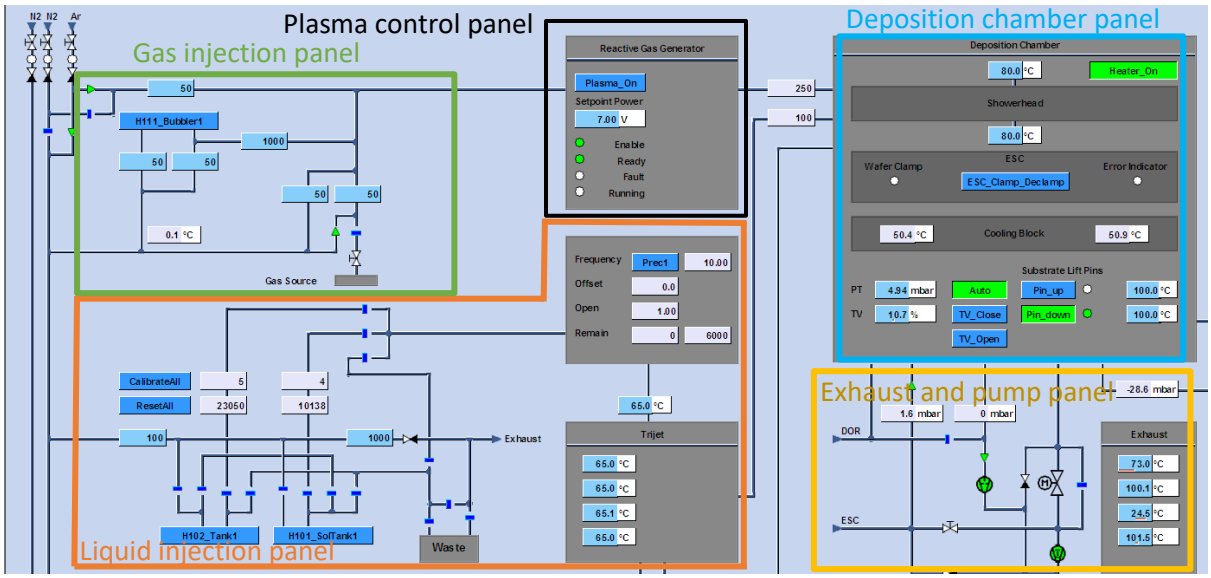

Figure 22 Main control panel of the Aixtron software used for manual handling of the multiple parameters that controls the PRODOS system

2.2 SUBSTRATES

The substrate for the first part and the study of the deposition are 8-inch silicon wafers (SIEGERT WAFER GmbH, Germany) with a resistivity of 0.5-100 Ω cm. The second type of substrates were commercial carbon fibres fabrics *Panex PW03*™ of 400 µm thickness, an electrical resistivity of 0.0014 ohm-cm and a carbon content of 99 % purchased from FuelCell store.

2.3 REACTIVE ION ETCHING (RIE)

Reactive ion etching is a dry etching technique that cleans the substrate from adsorbed organic matter. All susbtrates were treated with 40 sccm of oxygen activated with a plasma at 50 W for 30 seconds and a pressure at 60 mTorr in a Plasma-Therm 790 RIE.

2.4 WATER CONTACT ANGLE

Hydrophobic properties of deposited films were evaluated with water contact angle. This property is essential to evaluate the wettability of surfaces covered with our deposition. Static water contact angles (WCA) were measured by a Theta T200 by TECHNEX with a 2 µL drop of distilled ultra-pure water at 1.4 frame per second. 2.1. The contact angle was derived from the Young-Laplace equation from a photography taken by the apparatus.

2.5 SCANNING ELECTRON MICROSCOPY (SEM)

Scanning electron microscopy is a high-resolution imagery technique for samples surfaces based on the principle of interaction between electrons and matter. The resolution can go as low as ten nanometers. The equipment used was a FIB-SEM (FIB for Focused Ion Beam) HeliosNanolab™ 650 from FEI (Eindhoven, Netherlands). The deposited films were imaged with an acceleration voltage of 2 kV, current 25 pA and a 4 mm working distance. A 5 nm platinum layer was sputtered at a current of 30 mA prior to analyses to render the surface conductive and avoid electrical loading effects and degrade the films.

2.6 PROFILOMETRY

KLA Tencor™ P-17 stylus profilometer (diamond tip 2 µm thickness;radius of curvature: 60◦) was used to estimate the samples thicknesses with step-height technique on scratched films. Data's were acquired at a stylus speed of 20 µm/s; tapping frequency of 100 Hz with an applied force of 0.15 mg. Levelling of surface was performed with Apex software provided with the tool.

2.7 X-RAY PHOTELECTRON SPECTROSCOPY (XPS)

X-ray photoelectron spectroscopy is a surface elemental analysis probing the chemical composition of a material from a qualitative and quantitative point of view. The depth of analysis is shallow in the order of 10 nanometers[182] which allows for a sensitive analysis of the surface chemistry. The sensitivity of the technique is in the order of atomic percentage. XPS analyses were carried out with an Axis Ultra DLD Spectrometer (Kratos Analytical Ltd., UK) equipped with a monochromatic Al Kα X-

ray source (hν = 1486.6 eV). The analysis area was 300 × 700 µm^2. The acquisition of high-resolution spectra was done with a pass energy of 40 eV while the survey spectra were acquired at a pass energy of 160 eV. The spectra were treated with CasaXPS software.

2.8 X-RAY DIFFRACTION (XRD)

The crystalline structure of our samples was studied with X-ray diffraction. This technique gives an insight of the crystalline phases and the possible texture of the film following a preferential orientation. The samples were measured by a XRD X'Pert Pro equipped with a Cu anode (λ=0.1542 nm) and a PixCel3D detector. In order to best probe the structure of the deposited thin films, the measurements were performed at a grazing incidence angle of 0.5° and a 2θ range between 10° and 40° using a parallel plate collimator on the secondary optics. To determine the de- gree of crystallinity, each diffractogram was deconvoluted so that the background signal, the crystalline peaks as well as the amorphous content could be evaluated. For this, the software program Fityk[183] was used.

2.9 HELIUM ION MICROSCOPE COUPLED WITH A SECONDARY ION MASS SPECTROMETER (HIM-SIMS)

Helium Ion Microscopy (HIM) uses He^+ as a primary ions beam enabling ultra-high resolution ion-generated secondary electron (iSE) imaging with good depth of field. Coupling a Secondary Ion Mass Spectrometer (SIMS) offers the additional benefit of performing chemical imaging where He^+ is used for both high resolution iSE imaging as well as sputtering the sample surface generating secondary ions for SIMS detection.[184]

Sample preparation: The different fibres (n = 3) were embedded in Epofix resin (Struers), polymerised at room temperature for 8 hours and wet polished. The samples were coated with a 5-nm gold film via sputtering (Leica). *Analysis:* Measurements were performed with the Helium Ion Microscope coupled with a Secondary Ion Mass Spectrometer (HIM-SIMS, Zeiss, Peabody, US). A Ne^+ primary ion beam (impact energy of 25 keV and intensity of 5-7 pA) was used for scanning over a 25x25-µm^2 area on the sample surface with a sub-20 nm spatial resolution. The images were recorded in a 512 by 512 pixels raster. The SE image was acquired with an acquisition time of 1 µs.pixel^{-1} while SIMS images

were acquired at 3 ms.pixel^{-1}. Negative mode was used for the simultaneous detection of $19F^-$, $24C_2^-$ and $35Cl^-$ ions. *Data treatment:* The data were treated using OpenMIMS Data Analysis Software (ImageJ plugin), developed at the National Resource for Imaging Mass Spectrometry (NRIMS).

2.10 Environmental Scanning Electron Microscopy (ESEM)

ESEM allows for a gaseous environment in the sample chamber, which allows for imaging of non-conductive sample without nay additional coating needed. The ESEM was used in our case in a wet environment with high humidity level for the condensation of water vapour to occur. The Peltier heating/cooling stage lets us work within 20 Celsius degrees above or below ambient temperature, and the combination of low temperature (e.g., 4°C) and high-water vapor pressure (e.g., 6.1 Torr) permits us to achieve 100% relative humidity (RH) at the sample surface. The gaseous Secondary Electron Detector (GSED) was used which allows for the detection of secondary electrons from the gaseous atmosphere using the electron avalanche initiated by the impact of the primary electron beam on the sample surface. Sample images were recorded with a primary electron beam voltage of 17 kV at a total pressure of 6 Torr while maintaining a constant water vapour flow in the sample chamber. The Peltier temperature was maintained to accommodate the dew point at around 4°C.

2.11 Conductive Atomic Force Microscopy (cAFM)

Conductive AFM was used to probe the electrical conductivity with spatial resolution of carbon cloth fibres samples. Images of the topography and conductivity of the samples were simultaneously acquired using the C-AFM mode of an Innova AFM (Bruker). Conductive AFM tips ElectriMulti75-G from BudgetSensors coated with a layer of 5 nm chromium and 25 nm of platinum with nominal spring constants of 3 N.m–1 and nominal radius <25 nm were used. Images of a 4x4 μm^2 area with a resolution of 256x256 pixels were taken at a scan rate of 0.25 Hz. Carbon fabric samples were first cut into square of 1x1cm^2 deposited on a steel disk connected to the conductive stage. A silver colloidal ink is applied to electrically connect the carbon fabrics to the steel disk. The inspection area is optically checked to avoid any loose fibre which could be found over the carbon fabric surface and which could eventually short cut with the conductive AFM cantilever. The topography was obtained by maintaining the tip deflection constant (1 V) via the feedback loop of the AFM acting on the piezo Z direction. A bias was applied to the back electrode of the samples while the grounded conductive tip was collecting electrons for the current measured with an amplifier (DLPCA-200, Femto). The amplification of the transimpedance amplifier were adjusted according to the level of current encountered along the

samples surface. A 10^9 VA^{-1} amplification and a bias of +2V for the 40C sample and 10^7 VA^{-1} amplification and a bias of +2V for the 20C. A 10^6 VA^{-1} and +0.2 V settings were chosen for the highly conductive uncoated control sample in order to avoid high current density flowing into the tip and subsequent damage to it. The signal output was then transmitted to the AFM electronics and recorded.

Current images are log scaled using MountainSPIP software (Digital Surf, France). The current map of control carbon fabric is multiplied by a factor ten to compare data with a same 2 V bias. In this case we assume a linear increase of the current vs bias.

2.12 FUEL CELL TEST BENCH

The fuel cell test bench was used to draw polarization curves with the different GDL samples. The polarization curve displays the voltage output of the fuel cell for a given current density loading. The test bench was assembled at Umwelt-Campus Birkenfeld (Hochschule Trier) by the team of Prof. Gregor Hoogers (Figure 24). The test bench has a capability to draw current from 0 to 20 A (0 to 2 A.cm² in term of current density with a cell of 10 cm²).

1. The cathode panel: include a valve to select the gas to inject in the cell (air, oxygen hydrogen) and a pressure regulator valve.
2. The anode panel: include a valve to select the gas to inject in the cell (air, oxygen hydrogen) and a pressure regulator valve.
3. Temperature panel: controls the temperature of the cell by heating resistor, no cooling system was included.
4. Pressure components: Include pression controllers (one for the cathode side and one for the anode side) and pressure gauges.
5. Flow control: Mass flow controllers for the gas's injection on the cathode and the anode side.
6. Cell: the cell with an exploded view of the components (including the GDL) in Figure 23.

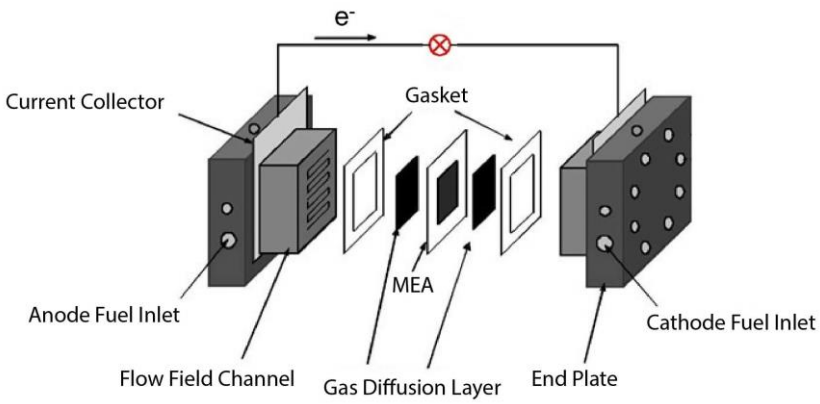

Figure 23 Exploded view of a cell for fuel cell test bench

The MEA used is Gore® A510.1/M820.15/C580.4, anode catalyst loading of 0.1 $mg_{Pt}.cm^{-2}$ and cathode loading of 0.4 $mg_{Pt}\,cm^{-2}$, the membrane is a Gore select with an equivalent weight (EW=grams of membrane per sulfonic acid group) of 820 and 15 µm in thickness . The active area of the cell (MEA) is 10 cm^2.

7. Water tub: Temperature controlled water tub are used to evaporate water used to humidify the gases injected in the cell (air, hydrogen or oxygen).
8. Nafion® humidifiers: Nafion® is highly selective and semi permeable membrane to water but poorly permeable to gases. When one gas is humid, the membrane soaks up the water and the gas exit the humidifier drier than it was. The dry gas on the other side of the membrane takes up humidity from the membrane and exit the humidifier wetter than it was.

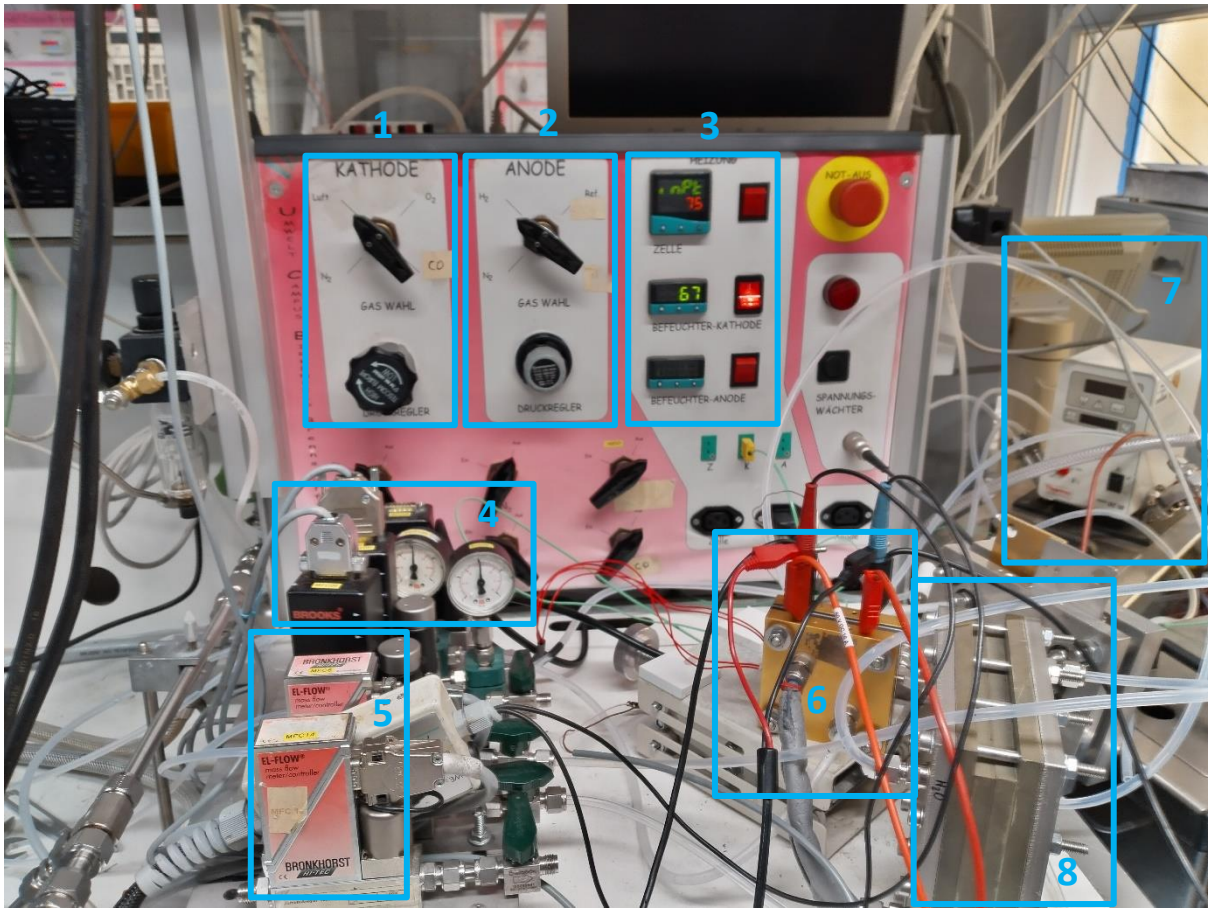

Figure 24 Picture taken of the test bench from Umwelt- Campus Birkenfeld where the sample were characterized

3 RESULTS AND DISCUSSION

3.1 DEPOSITION ON SILICON WAFERS

In this section we show the results published in VACUUM (Elsevier)[185]. The samples were deposited from a mixture of CH_4 and CF_4 in the PRODOS machine on 8-inch silicon wafers. The purpose of this section is to describe the films deposited from a physico-chemical point of view. Interesting results were found regarding the hydrophobicity and crystallinity of the samples. In order to study these various aspects, 10 samples were produced varying the ratio of CF_4/CH_4, the temperature of the substrate and the total flow of feeding gases. Other parameters remained unchanged through all the processes and were set as follow: showerhead temperature (200°C), chamber wall temperature

(125°C), deposition time (20 min), absolute pressure in the chamber (~0.25 mbar). The list of samples is described in the following table.

Table 8 Tabular description of the process parameters of the deposited samples

SAMPLE	$CF_4/(CF_4+CH_4)$ (%)	SUB. TEMP. (°C)	TOTAL FLOW (SCCM)	PLASMA POWER (W) *
1	80	0	500	2100
2	80	20	500	2100
3	80	40	500	2100
4	80	60	500	2100
5	70	0	500	2100
6	70	20	500	2100
7	70	40	500	2100
8	70	60	500	2100
9	80	20	250	1050
10	80	20	375	1575

*Samples 9 and 10 have a different plasma power input to maintain a constant X parameter[186] (=W/(feeding gas flow)) of 4.2

3.1.1 Water contact angle

Table 9 Static water contact angle values for all samples

Sample	*1*	*2*	*3*	*4*	*5*	*6*	*7*	*8*	*9*	*10*
Contact angle (°)	127.5	>150	123.2	124.8	>150	147.8	123.4	129.0	120.4	119.5

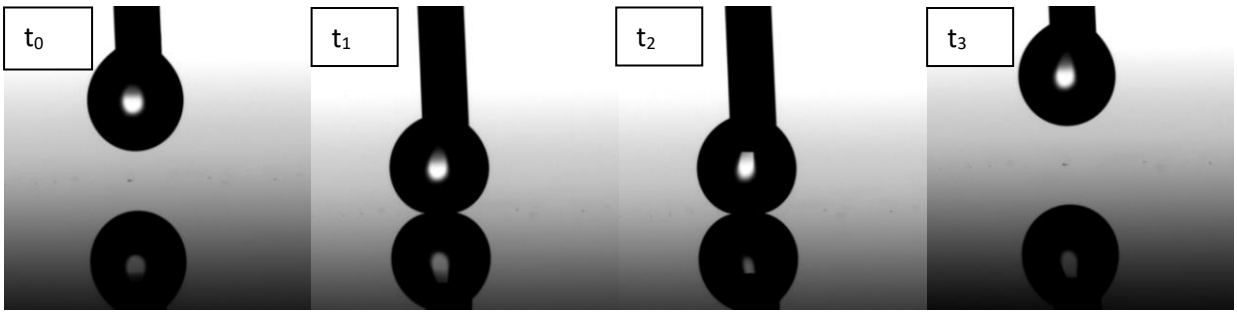

Figure 25 visual representation of WCA for sample 2 and its ultrahydrophobic property showing the 4 steps of the contact angle measurement

Samples 2, 5 and 6 have a contact angle higher than 150° which makes it impossible to calculate an accurate angle as the water drop does not detach from the tip. Figure 25 shows that the static contact angle for sample 2 does not allow the water droplet to adhere to the surface, at t_1 and t_2 the droplet floats over the surface and at t_3 it remained on the tip of the needle rather than staying on the surface.

3.1.2 Scanning electron microscopy

From SEM images we see that depending on the deposition process parameters various surface morphologies emerge (Figure 26. For samples 1 to 4, where the substrate temperature varied (respectively 0°C, 20°C, 40°C and 60°C) while maintaining a CF_4/CH_4 flow ratio of 80%, sample 1 shows the emergence of a certain roughness over the surface due to the growth of sharp bumps type of structures. Sample 2 (substrate temperature set at 20°C) clearly shows the emergence of what we will call *rose petals* structures. These *rose petals* morphologies are not clearly apparent in sample 1, 3 and 4. Sample 1 shows small ridges sticking out of the surface while in samples 3 and 4, dispersed granules can be observed. When we decrease the CF_4/CH_4 flow ratio to 70% for samples 5 to 8 and vary the substrate temperature respectively from 0 to 60°C we do not obtain the *rose petals* structures, even when the substrate temperature is set at 20°, but, for all samples, granule like structures appear on the surface. Sample 9 and 10 do not show the occurrence of any particular morphology, the surface is smooth without any specific distinction and are not shown here.

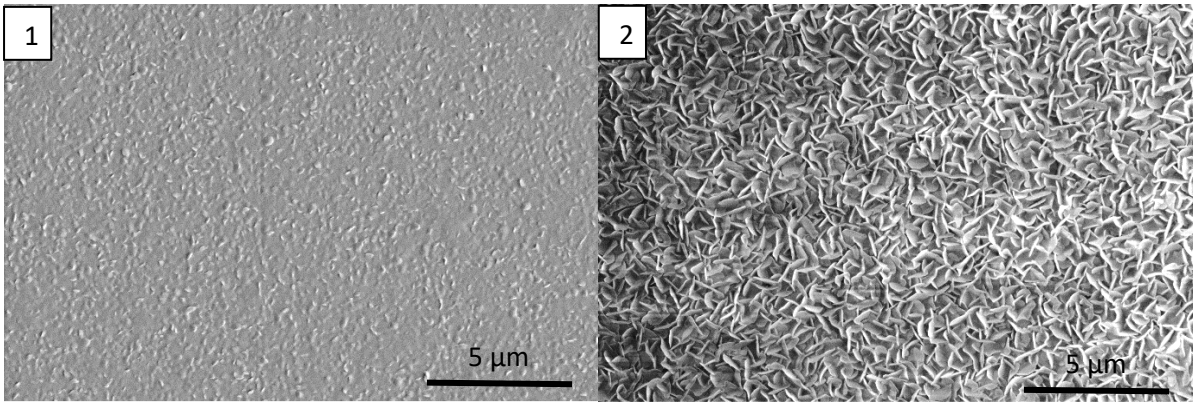

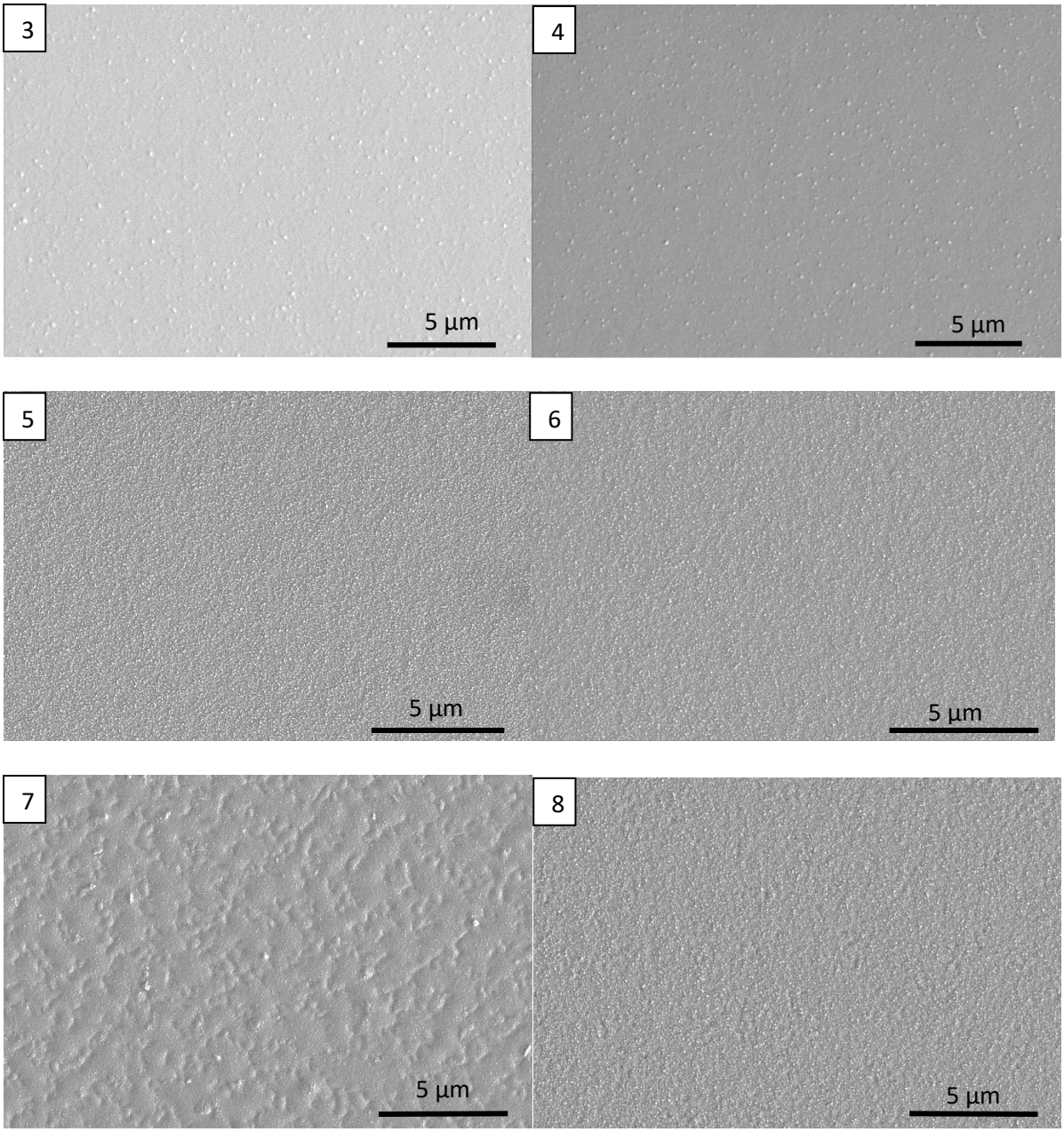

Figure 26 *Top view imaging via scanning electron microscopy for sample 1 to 8, showing how process parameters affect samples surface morphology (see text for details). Sample 9 and 10 did not show any particular structure and were not added.*

3.1.3 Profilometry

Table 10 Thicknesses of samples estimated via profilometry

Sample	*1*	*2*	*3*	*4*	*5*	*6*	*7*	*8*	*9*	*10*
Thickness (nm)	250	1400	180	113	350	290	120	84	20	37

The thickness of the all the samples was evaluated via profilometry. The results show that with increasing temperature the thinner the deposition for sample 5 to 8, the same pattern exist for sample 1 to 4 except for sample 2 (temperature substrate set at 20°C with a flow ratio of CF_4/CH_4 =80%) which stands out by its thickness that is above 1 µm unlike all the other samples. Samples 9 and 10 have very thin depositions due to the lower feeding gas flows used.

3.1.4 Atomic Force Microscopy

Table 11 Root Mean Square (RMS) roughness estimated via atomic force Microscopy

Sample	*1*	*2*	*3*	*4*	*5*	*6*	*7*	*8*	*9*	*10*
RMS (nm)	12.4	103.2	10.1	10.1	31.5	31.4	11.2	21.7	6.8	5.3

The roughness of the samples was estimated via topography AFM and we see that there is a correlation with the results of WCA. The samples with the highest water contact angles (2,5 and 6) have the roughest surfaces. Sample 2 (temperature substrate set at 20°C with a flow ratio of CF_4/CH_4 =80%) stands out again with the roughest surface which is due to the *rose petal* structures showed in the electron microscopy results.

3.1.5 X-ray photoelectron spectroscopy

XPS spectra (Figure 27) show that the ratio of CF_4 to CH_4 drastically alters the chemistry of the film. A $CF_4/ (CF_4+CH_4)$ ratio of 80% results in a film made out of $-CF_2-$ and $-CF_3$, from this result we expect our film to be made out of small oligomer fragments with the chemical formula $CF_3(CF_2)_nCF_3$ with n≈16. Decreasing the $CF_4/ (CF_4+CH_4)$ ratio to 70% for samples 5 to 8 by increasing the inlet flow of methane (150 sccm) and decreasing the flow of tetrafluoromethane (350 sccm) tends to increase the degree of crosslinking with -CF- and $-C-CF_x-$ groups incorporated. The latter also shows a large amount of aliphatic carbon incorporated in the films which can either be due to the incorporation of aliphatic carbon groups in the fluorinated polymer or the deposition of carbon dust agglomerates independent of the of the rest of the film. The second hypothesis is very likely as the films showed black dust that could easily be washed away from the surface of the silicon wafer.

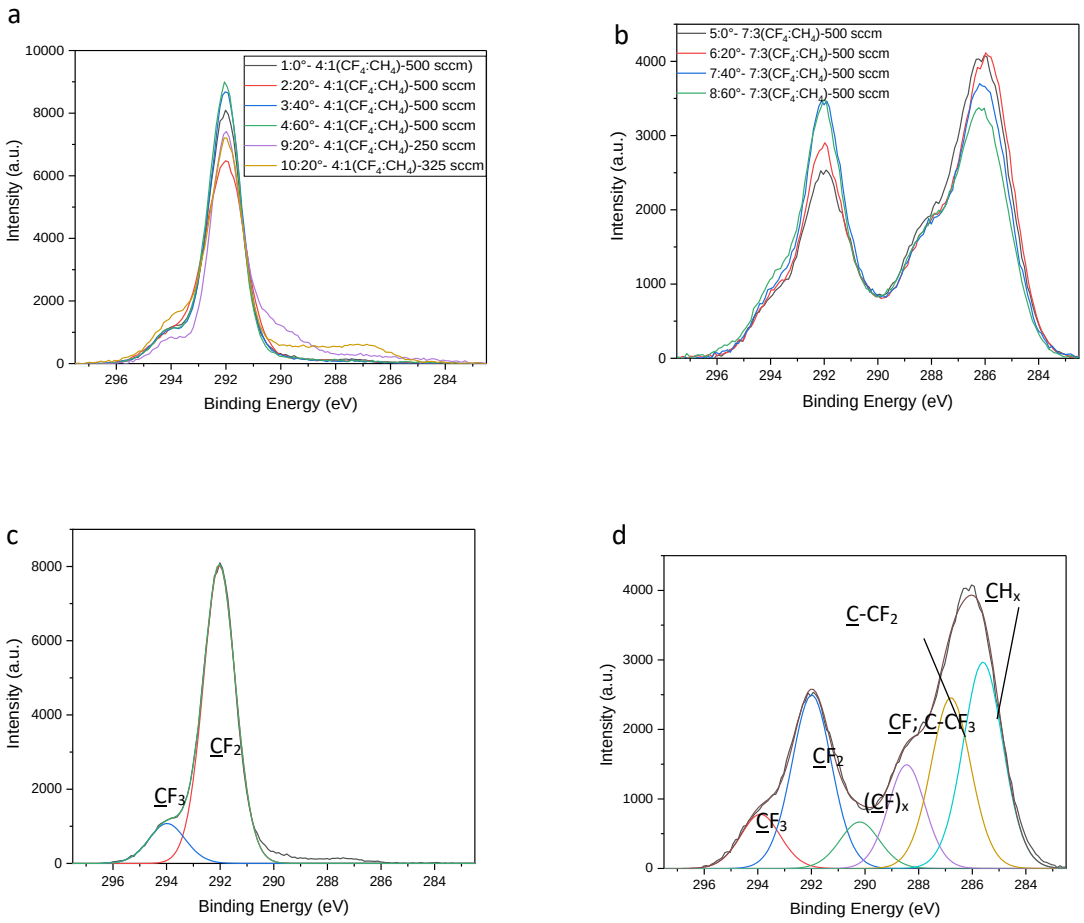

Figure 27 C1s spectra of the series (a) 1 to 4; 9-10, (b) 5 to 8, deconvolution for samples (c) 1 and (d) 5. Peaks were attributed accordingly following ref. [187,188]

3.1.6 X-RAY DIFFRACTION

Figure 28 shows that out of all 10 samples only one of them (sample 2) sees the occurrence of a well-defined crystalline phase. The peak at 2θ=18° was attributed to the (100) plane of the $(CF_2)_n$ crystalline matrix [189,190] with a degree of crystallinity of 43%. The Scherrer formula gives us a crystallite size of 29.4±1 nm. Sample 2 is considered to be crystalline while all the other samples are amorphous.

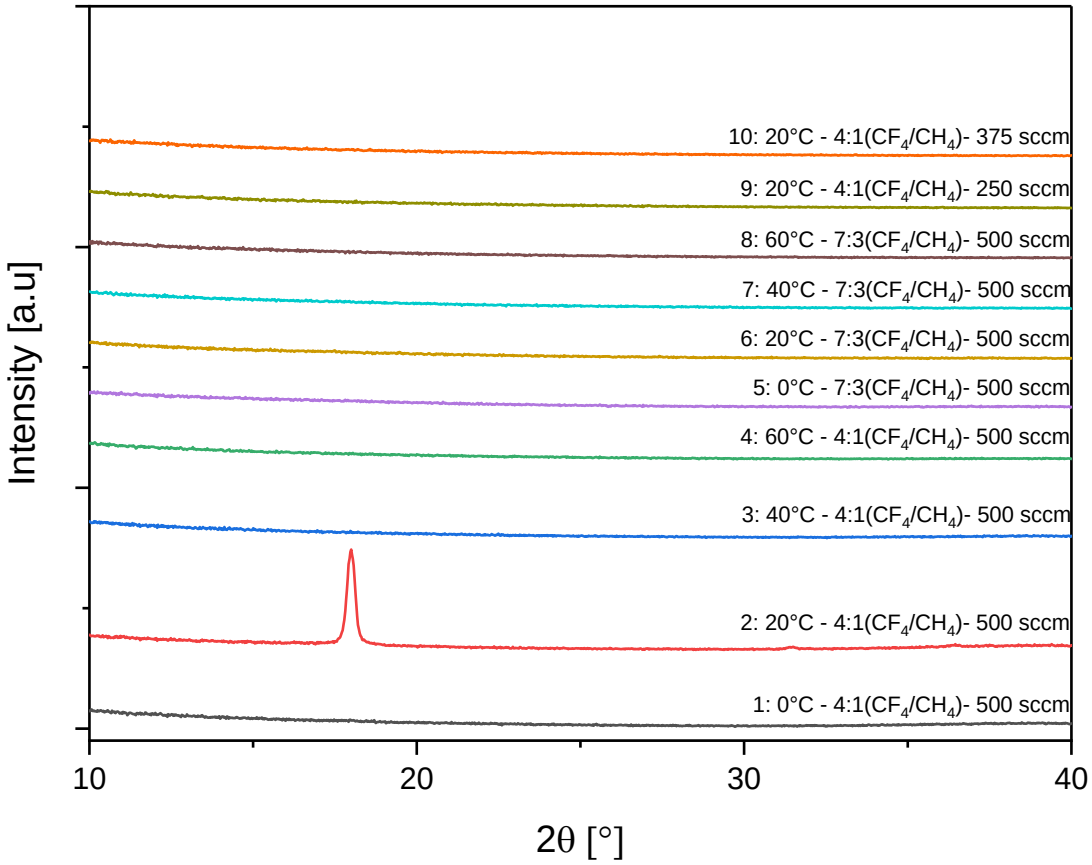

Figure 28 XRD spectra of samples 1-10 for 2Θ ranging from 10 to 40. This figure shows the occurrence of a crystalline phase for sample 2 while the others are amorphous.

3.1.7 Discussion

From the static contact angle measurements, the hydrophobicity varies depending on the process parameters. Correlating those results with the top view imaging of the same samples we determined that ultrahydrophobicity is due to the growth of structures roughening the surface for sample 2, 5 and 6. We postulate that a Cassie-Baxter type of hydrophobicity is occurring for those three samples. Long term storage did not affect the morphology of the deposition nor the wettability after 2 months and a heating test carried out at 80°C for 2 hours. Many other studies observed the same type of wetness behaviour when films are deposited via plasma techniques which is not necessarily correlated with fluorine chemistry but also with siloxanes[191], carbonaceous film from methane[192,193], with acetylene[194]. Surfaces with homogeneous chemistry show a Cassie-Baxter type of wetness due to the filling of the grooves with air and the hydrophobic nature of perfluorinated compounds.[195] The

estimation of the roughness via AFM gives us a hindsight of how it can affect the water contact angle of our samples. Indeed, the samples with the highest roughness's (2,5 and 6) also showed the highest water contact angle, with a specific attention to sample 2 that shows an RMS of 103.2 nm (and a contact angle >150°) which is much higher than any other sample.

XPS results gives us a hindsight in the chemical structure of the films. We can separate the chemical structure of the samples with a CF4/(CF4+CH4) ratio of 80% (samples 1 to 4, 9 and 10) from the ones with a CF4/(CF4+CH4) ratio of 70% (samples 5 to 8). The samples with 80% ratio showed C1s peaks representative of -$\underline{C}F_2$- and -$\underline{C}F_3$ units, from which we can assume that the film is made out of oligomeric linear chains with the chemical structure $CF_3(CF_2)_nCF_3$ with n being around 16 repetitive units. We also observe that little to no change stems from the variation in substrate temperature or the variation of total feeding gas flow. The samples with 70% ratio showed the occurrence of C1s -$\underline{C}$F- as well as -$\underline{C}$-CF_x- peaks which account for the ramification in the chemical structure in opposition with the first series of samples. The same samples also show a large amount of aliphatic species which can either be incorporated in the perfluorocarbon chains or as carbon particles which contaminate the film, this second hypothesis is more likely as the films were dusty and could easily be washed with water to remove black carbon dust. Long term storage did not affect the chemical structure of any of the depositions and remains the same even after 2 months and a heating test carried out at 80°C for 2 hours. This shows the chemical stability of the depositions can be due to the stability of fluorocarbons and the strength of the C-F bond (105.4 kcal/mol)[196] as opposed with plasma carbonaceous films that can undergo oxidation due to air exposure[194]. We assumed that, due to the remote plasma process, the formation of those oligomers happens only in the gas phase and deposit on the substrate without reacting further on the substrate surface. In order to confirm this allegation further studies should be carried out in reactors equipped with a laser induced fluorescence probe[172,173] to study the evolution of the gas composition in the axis from the plasma chamber to the substrate surface, which unfortunately we did not have during the course of this thesis.

XRD reveals the occurrence of crystalline structures in one film. Sample 2 shows a large peak at 18° which is attributed to the stacking of -CF_2- while the other samples are amorphous, hence the attribution of the formation of crystals to the temperature of the substrate. Since this crystalline growth occurs at 20°C but doesn't happen for lower or higher temperatures we hypothesize that a nucleation process is taking place with a maximal growth rate around 20°C. The thickness of the same sample was much higher than the other samples, which shows that the crystallization increases the growth rate of the deposition as opposed when samples are not crystalline. The roughness of that specific sample was drastically higher than the other samples due to the *rose petals* structures formed during the crystallization process. Gas to solid heterogeneous nucleation happens when the target

substrate has a specific temperature[197] and when there is a supersaturation of the partial pressure of the deposited component.[198,199] As samples 9 and 10 do not show the occurrence of a crystalline phase, we can assume that the quantity of feeding gas would account for the supersaturation of the gas phase with $CF_3(CF_2)_nCF_3$ oligomers in the deposition chamber. The second series of sample show a certain degree of ramification/branching and did not show the occurrence of a crystalline phase. For this reason, we postulated that the ramification of the oligomeric chains prevented the crystallization from happening which is commonly observed with other type of polymer materials[200,201] The *rose petals* like structures observed in Figure *26*(2) are the grains resulting from the crystallization of the linear oligomers and the resulting roughness as well as the fluorinated chemistry account for the ultrahydrophobicity of the material. Though the material is easily scratchable, the aging test carried out for 2 months and at 80°C for 2 hours did not impact the chemical structure, the wettability nor the morphology of the samples.

3.2 Deposition on Carbon cloths

In this section we show the results of the films deposited from a mixture of CH_4 and CF_4 in the PRODOS and described from a physico-chemical point of view in the previous section but deposited on carbon fibres fabric. The characterization of the carbon cloths with the film and the application as a gas diffusion layer were investigated. All the samples were pre-treated with oxygen in Reactive Ion Etching (RIE) to clean the organic contamination and the dust that accumulated on the carbon cloth. Three samples were produced, the uncoated and pre-treated carbon cloth with oxygen (without deposition on it), the sample deposited with a substrate temperature of 20°C and 40°C. The decision for these two sets of parameters was to obtain one sample with the *rose petals* structures observed in the previous section and one with a smooth deposition. The idea is to assess the difference between the behaviour of the GDL when the *rose petal* structures are formed and when they are not to see whether the increase in hydrophobicity (ultra-hydrophobicity of the crystalline deposition) increase the performance of a fuel cell with regard to the GDL. The list of process parameters which can be compared with the physico-chemical analysis of the previous section are listed in the following table.

Table 12 Tabular description of the process parameters of the deposited samples

Sample	$CF_4/(CF_4+CH_4)$ (%)	Sub. Temp. (°C)	Total flow (sccm)	Plasma power (W)	RIE O_2 treatment
uncoated	-	-	-	-	yes

20C	80	20	500	2100	
40C		40			

3.2.1 X-ray tomography

X-ray tomography was used to render a 3-dimensional mapping of the carbon cloth fabric. Originally, we wanted to observe the fluorinated deposition onto the carbon fibres fabric but the resolution limit of this technique is in the order of 1 µm and we could not observe the film. We later moved to HIM-SIMS technique to cope with this limitation and we will see the results in a section below. The 3D imaging of the carbon fabric is rendered well, the woven fabric is clearly visible and individual fibres are also observed.

a

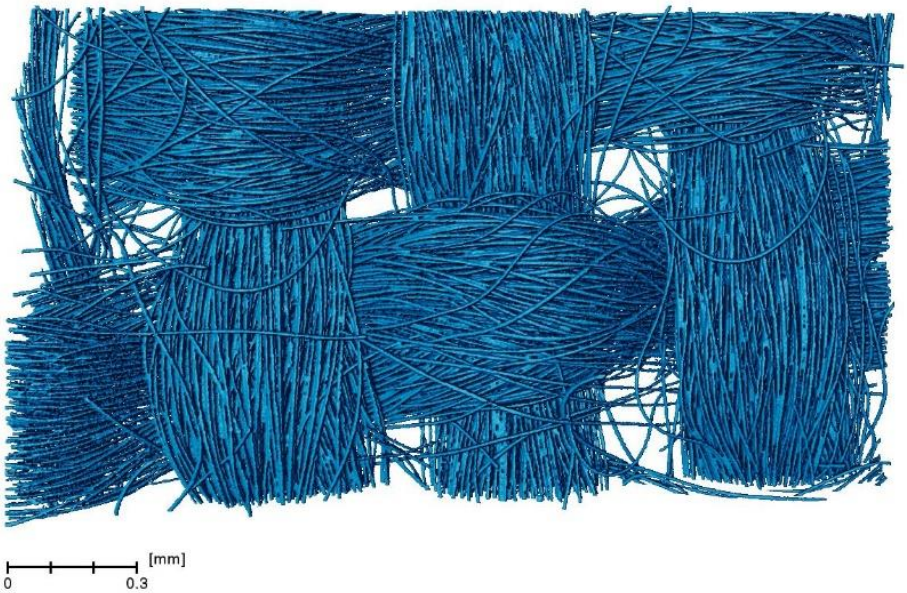

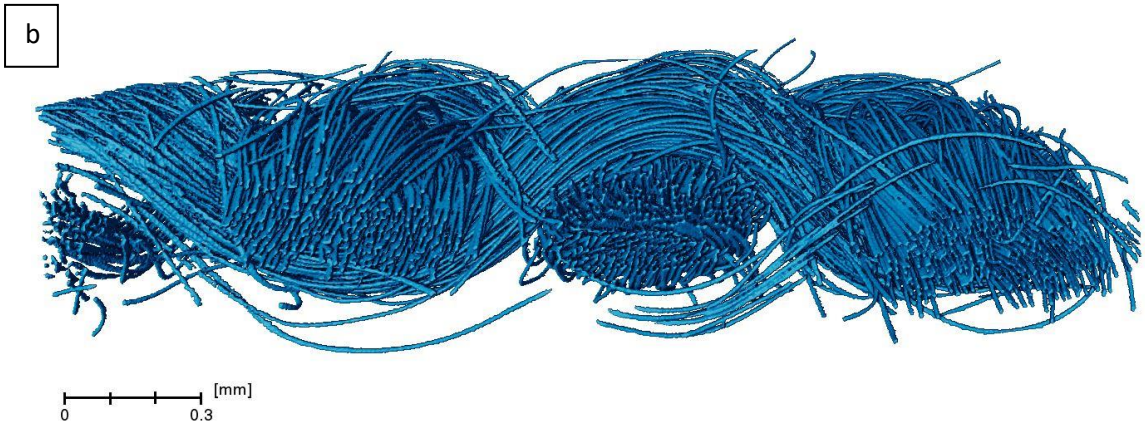

Figure 29 3D imaging of carbon cloth based material with X-ray tomography as (a) top view, (b) cross section

3.2.2 Scanning electron microscopy

The electron microscopy was used to obtain high resolution images of the fabric to compare the uncoated, 20C and 40C samples. Many images were taken for this purpose and there was a huge variation from the observation made from one fibre to another one. For the sake of clarity and consistency we, here, show the image of only one fibre from the uncoated fabric because we could not observe any difference from one fibre to another one. For sample 20C and 40C we show one image from the upper part of the fabric (with regard to the deposition, the upper part means the fibres that were closer to the showerhead) and deeper in the fabric (again with regard to the line of sight from the showerhead). Sample 20C shows the occurrence of *rose petals* that we observed in the deposition on silicon wafers on the upper part of the fabric, the deeper image also shows the occurrence of these structures but far less numerous and less dense. For sample 40C, the upper side of the fabric shows the occurrence of wrinkles at the surface of the fibres while the deeper part look like the uncoated fabric with no particular observation. From these pictures we can estimate that the deposition is different with regard to depth in the fabric. The picture provided have clear evidence of a difference between upper side and deeper side but there is actually a broad spectrum of differences between the fibres, the general trend though, seems to have the structure formed on the upper part disappear deeper in the fabric.

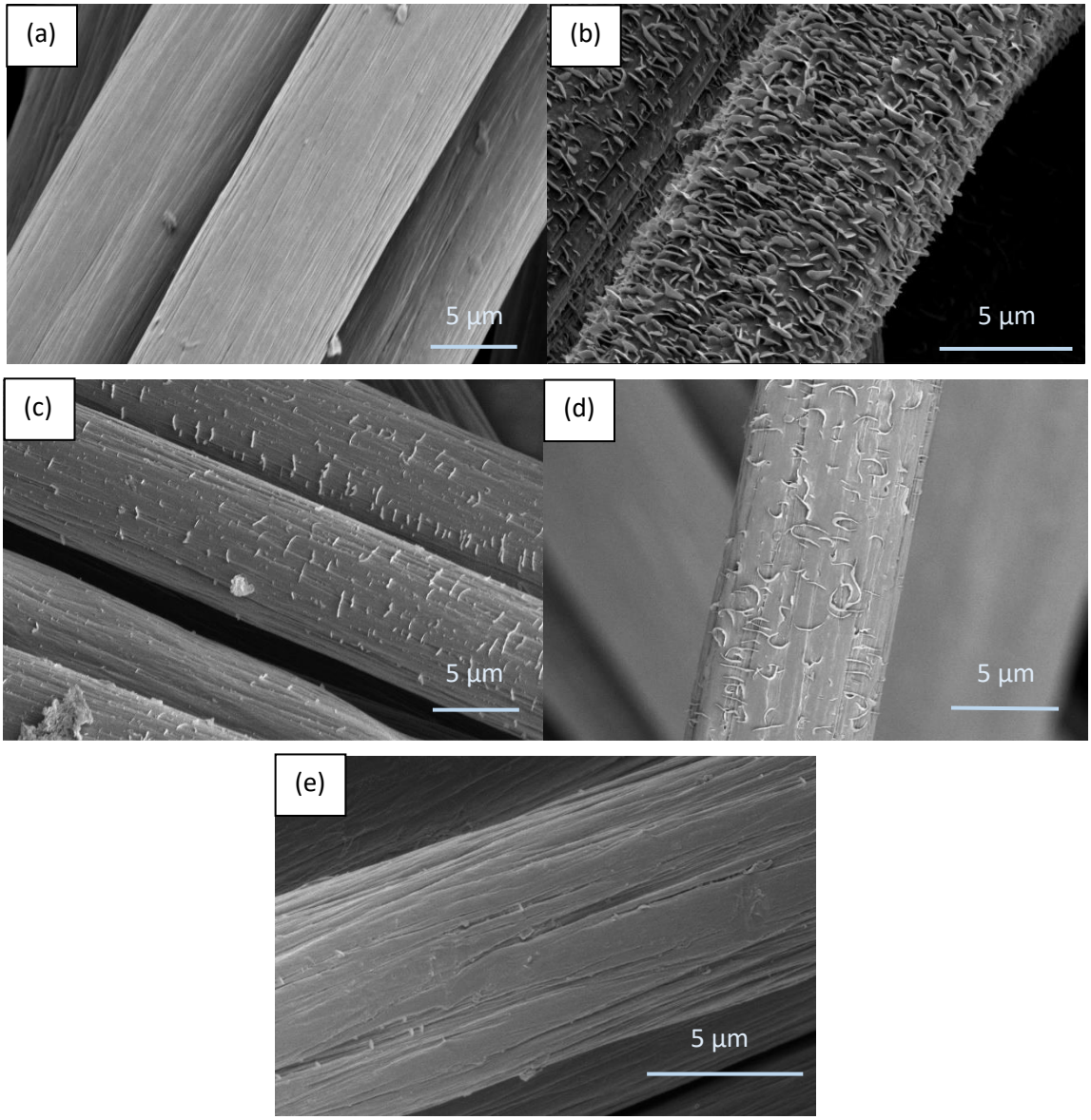

Figure 30 SEM imaging of uncoated carbon cloth fibres as purchased (a), with deposition of perfluorocarbonated material at 20°C on the upper part of the fabric (b) and deeper in the fabric (c), with deposition of perfluorocarbonated material at 40°C on the upper part of the fabric (d) and deeper in the fabric (e).

3.2.3 Helium Ion Microscope coupled with a Secondary Ion Mass Spectrometer (HIM-SIMS)

The HIM-SIMS technique was used to have an elemental mapping of fluorine in the cross section of of the carbon fibres fabric. The analysed zone was capture via scanning electron microscopy before performing the simultaneous detection of F^-, C_2^- and Cl^- ions. While the fluorine was used as the elemental signature of the deposited film, the carbon was also detected to probe the overall carbon content present in the scanned area. Chlorine detection is used as a control of contamination usually

inherent in the resin used to embed the fabric and as a negative control of the preparation artefacts. Several areas were probed for each sample to assess the depth profiling of the deposition on the carbon fabric. To better visualize the position of the scanning area in the depth of the fabric, a reference of the 3-dimensional imaging of the fabric with X-ray tomography is provided.

3.2.3.1 Uncoated fabric

In the case of the uncoated fabric, fluorine is not observed as expected, carbon is detected in the whole scanning area and chlorine is detected in the resin but not on the fibres. Sometimes the carbon detection can be brighter at the interface between the fibres and the resin, this is usually due to the preparation of the samples that is a hard mechanical polish of the cross section.

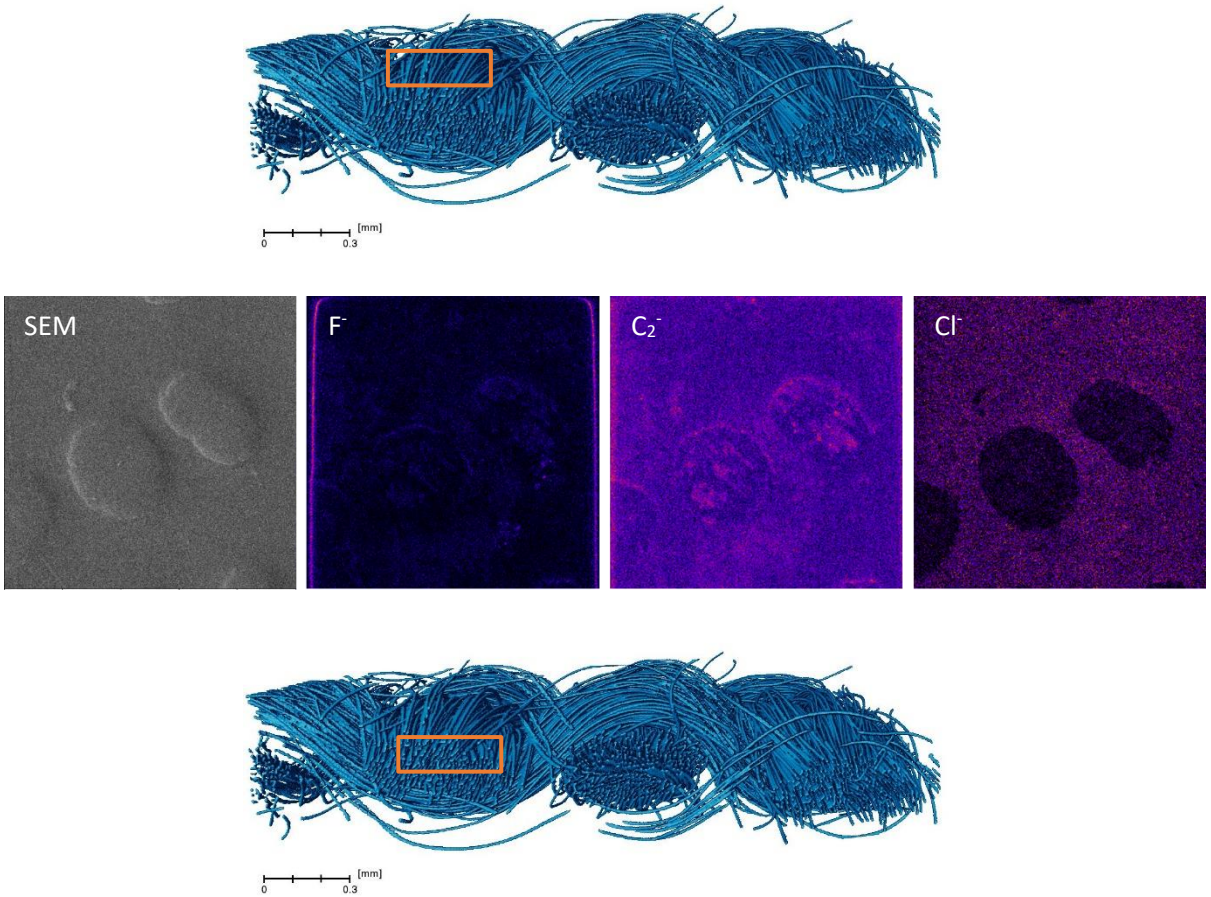

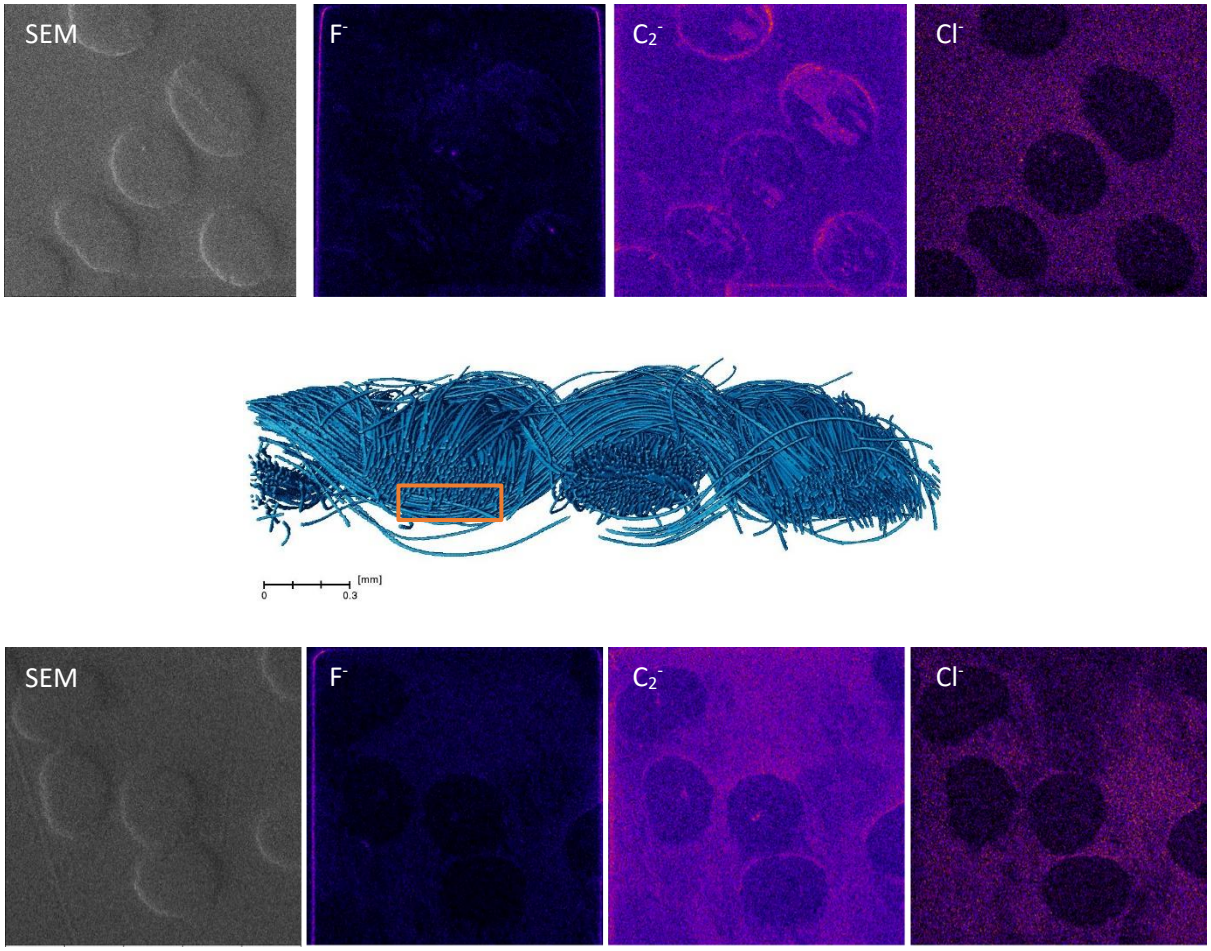

Figure 31 Cross section elemental analysis by HIM-SIMS including SEM image, Fluorine, Carbon and chlorine with varying depth for uncoated sample

3.2.3.2 Fabric coated with perfluorinated film deposited at 20°C

When we scan the cross section of the fabric with the deposition of perfluorinated films, fluorine is the element we focus on to assess the thickness and the homogeneity of the depositions. We can see that the deposition is non line of sight and wrap around the fibres across the whole depth profiling. The thickness in depth profiling was evaluated using ImageJ software. The upper section had a deposition of 324±59, the middle part 400±123 nm and the lower section 372±97 nm. With these results we cannot say if there is an actual evolution in film thickness in the depth of the fabric.

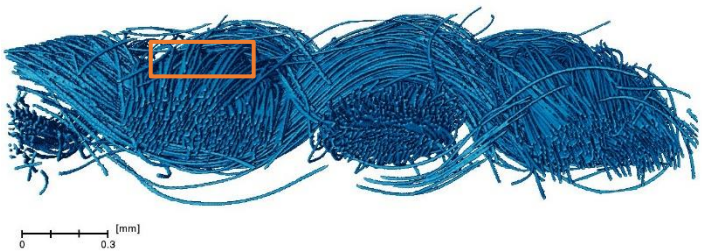
[mm]
0
0.3

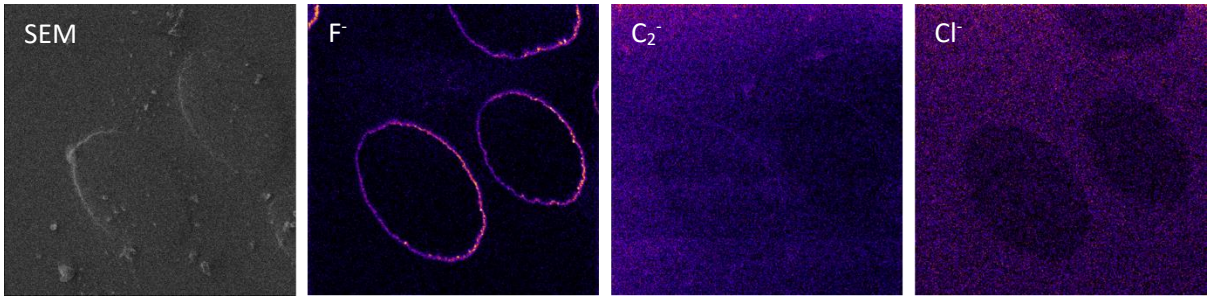
SEM
F-
C2-
Cl-

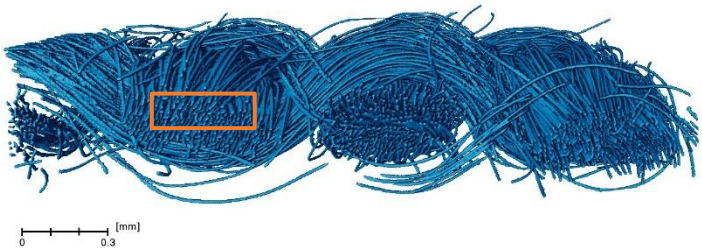
[mm]
0
0.3

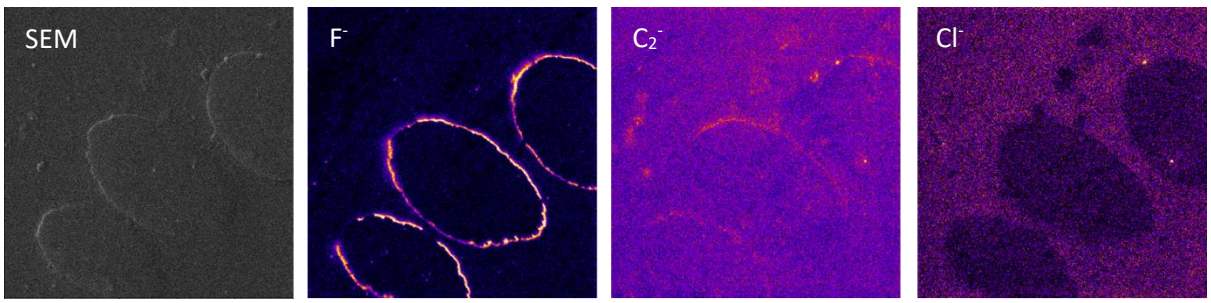
SEM
F-
C2-
Cl-

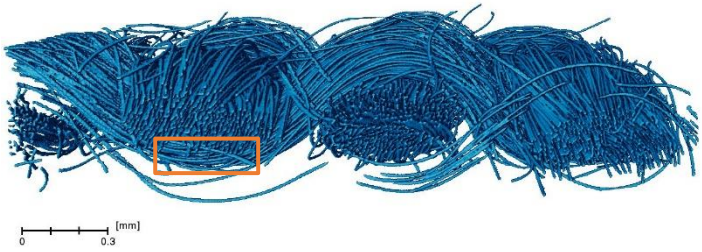
[mm]
0
0.3

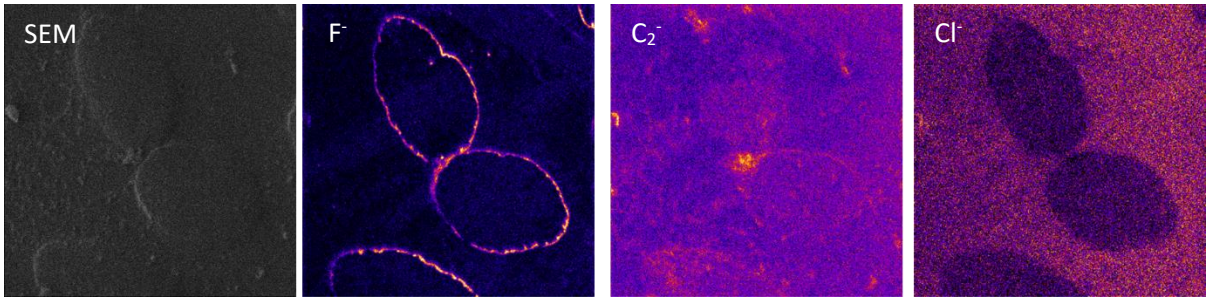

Figure 32 Cross section elemental analysis by HIM-SIMS including SEM image, Fluorine, Carbon and chlorine with varying depth for sample 20C

3.2.3.3 Fabric coated with perfluorinated film deposited at 40°C

When we scan the cross section of the fabric with the deposition of perfluorinated films, fluorine is the element we focus on to assess the thickness and the homogeneity of the depositions. We can see that the deposition is non line of sight and wrap around the fibres across the whole depth profiling. Sometimes the Chlorine is visible between fibres and the resin, this is due to the preparation method which adds some contamination detected by the technique. The thickness in depth profiling was evaluated using ImageJ software. The upper section had a deposition of 413±111, the middle part 328 ±111 nm and the lower section 271±71 nm. With these results we cannot say if there is an actual evolution in film thickness in the depth of the fabric.

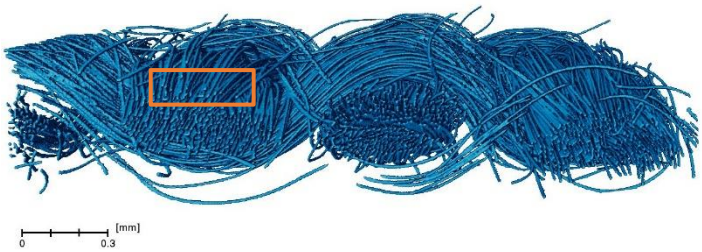

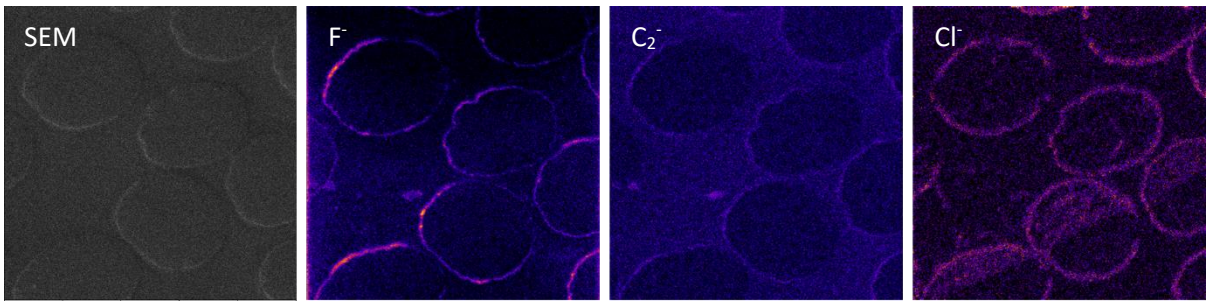

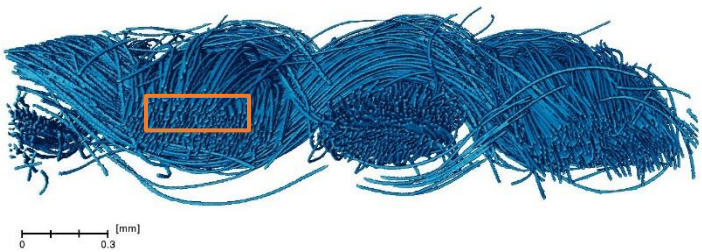
0
0.3
[mm]

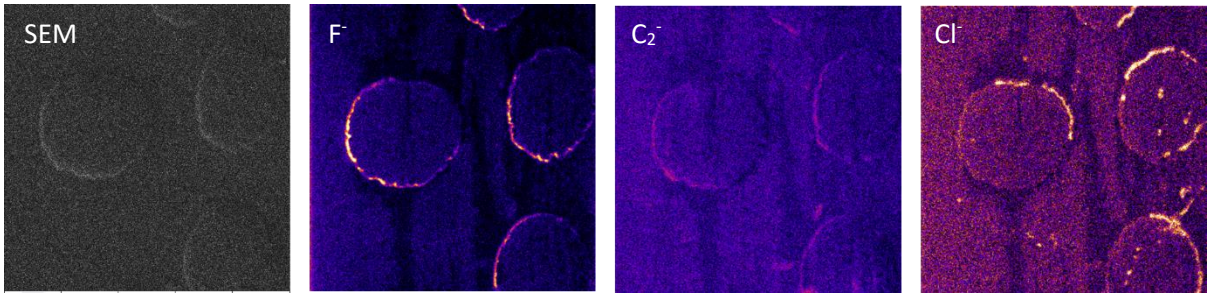
SEM
F-
C2-
Cl-

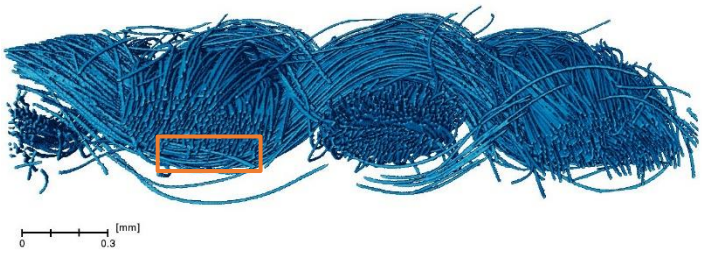
0
0.3
[mm]

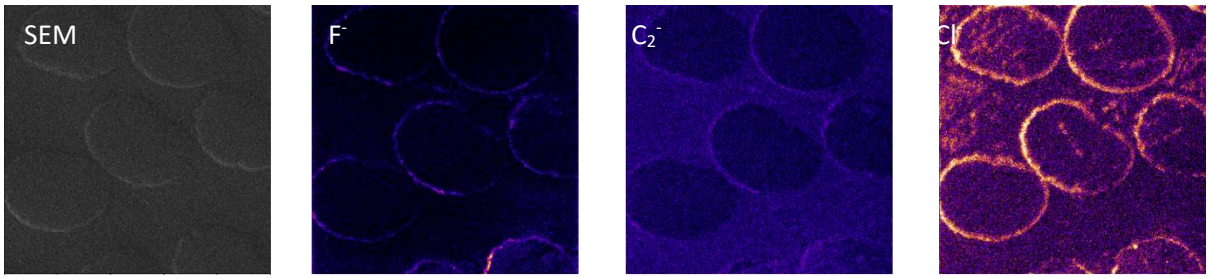
SEM
F-
C2-
Cl-

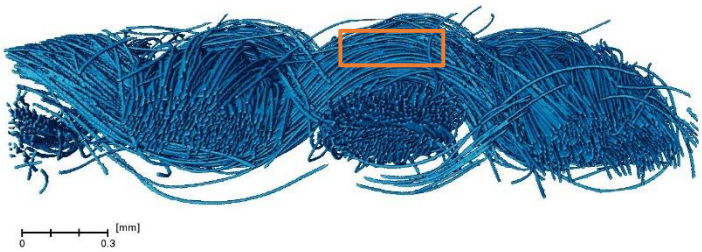
0
0.3
[mm]

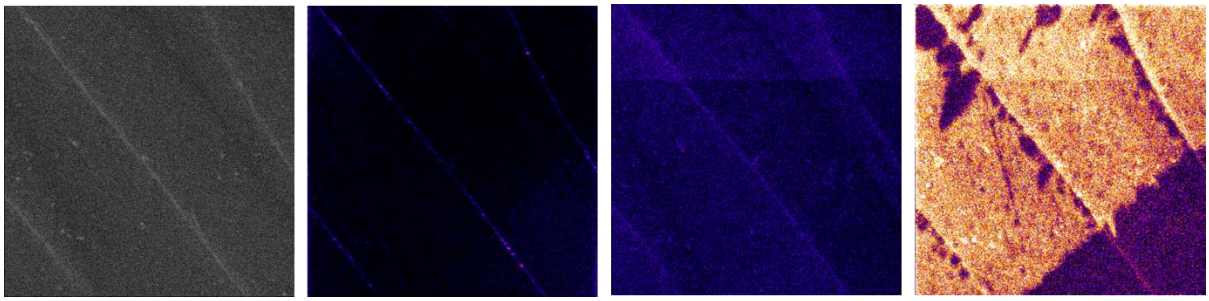

Figure 33 Cross section (and longitudinal) elemental analysis by HIM-SIMS including SEM image, Fluorine, Carbon and chlorine with varying depth for sample 40C

3.2.4 Scanning electron microscopy in atmospheric chamber

Electron microscopy in atmospheric chamber allows for the injection of water vapour in the chamber and the germination of water droplets on samples. Here we used this technique to assess the behaviour of water on the carbon fibres fabric at the microscopic level. Two samples were investigated (uncoated and 20C), and the results are shown below. Both samples show very different behaviours. A capillary effect seems to take place with water being drain within the thread of carbon fibres with the uncoated sample. Sample 20Cs shows a poor interaction with water, as the droplets remain round and appear to be squeezed in between the fibres. These results highlight the highly hydrophobic nature of coated fabric with perfluorinated films compared to uncoated fabric when water droplet is formed by condensation of water vapour which is how liquid water form in fuel cells[202].

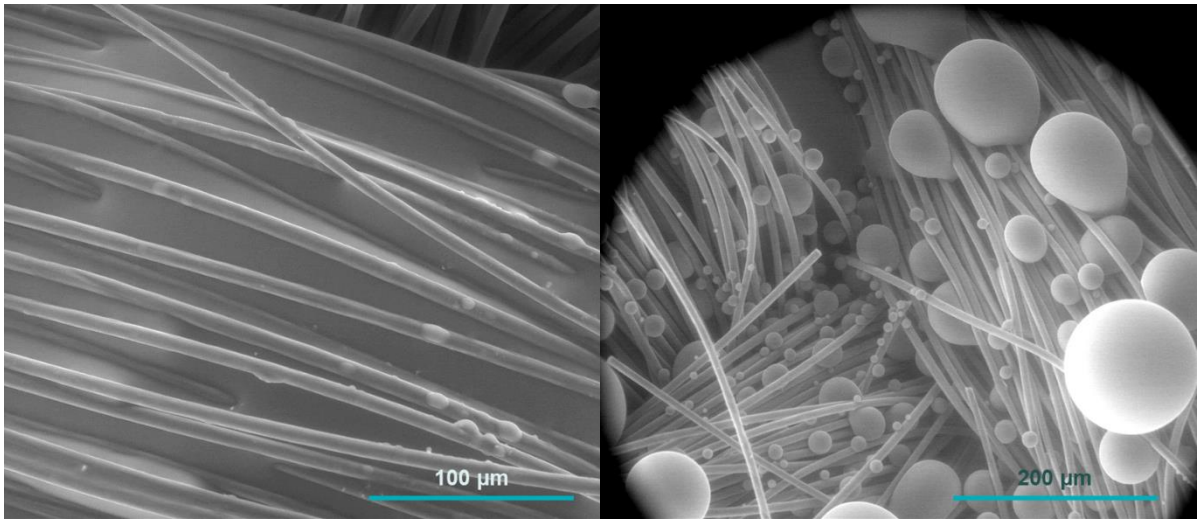

Figure 34 Environmental SEM imaging with condensed water vapour on uncoated sample and sample 20C

3.2.5 Conductive Atomic Force Microscopy (cAFM)

The cAFM allow us to investigate the conductivity with regard to the position on fibres. The topographic imaging is not provided as the curvature of the fibres does not allow a good resolution. The uncoated sample shows the highest conductivity with 3784 nA which is expected as carbon fibres are highly conductive. The lowest conductivity was observed for sample 40C with 3275 pA, here we expected a low conductivity as the fibres are wrapped in perfluorinated film as seen with HIM-SIMS analysis which is a insulator. An interesting result was obtained for sample 20C which has a lower average conductivity than the uncoated sample as expected but higher than 40C unexpectedly. The explanation resides in the specific rose petal structures observed with the scanning electron microscopy. When we look at the conductivity mapping in Figure 35b we see elongated nonconductive areas interlaced with elongated conductive areas. We can assume that rose petals made of perfluorinated material are the black nonconductive area and in between those structures, the tip of the AFM was in contact with leaner film regions which makes it less electrically resistive than thicker rose petal regions.

Table 13 Average conductivity of samples measured over 4 x 4 µm² surface on fibres

SAMPLE	AVERAGE CONDUCTIVITY
UNCOATED SAMPLE	3784 nA
20C	161 nA
40C	3275 pA

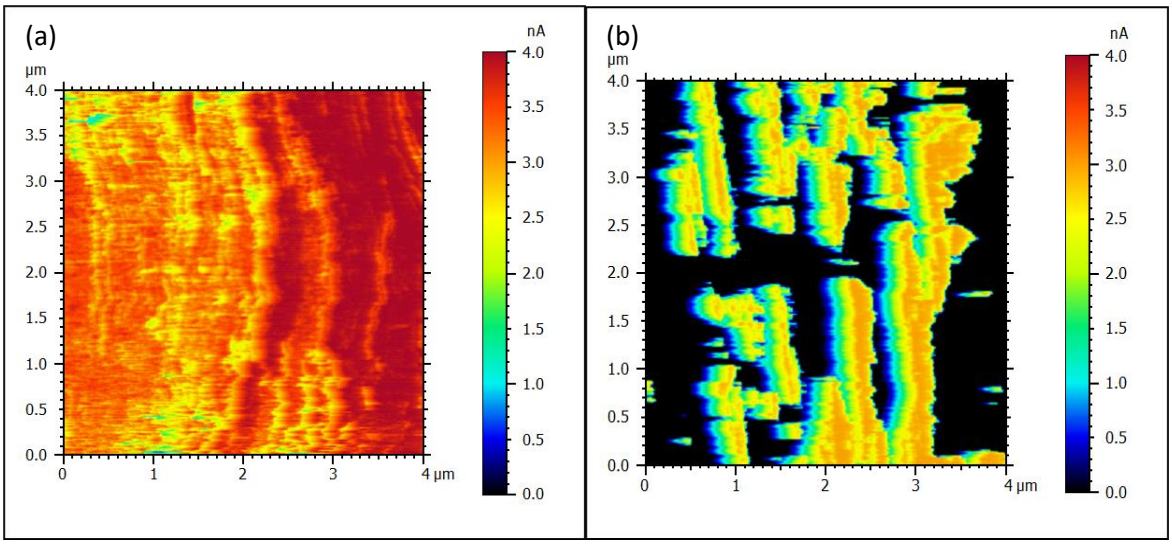

(c)

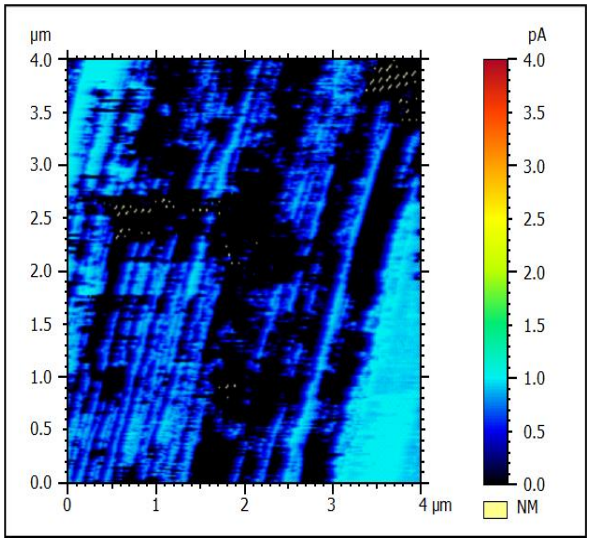

Figure 35 Spatially resolved conductivity on carbon fibres in logarithmic scale for (a) uncoated sample, (b) 20C sample and (c) 40C sample

3.2.6 Gas diffusion layers in test bench

The purpose of testbench testing is to assess the behaviour of the cell in situ when we change the gas diffusion layer. A typical polarization curve for fuel cells is given in Figure 36. The standard electrode potential for the ideal thermodynamic fuel cell voltage is 1.23 V. At the OCV (open circuit voltage) no current is drawn from the cell and the voltage is maximal with a drop from the ideal thermodynamic state which is due to gas cross over (hydrogen and oxygen crossing the fuel cell in their native state). At low current density, the activation region is related to the kinetic limits of the chemical reaction. At moderate current density, the drop in voltage occurs due to ohmic resistance of transport of protons and electrons through the various components of the fuel cell. At high current density, the gas transfer to the electrodes is slow at supplying the gases sufficiently and removing water quickly which leads to a depletion of the reactants at the catalyst interface and a accumulation of water resulting in a further drop in voltage.[203] Thus we obtain the following equation for fuel cell voltage:

$$V_{cell} = E_{th} - v_{act(cath)} - v_{act(an)} - v_{ohm} - v_{mt(cath)} - v_{mt(an)}$$

Where v_{act}, v_{ohm}, v_{mt} represent activation, ohm resistance and mass transport polarization. Every component of the fuel cell plays a role in this overall equation. In order to optimize this, each and everyone of them should be carefully optimized to decrease the drop in voltage when current density is increasing. Here we are looking at how gas diffusion layers can alter the polarization curve with regard to their nature.

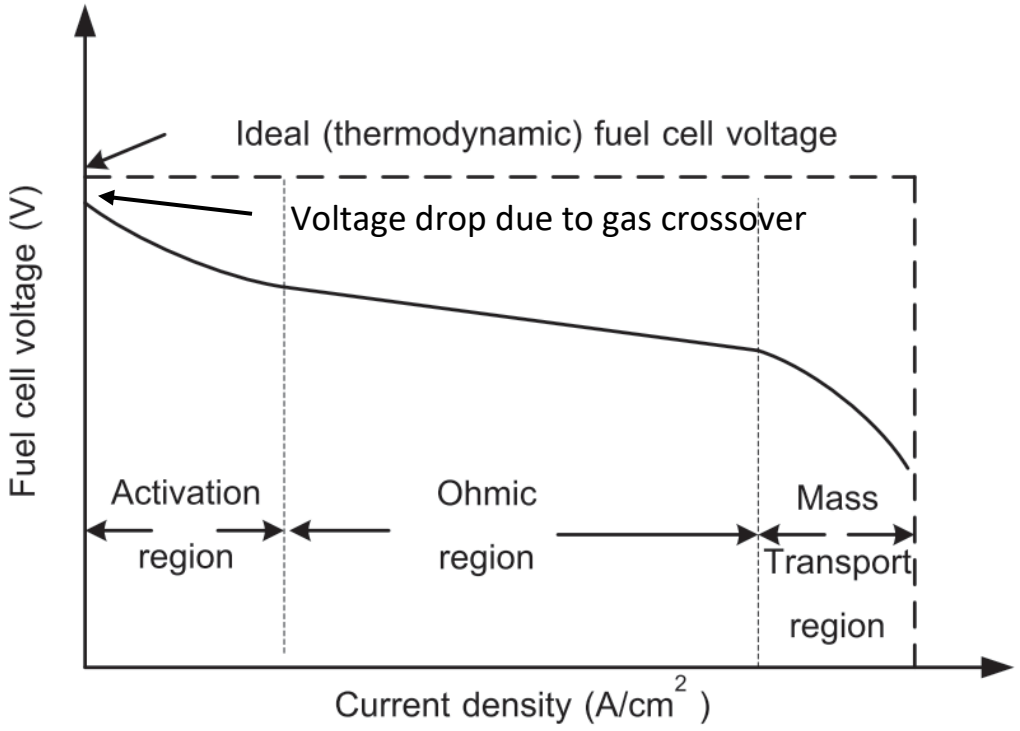

Figure 36 Typical polarization curve given for fuel cell including the various contribution of voltage losses with increasing current density draw[203]

The three samples were tested simultaneously on the anode and the cathode side at two level of gas humidification each with a cell temperature kept constant at 75°C. The humidification level is referred to in water bath temperature, the higher the temperature, the higher the feeding gases (hydrogen and oxygen) humidification (see material and method) and the higher the humidification of the membrane. All the components of the cell were the same throughout the test except for the gas diffusion layers which are the samples we are studying. When look at Figure 37, the first striking evidence is that the gas diffusion layer plays an important role in fuel cells and their nature should not overlooked and optimized to give the best performances. The three samples make the fuel cell react quite differently, sample 20C has a steady drop in the ohmic loss region while the two other samples have a drastically higher loss in the same region. For sample 20C and 40C, the increasing the temperature of humidifiers allows for better performances of the fuel cell over the whole spectrum

of current density probed. For the uncoated sample though, the difference is not so obvious and the tendency to drop in voltage at higher current invert the position of the two curves. Surprisingly, sample 40C shows worse performances compared to the uncoated sample. We will discuss the results in the next section and provide with elements of information's on the behaviour of the fuel cell with regard to the GDL used.

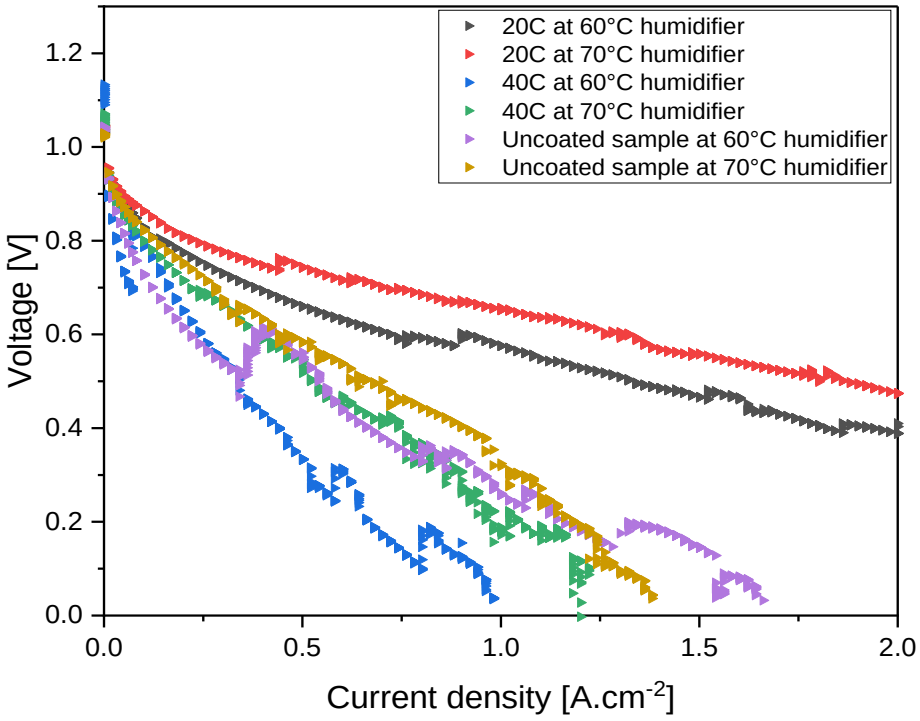

Figure 37 Uncoated, 20C and 40C samples are tested in a fuel cell test bench at two different level of feeding gases humidification to probe the behaviour of the cell on a polarization curve.

3.2.7 Discussion

For this 4th section three samples have been synthesized, one control sample that underwent a reactive ion etching with oxygen cleaning, a sample called 20C which underwent the oxygen RIE and a subsequent deposition of perfluorinated film characterized in section 3 maintaining a substrate temperature of 20°C and a sample called 40C that underwent the oxygen RIE and a subsequent

deposition of perfluorinated film characterized in section 3 maintaining a substrate temperature of 40°C.

In section 3, scanning electron microscopy showed that methane and perfluoromethane in specific proportion and a specific substrate temperature show the growth of a crystalline phase and rose petal like structures. In this section the film deposited at 20°C of substrate temperature also showed the occurrence of rose petals structures grown on carbon fibres. At 40°C of substrate temperature the structures disappear just as we saw in section 3 when the film is deposited on a silicon wafer. We also showed that mostly the upper fibres in 20C (with regard to the position in the deposition chamber) show the occurrence of these structures and when we zoomed deeper in the fabric depth, the structures were slowly disappearing. HIM-SIMS analysis revealed that the films were deposited in all the depth of the carbon fabric and showed the non-line of sight nature of the chemical vapour deposition. Both sample 20C and 40C showed a similar thickness with no particular evolution in the depth of the fabric.

Scanning electron microscopy in atmospheric chamber allows to have an insight into the behaviour of water at the microscopic level on the carbon fibres. The samples with a fluorinated deposition (20C and 40C) showed a strong tendency toward hydrophobicity while the uncoated sample showed a tendency toward coating itself with water.

Fuel cell testing station allowed us to test the behaviour of a fuel cell when we used the elaborated GDL's. The uncoated sample showed a sharp drop in voltage over the ohmic region at both humidity level. At the lower level of humidity, a jump in voltage is occurring between 0.4 and 0.5 $A.cm^{-2}$ and proceeded to decrease at the same rate, this phenomenon can be explained by the full hydration of the membrane at that point. At low current density, small water quantity is generated at the cathode to hydrate the membrane and the feeding gases dry up in contact with the hydrophilic gas diffusion layers adsorbing the water as can be seen in atmospheric SEM images. When the feeding gases are more humidified, the jump does not occur due to the sufficient water quantity supplied to hydrate the membrane at low current density. The uncoated sample show a drastic drop in voltage in the ohmic region for both level of humidity, but when we look at the conductive AFM measurements, the fibres are highly conductive hence the drop is not due to the poor conductivity of the GDL material. One can assume that the adsorption of water over the fibres from the humidified gases slowly increase the resistance contact impacting the conductivity of the electrons flowing from the electrodes to the bipolar plates. At higher current density in the polarization curve, the test at lower gas humidity has a higher voltage than the one at higher humidity showing that the more water is adsorbed, the stronger the resistance of the GDL bringing the voltage down to zero. For sample 40C the voltage is dropping

faster than for the uncoated sample. This was surprising as the coating is supposed to improve the water management and improve the performance of the cell but when we carried out the conductive AFM measurement, we realised that the coating was so uniform and poorly conductive that the ohmic losses are incredibly high bringing the voltage down to zero at an early stage. Sample 20C was the most promising one for GDL application as shown with fuel cell testing. The voltage drop in the ohmic region was dropping slowly and steadily with the current density as opposed with 40C sample. The hydrophobic behaviour of 20C is the same as 40C as highlighted by atmospheric SEM but the conductivity was drastically different as shown by cAFM. From the SEM images we see that the rose petals are sticking out of the fibres vertically but in between them, some areas seem uncovered in perfluorinated material as confirmed by cAFM. The measurement showed that fibres had conductive spots located between highly nonconductive areas which are believed to be the rose petals structures. With this dual behaviour type, sample 20C shows a highly hydrophobic behaviour and reduced conductivity compared to the uncoated sample but much higher than sample 40C keeping the conductivity high enough to run the cell. Every sample did not reach a mass transport limitation which would show the water management limitation, on the one hand sample 40C and uncoated are too ohmic resistive and the cell with 20C is performant enough to go to the limit of the test bench which is 20 A.

4 CONCLUSION

In this chapter we showed the results associated with the deposition of perfluorinated films in the PRODOS-200 PVPD™ R&D System from methane and tetrafluoromethane. The PRODOS system is a chemical vapour deposition that uses a remote plasma unit to deposit thin films on 8 inches in diameter substrate. A remote plasma system should be carefully considered as gas phase reactions takes place and the inactivation of species due to gas phase reaction and gas to wall reaction inactivate the active gaseous species. That's why we used a mix of an etching agent (CF_4) and a fast-depositing agent with a high sticking coefficient (CH_4). In a remote plasma, the mix of fluorinated gases and a gas with high deposition rate work against each other, producing surface and gas phase reaction preventing the deposition of a film in the plasma chamber and allowing for a longer life-time of a the generated species in the gas phase. In a remote plasma, several steps will take place from the plasma chamber to the remotely located substrate. Due to its etching properties, CF_4 will prevent the

deposition of an amorphous carbon film (due to the presence of CH_4) while adding fluorinated atoms in the chemical structure of generated volatile species.[172]

The first part of the results includes the physico-chemical characterization of the deposited films that varied with regard to the deposition process parameters (substrate temperature, total feeding gas flow, flow ratio between CH_4 and CF_4). The second part studied the potential use of these films to enhance carbon fibres fabric and their use as gas diffusion layers for PEMFC.

The first part showed the results published in VACUUM (Elsevier)[167]. We studied the deposited films and characterized them with WCA, SEM, profilometry, topographic AFM, XPS, XRD. From these results we showed that the films had various water contact angle ranging from hydrophobic to ultrahydrophobic. Correlating these results with topographic AFM, we could see that the rougher the surface of the deposition the higher the hydrophobicity. Thicknesses were assessed via profilometry and correlated the temperature of the substrate with the thickness of the deposition (the lower the temperature, the thicker the deposition). SEM imaging revealed one very peculiar sample with *rose petals* morphologies at the surface, that sample also occurred to have the highest roughness, the thickest deposition and an ultrahydrophobic behaviour. XPS shows two categories of profiles depending on the feeding gas ratio of CF_4 and CH_4. At a ratio of 80% CF_4, the chemistry of the film is made out of linear oligomeric chains with the formula $CF_3(CF_2)_nCF_3$, while when we have a ratio of 70% CF_4, the chemistry becomes more complex with reticulation of the polymer and the addition of aliphatic groups under the form of carbon black dust. XRD measurement showed us that the one sample showing the *rose petals* structures is crystalline while all the others were amorphous. This led us to think that when linear oligomeric chains are deposited at a specific temperature (20°C) with a sufficiently high enough total feeding gas flow, a nucleation process is taking place forming crystallites that in turns form grains that look like *rose petals*.

The specific purpose for the development of a process to coat surfaces with perfluorinated material finds its roots in the fuel cell field for the gas diffusion layer component. The GDL's are commonly made out of a support of diffusion which undergoes a hydrophobic treatment or the application of a microporous layer. Plasma treatments can be used when one desire conformally coat carbon fibres. The hydrophobization of carbon cloth fabric with the present process was used to produce elaborated gas diffusion layers. A methodology was developed using techniques such as X-ray tomography, SEM, HIM-SIMS, atmospheric SEM, fuel cell test bench and conductive AFM to deeply understand the behaviour of the produce samples as GDL's. High resolution electron microscopy revealed that the *rose petals* structures observed when the film was deposited on silicon wafer also appear on the carbon fibres cloth. HIM-SIMS shows us also that the process coats the carbon fabric in a non-line of

sight fashion wrapping the carbon threads even at the lowest point in the deposition chamber without decreasing the thickness of the deposition. Electron microscopy in atmospheric chamber gives us the hindsight to compare the behaviour when water condensate on the fabric. When no perfluorinated coating is applied the sample tends to soak up the water to wrap the carbon fibres with water while when a coating is deposited, water droplets are formed without interacting with the fibres and are roundly shaped and squeezed between the threads highlighting the high hydrophobicity of the material. Results in testbench allows to probe the behaviour of a fuel cell, our three different samples were successively used in a cell and two tests were carried out at different level of humidity while maintaining a constant cell temperature at 75°C. Initially the idea to hydrophobized carbon fabrics fabric was to enhance the water management of the cell. The control sample (uncoated) shows that the humidity of the gas interacts with the hydrophilic surface and adsorb water which impacts the electrical conductivity of the gas diffusion layer which in turn poison the cell and makes the voltage drop to zero at an early stage. When we take a uniformly coated sample (40C with homogeneous fluorinated film) the behaviour is even worse and the voltage drops quickly to zero, though at higher humidity level a slight improvement is observed. The sample showing the occurrence of *rose petals* on the other, shows a steady behaviour with slow decrease in voltage throughout the ohmic region. The explanation for these two behaviours was explained with conductivity AFM. Sample 40C, having a homogeneous non conductive layer of perfluorinated film has a drastic drop in the ohmic region because of the high resistance to electrical contact in the cell. Sample 20C on the other, having those *rose petals* structures, has conductive area and non_conductive areas, which confers a lower conductivity than when no coating is deposited but much higher than when the film is uniformly deposited. At the end of the day, sample 20C shows a respectful performance without reaching the mass transfer limitation over the range of current used in the test bench owing its good performance to the *rose petals* structure which confer a sufficient conductivity to withstand the high ohmic losses observed with the two other samples.

Chapter III

Prototype design for proton exchange membrane deposition

Proton exchange membranes are the cornerstones of proton exchange membrane fuel cells and the membrane electrodes assembly. They are responsible for the proton conduction and the electronic insulation. Being able to synthesize such material with chemical vapour deposition is highly interesting as the manufacturing of commercial PEM is costly and shows poor yield. This chapter see the design of a new prototype based on remote plasma deposition for the soft activation of perfluoro(3-oxapent -4-ene) sulfonyl fluoride (PSVE) and hexafluoro-1,3- butadiene (HFBD). Each upgrade of the prototype saw improvement in the deposition. The third and last version is the most promising with a quasi-full retention of the PSVE functionality and the successful copolymerization. Another interesting finding was the emergence of the conversion of the sulfonyl fluoride function to sulfonate in a one-step process.

1 INTRODUCTION

In this chapter we are studying the synthesis of proton exchange membrane (PEM) via CVD. PEM are semi permeable membrane made of copolymers composed of repeating units electrically neutral with acidic dangling units covalently bonded to a polymer backbone (e.g. surlyn™ is a resin created by Dupont® and is a copolymer of polyethylene backbone with methacrylic acid has the dangling group).[64] For fuel cell application the reference material remains, as of today, Nafion™ commercialized by Dupont-Chemours® and is a copolymer of polytetrafluoroethylene (as polymer backbone) and perfluoro-sulfonylethoxy propylene vinyl ether (also abbreviated PSEPVE as the dangling group). In general, for FC applications, fluorinated polymers are appreciated due to their chemical inertness and the strength of the C-F covalent bond which increase the lifetime of the membrane[204]. Acidic sulfonate groups are also appreciated due to their strong acidity which allows for an optimal proton conduction through the membrane. Nevertheless, many other types of membrane have been suggested throughout the years such as polystyrene sulfonate, polyimide sulfonate, polyphosphazen sulfonate, polybenzimidazole, polyarylene ether or even natural chitosan based polymers[205]. All these types of membranes work following the same principle, they hydrate creating hydrophobic clusters and hydrophilic ones filled with water. Pure water, being non-electronically conductive but proton conductive, allows for the free passage of proton and maintain electrical neutrality.

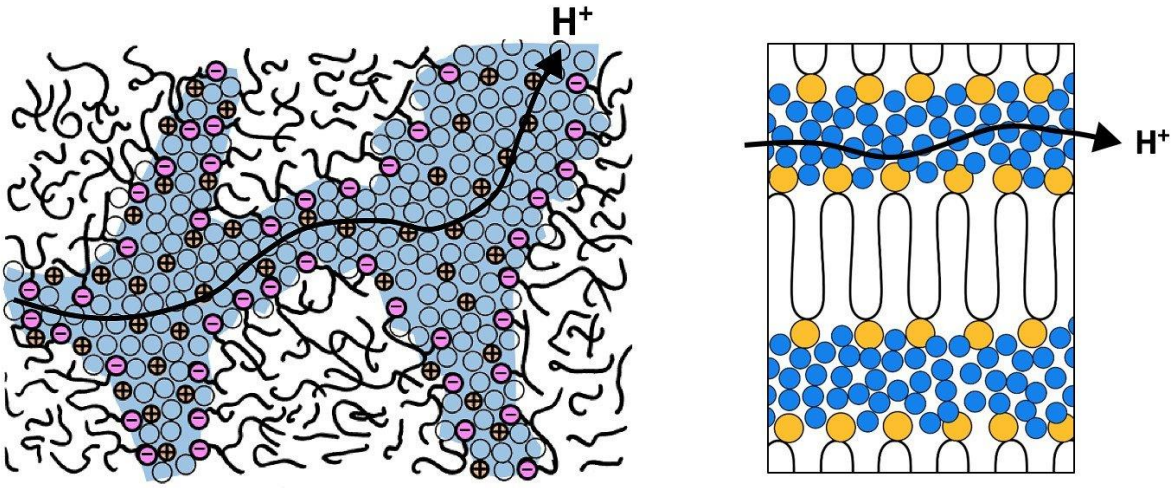

Figure 38 schematic representation of hydrophobic and hydrophilic clusters, with the hydrophilic side filled with water and allowing for proton conduction throughout the membrane

Protons cross the membrane following a Grotthuss or a Vehicular mechanism; the former proceeding via proton hopping from one water molecule to the next from a stationary oxygen atom to a neighbouring oxygen atom; the latter proceeding via proton attachment to a water molecule which is transported through the membrane via transitional diffusion.[65–67] The Vehicular mechanism occurs when water molecules move freely (i.e. when polyelectrolyte membranes are highly hydrated). The Grotthuss mechanism can also occur at lower humidity with water molecules bonded to acidic groups [68].

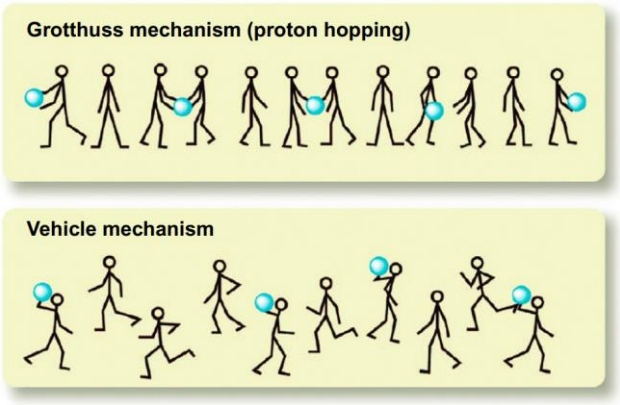

Figure 39 Simplified representation of the Grotthuss and Vehicular transport of protons. Reproduced with permission from Ref. [69].

PEM have mainly been produced through wet processes [70], bringing several drawbacks including swelling, shrinkage, agglomeration, and wastage whilst typically being costly and multistep. The development and application of innovative approaches to overcome these drawbacks are naturally of significant interest. A relevant approach is CVD, which uses gaseous precursors that are capable of reacting on various surfaces. CVD has the advantage to produce thin films which decrease the proton ohmic losses of the membrane[206], moreover the ability to provide conformal coating over rough surfaces can increase the intimate contact between the catalyst and the membrane which is essential to have a good triple phase boundary (TPB)[29].

In this chapter we are going to describe the setting up of a prototype CVD tool developed during the course of this PhD and the results associated with it regarding the synthesis of proton exchange membranes. Initially, the project was focusing on the synthesis of such materials using the PRODOS (see chapter II). The PRODOS is equipped with a vaporizer for liquids and a gas line undergoing plasma activation (see PRODOS description in chapter II). The idea was to copolymerize a liquid perfluoro-sulfonylethoxy propylene vinyl ether (PSEPVE) (Figure 40) which is the ionic bearing group of nafion® and the gas mixture of CH_4 and CF_4 saw in the previous chapter. The activated gas mixture including

gaseous radicals would attack the π bond in the PSEPVE and incorporate the molecule in the perfluorinated matrix which would give us a nafion-like film.

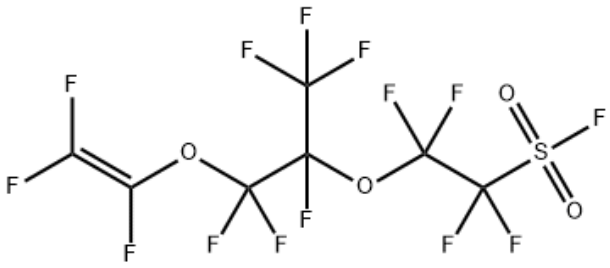

Figure 40 perfluoro-sulfonylethoxy propylene vinyl ether also abbreviated PSEPVE is the ion bearing group molecule of nafion®

Quickly we realised that the incorporation of the PSEPVE in the matrix was not successful which led us to think that the pathway between the plasma activation area and the deposition chamber is too long (approximately 50 cm) and has a high chance of inactivating the active species prior to reaching the substrate surface, preventing the copolymerization from taking place. When we use the mean free path formula:

$$\lambda = \frac{k_b T}{\sqrt{2}\pi d^2 P}$$

Where $k_b$is the Boltzmann constant, T the temperature, P the pressure and d the molecule/atom diameter. Considering a pressure of 0.2 mbar and a temperature of 200°C for Ar, which are typical experimental conditions for the PRODOS, we obtain a mean free path of 1 cm. With this we can estimate that an activated specie coming from the plasma source has very low chances to reach the substrate without undergoing a single collision. Moreover, the path from the plasma source to the chamber is not a line of sight and the gas stream encounter many surfaces, which further increase the risk of inactivation due to collisions with walls.

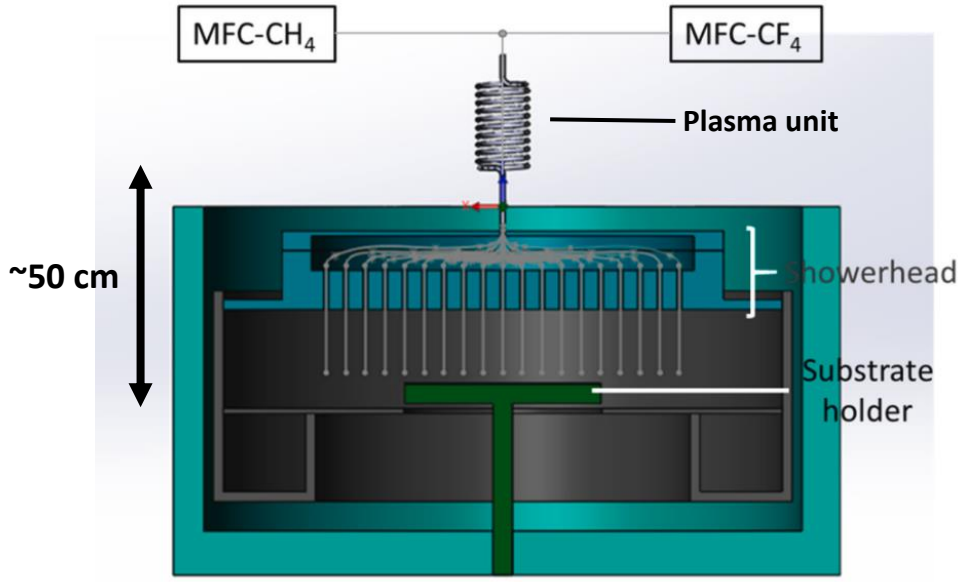

Figure 41 Schematic representation of the PRODOS path from the plasma unit to the deposition chamber highlighting the long tedious pathway

In order to overcome these limitations and the inability of the PRODOS to copolymerize the dually injected species, a prototype was set up based on the PRODOS itself. In this chapter we will describe the evolution of the setting up of the prototype to replace the PRODOS for the synthesis of proton exchange membranes. Various versions were set up in an evolutive way based on the results obtained with one version and the other. The objective pursued to assess the relevance of a prototype version is the copolymerization of perfluoro(3-oxapent -4-ene) sulfonyl fluoride (also abbreviated PSVE) and hexafluoro-1,3- butadiene (HFBD) (Figure 42). PSVE is the ionic bearing group of Aquivion™ membranes which is a proton exchange membrane with improved proton conduction properties compared to Nafion™ commercialized by Solvay. HFBD is used as the carbon backbone, with its two double bonds, it can covalently bond and reticulate the polymer produced to improve its mechanical properties. Since Aquivion™(and Nafion™) rely on the crystallization of PTFE backbone chains for the mechanical properties, replacing the TFE monomer with HFBD, the covalent bonding of the chains between themselves would allow for the riddance of hydrophobic crystals clusters responsible for the mechanical properties of the membrane.

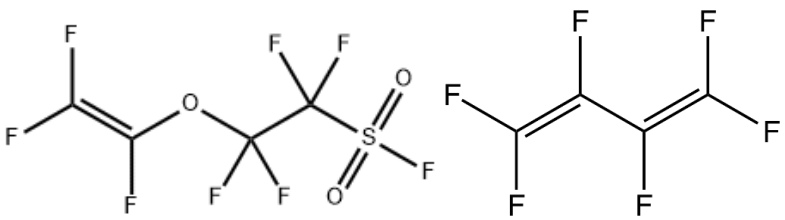

Figure 42 Chemical structure of perfluoro(3-oxapent -4-ene) sulfonyl fluoride (also abbreviated PSVE) and hexafluoro-1,3-butadiene (HFBD).

2 MATERIAL AND METHOD

2.1 SUBSTRATES

The substrates used in this chapter were silicon wafers of 50 mm in diameter of undoped prime grade. The thickness is 280 µm and the resistivity >100 Ohm-cm.

2.2 OPTICAL EMISSION SPECTROSCOPY (OES)

An optical emission spectrometer is a tool designed to study the elemental composition of a sample based on its light emission. In the case of glow discharges, electrons are accelerated and collide with molecules/atoms releasing more electrons in the cloud. A significant portion of these atoms will become ionized and when an atom or a molecule is excited within a plasma, its electrons move from a lower to higher energy level. Upon relaxation to their initial ground state, energy is emitted in the form of photons giving a characteristic emission spectrum for their respective elements/species. Optical emission spectra were recorded in the 200–900 nm wavelength range thanks to an ARC SpectraPro-2500i spectrometer, equipped with a CCD detector and a grating of 300 lines/mm and blazed at 300 nm. One hundred acquisitions of one hundred ms were recorded for each process. The OES was connected to the deposition chamber on the left side on the level of the substrate to record the emission spectra of the species generated in the upstream plasma unit.

2.3 X-RAY PHOTELECTRON SPECTROSCOPY (XPS)

X-ray photoelectron spectroscopy is a surface elemental analysis probing the chemical composition of a material from a qualitative and quantitative point of view. The depth of analysis is shallow in the order of 10 nanometers[182] which allows for a sensitive analysis of the surface chemistry. The sensitivity of the technique is in the order of atomic percentage. XPS analyses were carried out with an Axis Ultra DLD Spectrometer (Kratos Analytical Ltd., UK) equipped with a monochromatic Al Kα X-ray source (hν = 1486.6 eV). The analysis area was 300 × 700 µm^2. The acquisition of high-resolution

spectra was done with a pass energy of 40 eV while the survey spectra were acquired at a pass energy of 160 eV. High resolution XPS was performed for C1s, S2p and N1s. The spectra were treated with CasaXPS software.

2.4 TIME OF FLIGHT-SECONDARY ION MASS SPECTROMETRY (TOF-SIMS)

ToF-SIMS is a surface sensitive analysis method that uses an ion beam to volatilise the molecules from the outermost surface while ionizing them (SIMS). The molecules are then accelerated into a flight tube and their mass is determined by the time the molecules take to hit the detector (ToF).

3 PROTOTYPE DESIGN, RESULTS AND DISCUSSIONS

3.1 FIRST VERSION

In order to cope with the PRODOS limitations a smaller version of it was set up. Initially the working principle of the so called PRODOS junior was the same as the bigger version of it and the first version had the same working principle.

3.1.1 Set up of the 1st version of the prototype

The 1st version of the prototype was set up as follow (Figure 43). The gas panel included three injection line connected to argon, oxygen and HFBD (Gas in the scheme) sources. Every gas injection line was controlled by a mas flow controller which allowed for gases to mix in designated proportions. The mix of gases was injected in the Plasma chamber (3000 W, 1.9–3.2 MHz, Model Litmas RPS 3001 from Advanced Energy). The plasma unit is an inductive coil type of plasma with a range of power input going from 100 to 3000 W.

The liquid panel is equipped with an atomizer for the liquid PSVE and a Controlled Evaporation Mixing (CEM). The liquid PSVE cannister is put under pressure with argon, pushing the liquid through a Liquid Flow Monitor (LFM) to a mixing valve. In parallel, argon is injected in the CEM through the mixing valve via a Mass Flow Controller (MFC). The mixing valve allows for the regulation of the injection rate of

the liquid in the CEM and the argon is used for the atomization of liquid droplets in the CEM. The mixing valve is controlled via the Bronckhorst® software which regulates the injection flow of the PSVE. The CEM unit is basically a heated tube that can increase temperature up to 200°C to evaporate the liquid. The gaseous PSVE reaches the deposition chamber after the plasma unit. Argon is directly connected to the deposition chamber allow for the purging of the chamber. The deposition chamber is set under vacuum by a pumping system that can be bypassed to go through a cold trap for the trapping of toxic species.

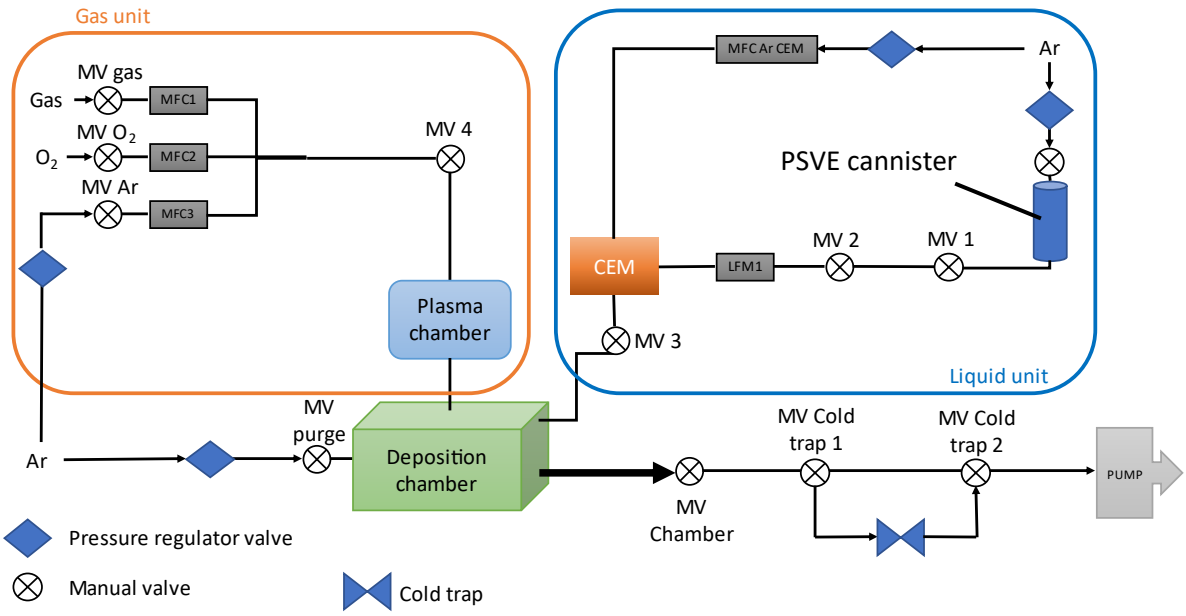

Figure 43 Schematic representation of the prototype (back then called PRODOS junior)

Here below is a picture showing the deposition chamber located underneath the plasma unit and the prototyping model sketched by the prototyping team in LIST (Figure 44). In those depictions, we can see the plasma unit located above the deposition chamber. The deposition chamber is equipped with a pressure gauge and the pumping line. Both the plasma injection line and the liquid injection are located on the above of the deposition chamber. From the bottom, a tube holding the substrate holder that can slide up and down to adjust the distance of the substrate from the plasma chamber, the same tube is connected to a chiller which is a component that we use to control the substrate holder temperature during depositions.

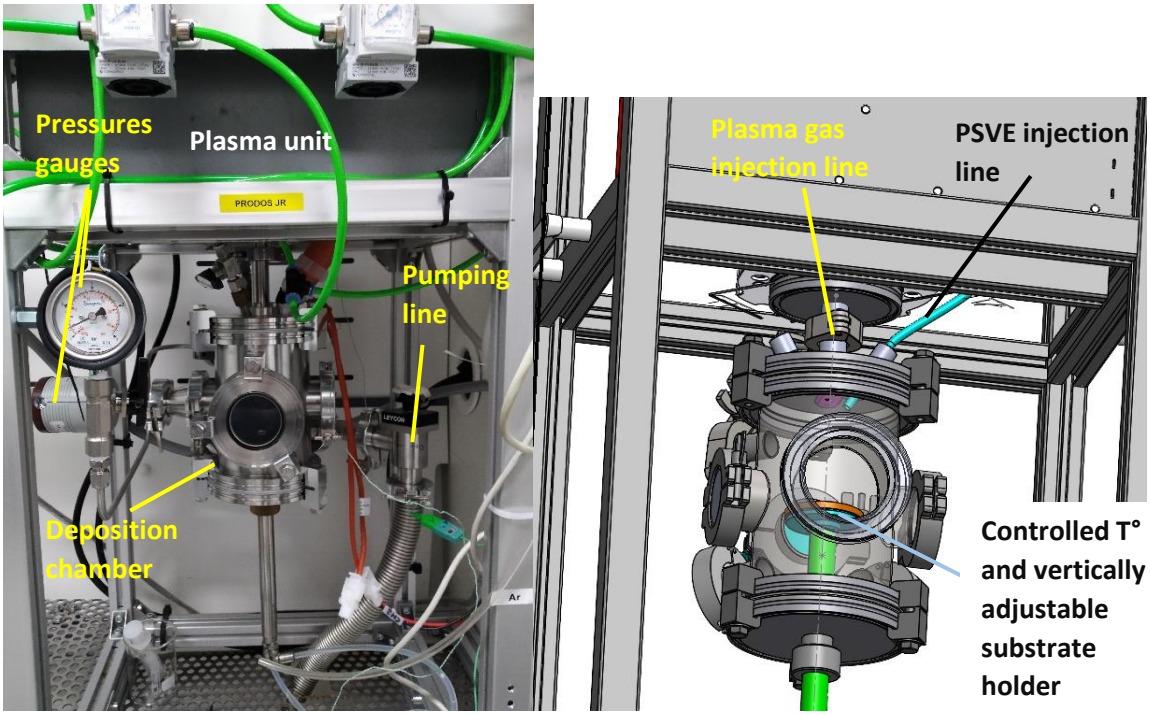

Figure 44 Picture and prototype scheme model for the 1st version of the deposition chamber of the PRODOS junior.

With this we can control several parameters during the deposition processes. HFBD injection flow, argon flow (for dilution), PSVE injection flow, the temperature of the substrate, the distance of the substrate to the plasma chamber and deposition time. The pressure is not adjustable, nor is the temperature of the deposition chamber.

3.1.2 Results associated with 1st version

The tests that we carried out with this version were solely based on the deposition of HFBD. The reason for this decision was that the HFBD undergoes plasma activation and must be able to deposit by itself before the second monomer can be incorporated. But unfortunately, we could not observe any deposition. A silicon wafer substrate covered in fluorinated polymer should go from hydrophilic to hydrophobic surfaces, hence a quick test that we can do when we take out the silicon wafer out of the deposition chamber is to drop a water droplet and see whether it sits round or flat on the surface. Now with this first version of the prototype little to no deposition was ever observed which led us to think that active species could not exit the plasma chamber and were depositing on the plasma chamber walls instead which is why we connected an Optical Emission Spectrometer (OES) to the chamber in the stead of the pressure gauge to analyse the light emission of gases in the deposition

chamber. Since the gas undergoing the plasma activation is HFBD and argon we would expect to see emission spectra's typical of CF, CF_2, CF_3 and argon. Fluorinated carbonaceous species usually have a typical signature ranging from 200 to 350 nm in the emission wavelength spectrum[207] while argon typically show light emission ranging from 700 to 900 nm[208]. Figure 45 shows the emission spectra obtained in our deposition processes for a mix of argon and HFBD at various plasma power, with one benchmark of solely argo. What we see is that typical emission wavelengths for argon are observed but no typical signature of CF_x are detected. This led us to confirm our allegation suggesting that the HFBD is decomposed in the plasma chamber and deposited there which prevents the deposition on the silicon substrate further downstream. Some peaks between 400 and 500 nm can be distinguished and are usually considered to be carbon contamination emission lines[209].

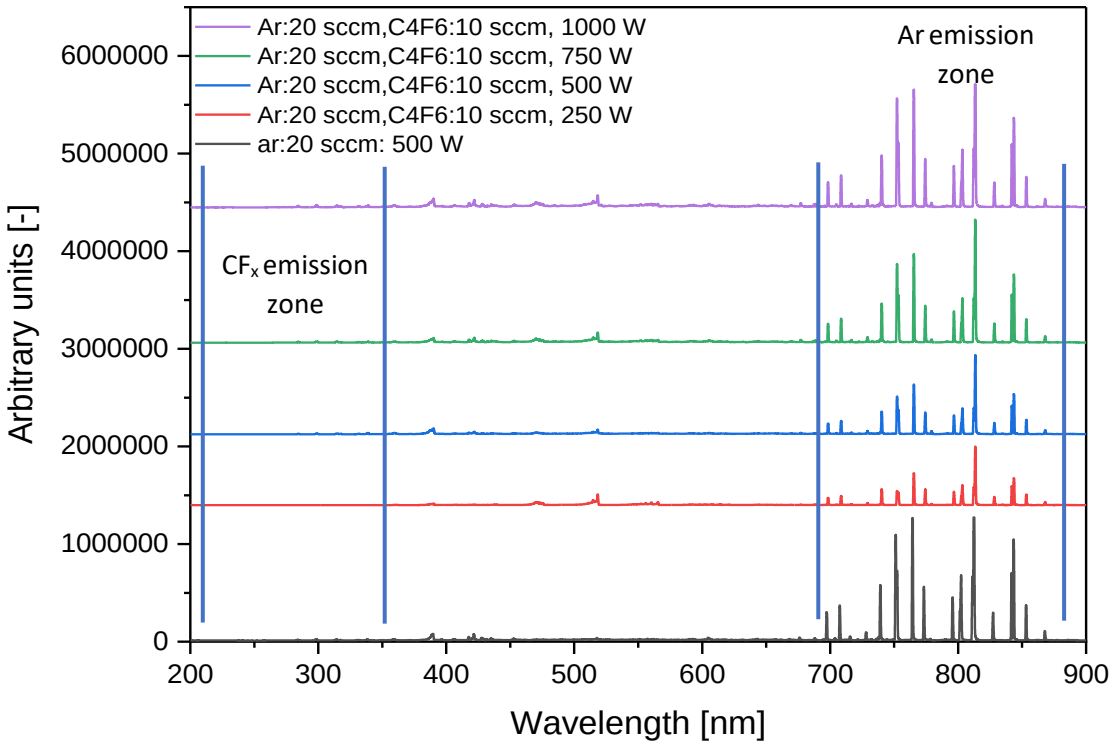

Figure 45 OES of a mix of argon and HFBD with varying plasma input power

3.2 SECOND VERSION

3.2.1 Set up of the 2nd version of the prototype

After the failure to obtain any kind of deposition in the first version, a drastic change of technicality was brought to the prototype. A set up based on Lucovsky et al. work was assembled[153,154]. For a starter, the HFBD no longer goes through the plasma, but only non-polymerizable gases such as argon, oxygen or nitrogen. The injection of PSVE no longer rely on Bronkhorst technology as we only had issues with it. In the injection tests of PSVE, we could not establish an injection rate setpoint, but only having an open or a closed mixing valve. Furthermore, sometimes the mixing valve would not open without us knowing why. We could not rely on this technology, so we sent it back to Brockhorst manufactory for repair but in the meantime, we built a new liquid injection system. The new system is a simple bubbler, with an argon pipe plunging in the liquid and an exit line open on the deposition chamber under vacuum. As a matter of fact, PSVE has a high vapour pressure, which is around 12kPa at 20°C "https://echa.europa.eu/registration-dossier/-/registered-dossier/20762/4/7" (as a comparison, ethanol vapour pressure is 5.95 kPa at 20°C). We decided then to use the bubbler as a simple evaporator, so we don't have to inject more argon in the deposition chamber which tends to increase the total pressure in the chamber.

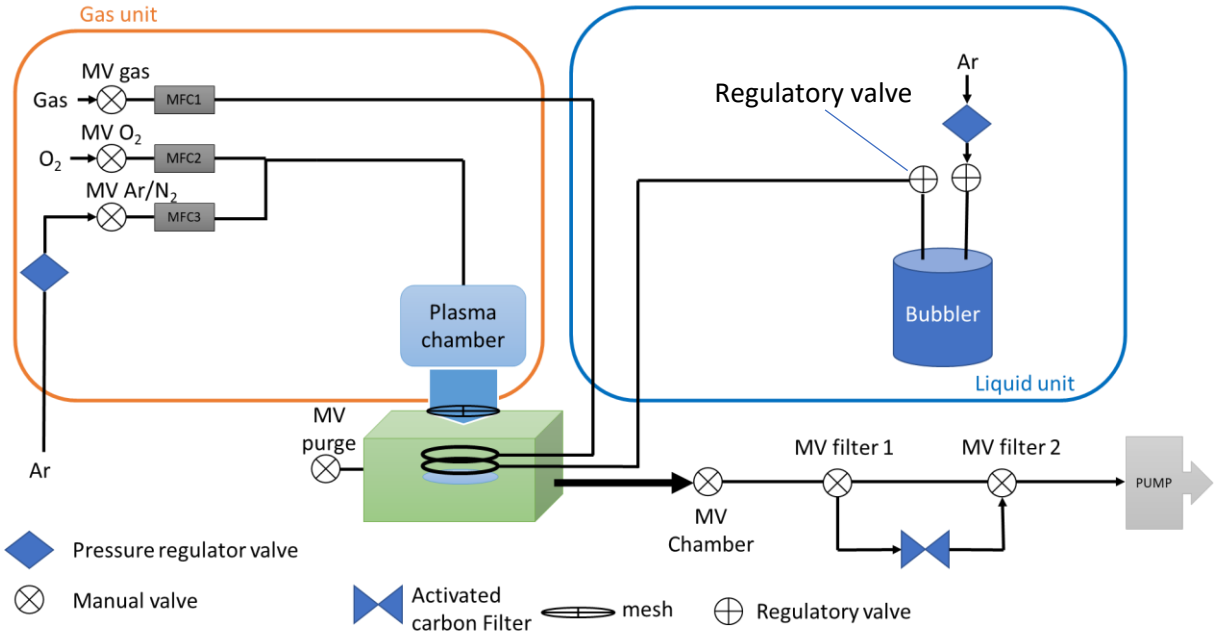

Figure 46 Scheme of the second version of the prototype working principle.

The injection of both the HFBD and the PSVE was changed to occur close to the substrate surface. Two O ring (one ring for the HFBD and one for the PSVE) are stacked together and pierced inward to inject both precursors above the substrate. Reactive gases coming from the plasma chamber are injected from above and come in contact with the precursors right above the substrate surface. The tube connecting the plasma chamber to the deposition chamber was also widened to consider the geometry factor stating that decreasing the diameter of the injection will reduce drastically the number of active species downstream from the plasma zone[166].

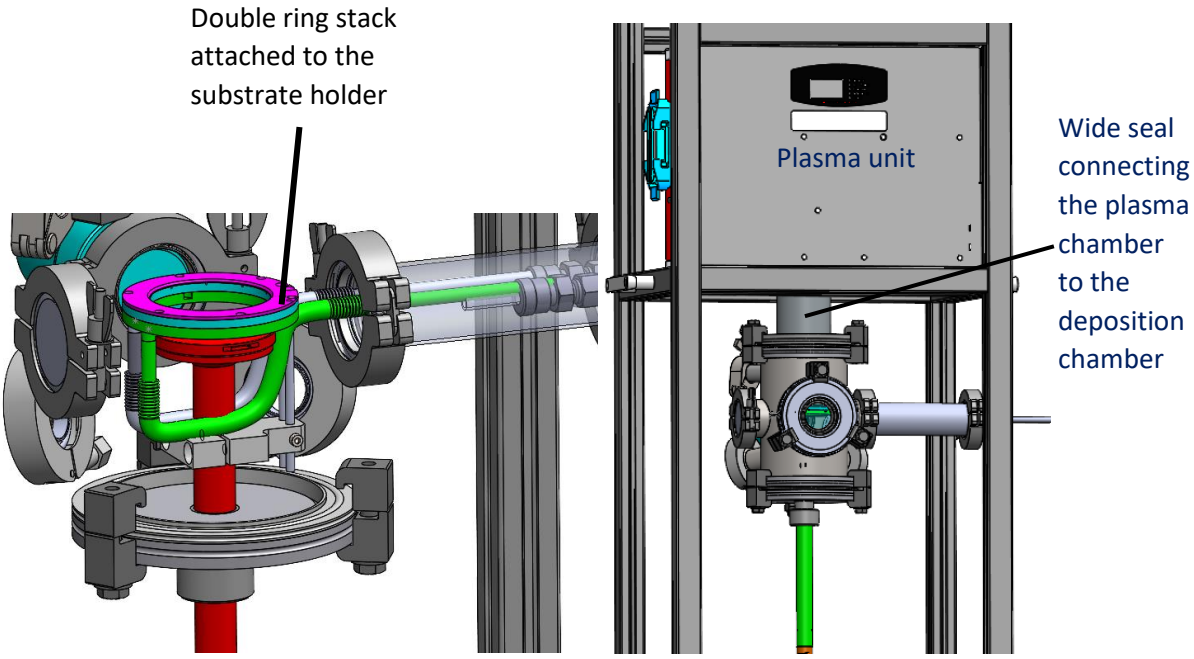

Figure 47 Picture and prototype scheme model for the 2nd version of the deposition chamber of the PRODOS junior.

3.2.2 Results associated with 2nd version

In this context, the dual injection of HFBD and PSVE was investigated. The first results were encouraging and showed deposition on the substrate surface. The main characterization technique that we used was XPS to obtain an insight in the chemistry of the deposited polymer. Figure 48 shows the elemental analysis and reveals the occurrence of sulphur, fluorine, oxygen and carbon in the film. Sulphur is the signature element that we want to see in the film as it is the proof that the PSVE is well incorporated in the film. Oxygen is only present in PSVE as parent molecule but can also be detected from the substrate (silicon wafer) and from a potential atmospheric leak in the reactor. In term of

atomic percentage, the carbon and fluorine have the highest ratio as can be expected from the precursor molecules. Sulphur occurs in an interesting 2.86% ratio which is higher than Nafion™ (≈1-2%[210,211]) and Aquivion (≈1%;in house measurements). The higher the concentration of ionic groups, the better the proton conductivity[212], hence the interest in this atomic ratio. O1s is twice as high as the sulphur content which could be expected when we look at the ending group of PSVE -SO_2F which shows two oxygen atom per sulphur atom.

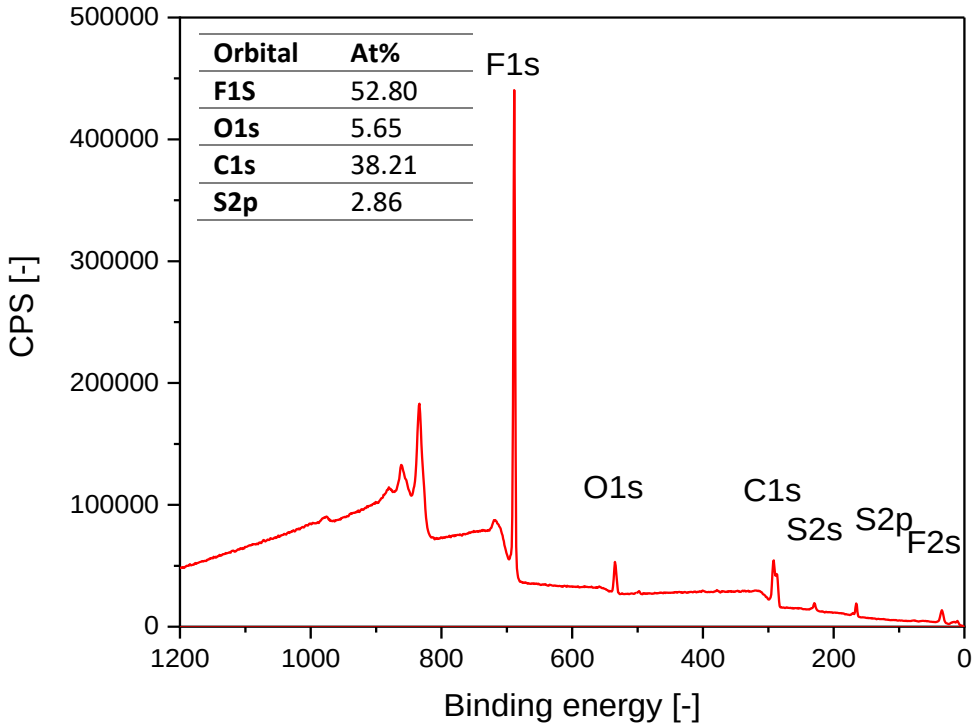

Figure 48 Elemental analysis of the first sample deposited from HFBD and PSVE with the second version of the prototype

High resolution XPS spectra were obtained for the same sample for orbital C1s and S2p (Figure 49). C1s shows us the oxidation state of the carbon atoms in the polymer matrix. The fluorinated carbon chains are interconnected via CF and C-CF_x (290 and 287.5 eV) units while CF_2 (292 eV) provides a linear portion of the chain. The CF_3 units (294 eV) are token of the end of chains as they can only be bonded to one carbon atom at a time. Some aliphatic groups were also detected and are most likely due to atmospheric contamination.

High resolution S2p spectra were very interesting as they showed us that most of the sulphur was on the wrong oxidation state. -SO_2F is supposed to have an oxidation state equivalent to 171 (for spin orbit 1/2) and 172 (for spin orbit 3/2) but most of it was found in the 165-167 eV region which is

considered to be -SH group with CF_x neighbouring groups. With this we can expect the PSVE to be degraded due to the plasma process and most of the sulphur finds itself incorporated in the film in the wrong conformation. Based on these first results, the next depositions we tried were with the scope to increase the -SO_2F peak with regard to the total amount of sulphur in the film.

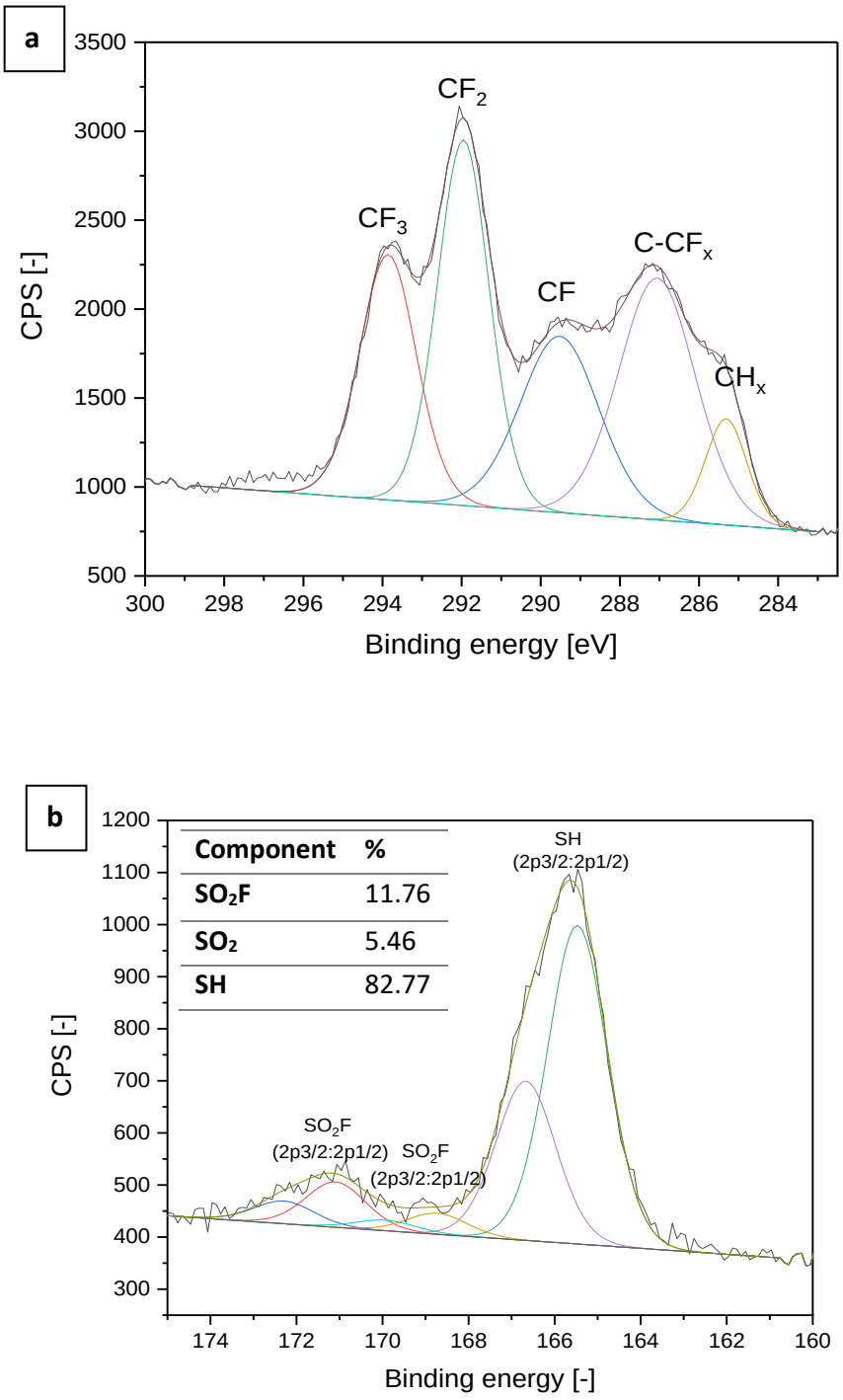

Figure 49 High resolution spectra for C1s and S2p the first sample deposited from HFBD and PSVE with the second version of the prototype

Nevertheless, we could observe the occurrence of -SO_2F in the film and we decided to cross check with TOF-SIMS technique to see whether the whole PSVE molecule was present in the film of just the ending group. Figure 50 shows the m/z spectra of the obtained fragments of the films. At m/z= 83 we can see the occurrence of -SO_2F unit occurring and at m/z=199 the fragment corresponding to PSVE with a bond breakage between the oxygen and the CF between the dangling bond and the backbone chain. With this we can estimate that when we incorporate the PSVE in the polymer matrix, some of the sulphur remains in the form that we wanted with a radical chain polymerization on the double bond.

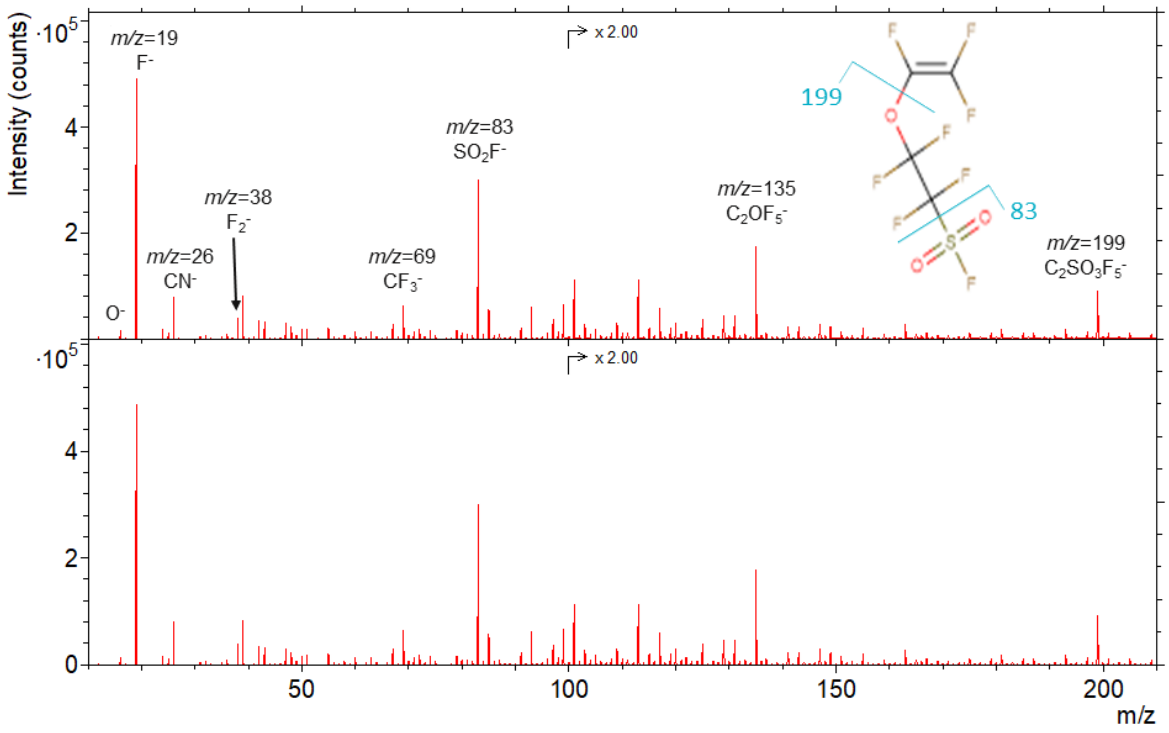

Figure 50 TOF-SIMS performed on the first sample of the 2nd version of the prototype

From these results, the objective that we pursued was to increase the quantity of -SO_2F (from XPS data's) with regard to the total amount of sulphur in the film. In order to do this, we had several process parameters we could play on. The flow rate of argon as diluent, the substrate temperature, the distance to the plasma unit and the plasma power. The injection flow of HFBD and PSVE remained constant at the maximum allowed by the components, respectively 10 sccm for HFBD and the manual valve of PSVE was kept at an opening of 10%. The duration was maintained for all samples at 60

minutes while the pressure could not be regulated and was dependent on the total gas flow within the reactor. A tabular visualization of the samples produced, and their key process parameters is given. From the reference sample the first thing that we did was to increase the distance from the plasma zone to the substrate (9.5 cm to 11 cm) in order to try and decrease the alteration of the precursors in the films. The temperature of the substrate was lowered to 5°C to increase the adsorption of precursors on the substrate and various plasma power were used.

Table 14 Tabular description of samples produced with their respective process parameters

sample	Subs. Temp (°C)	Ar (sccm)	Plasma power (W)	Press. (mbar)	dist (cm)
ref	10	20	150	1	9.5
1	5	20	150	1	11
2	5	20	200	1	11
3	5	20	250	1	11
4	5	40	150	1.4	11
5	5	20	150	1	9.5
6	5	15	150	0.8	9.5
7	5	20	300	0.9	9.5
8	5	15	200	0.7	9.5
9	5	15	250	0.7	9.5
10	20	15	150	0.8	9.5
11	5	15	150	0.8	8

Table 15 shows the results associated with every sample produced and characterized by XPS with high resolution S2p deconvolution. We realise that at a distance of 11 cm, the silicon wafers show on the analysis, which we can assume is due to the fact that the films deposited are either too thin or are non-continuous. Unfortunately the Si2s peak has a plasmon associated with which peaks around 170 eV of binding energy[213] which overlaps the position of the S2p orbital for -$\underline{S}O_2F$. With this, when the silicon wafer shows on the analysis, we cannot deconvolute the peaks for S2p and provide a ratio. Due to this plasmonic effect and the very thin deposition obtained we decided to decrease the distance from the substrate to the plasma zone back to 9.5 cm. The distance to the plasma plays a role in the

deposition rate of the film and setting a longer distance decrease the film formation rate. Sample 4 is the sample where the silicon wafer is the most prevalent, which led us to consider decreasing the flow of argon for future samples.

For sample 5 to 10, varying the substrate temperature and the plasma power brought little to no improvement to the deposition when considering the atomic percentage of sulphur in the film and the atomic percentage of -SO_2F group. In sample 11, we observed a little improvement when we decrease the distance to the plasma to 8 cm with regard of the absolute quantity of -SO_2F. This led us to think that the closer the substrate to the plasma the higher the incorporation rate of the native PSVE precursor in the film.

Table 15 Tabular description of XPS characterization for all samples from the second prototype version with the atomic percentage and the various contribution to the S2p peak

Sample	C1S	Cu 3p	F1s	N1s	O1s	S2p	Si2p	S2p deconvolution		
								SH	SO2	SO2F
Ref	38.2	0	52.8	0.5	5.6	2.9	0	83	5	12
1	41.9	0	40.6	0	8.9	2.5	6.1	No data		
2	39.6	0	46.0	0	7.3	1.5	5.6			
3	38.9	0	50.7	0	6.3	1.8	2.3			
4	35.1	0	38.2	0	11.2	0.7	14.8			
5	36.5	0	53.8	0.4	6.7	2	0.5	70	17	13
6	35.9	0	55.7	0	5.4	2.3	0.2	79	11	10
7	38.1	0	53.7	0.5	5.5	2	0.5	86	3	11
8	36.8	1.1	52.4	1	6.6	2.1	0	85	3	12
9	37.4	0.5	54.6	0.5	5.3	2.2	0	89	1	10
10	36.6	0.8	56	0.5	4.5	1.8	0	84	5	11
11	36.4	0	54.3	0.7	5.7	2.6	0	83	0	17

It is worth mentioning that the window of opportunity for the process parameters that we could allow to sustain an inductive plasma are highly dependent on the plasma unit. This specific plasma unit has very narrow possibilities for process parameters before setting itself in warning mode (inductive plasma cannot be sustained). On the one hand we would like to decrease the plasma power to avoid the total or partial destruction of the precursors and the film and on the other hand at low power the plasma cannot be maintained in a stable inductive mode. Moreover, the higher the argon ratio in the total flow of gas present in the chamber the more stable the plasma, but we saw that increasing the

argon flow too much drastically increase the destruction of the forming film. We also saw that the films were thicker and the PSVE conformation better retained when the substrate was closer to the plasma zone, but the closer the injection rings to the plasma zone, the harder it is to maintain stable inductive plasma conditions due to PSVE and HFBD flying in the plasma zone. It seems that we were limited by the plasma unit and the narrow set of parameters that it can be subjected to which led us to the inevitable conclusion that we needed to change the plasma unit. This will be the third and final version of the prototype presented in this thesis. Table 16 summarizes the issues we encountered with the inductive plasma source with regard to the film formation and we can see that everything we wanted to do to improve the film deposition was detrimental to the sustainability of an inductive glow discharge.

Table 16 Tabular description of the conditions to improve the film deposition and the sustainability of the inductive plasma associated with it

Actions	Plasma stability	Film formation
Decreasing plasma power		
Substrate closer to plasma		
Higher argon flow		
Higher flow of precursors		

3.3 THIRD VERSION

The results of the second version were encouraging but quickly reached some limitations. The results showed that the polymerization and the incorporation of PSVE in the polymer matrix was working. The PSVE, though, was highly deteriorated and most of the sulphur (the signature element of the molecule) is incorporated in the form of -SH- in the polymer backbone and only about 10% of it was incorporated in the parent form -SO_2F-. The purpose of this 3rd version is to be able to increase the ratio of -SO_2F in the film by lowering the plasma power which could not be attained with the 2nd version. From discussions with the plasma group in LIST, they had a spare microwave plasma source that we could borrow for the last month of the thesis. With their advice we could mount this new plasma unit with minor changes to the previous version. The microwave source borrowed can withstand low (0.01 mbar) and high pressure (atmospheric pressure plasma) while maintaining a homogeneous microwave plasma even with low power value which is what we were looking for after the limitations encountered in the second version of the prototype.

3.3.1 Set up of the 3rd version

The 3rd version saw the replacement of the inductive plasma source with a microwave plasma source. As this last modification took place during the last month of the thesis, no prototyping scheme is provided here. A microwave generator was connected to a microwave focuser via a coaxial tube. The focuser provoke the ignition of a glow discharge within a quartz tube. The first thing that we can notice is that the microwave generator is outside of the fumehood which clears the view for the quartz tube. Due to this configuration, we can observe the glow discharge on the contrary with the inductive plasma source. The after glow is also observable underneath the microwave focuser. It's important to point out that in the picture, the glow discharge is a nitrogen one and not argon unlike the inductive source. Argon plasma, as we can now see, has a non-visible afterglow and a glow discharge upstream of the plasma source. We decided to keep using nitrogen plasma because the afterglow is the proof that there are active species downstream from the plasma generator. Argon plasma on the other hand was so high upstream that the glow discharge was located in the plastic connections, which could be a hazard due to the heating of the ion bombardment.

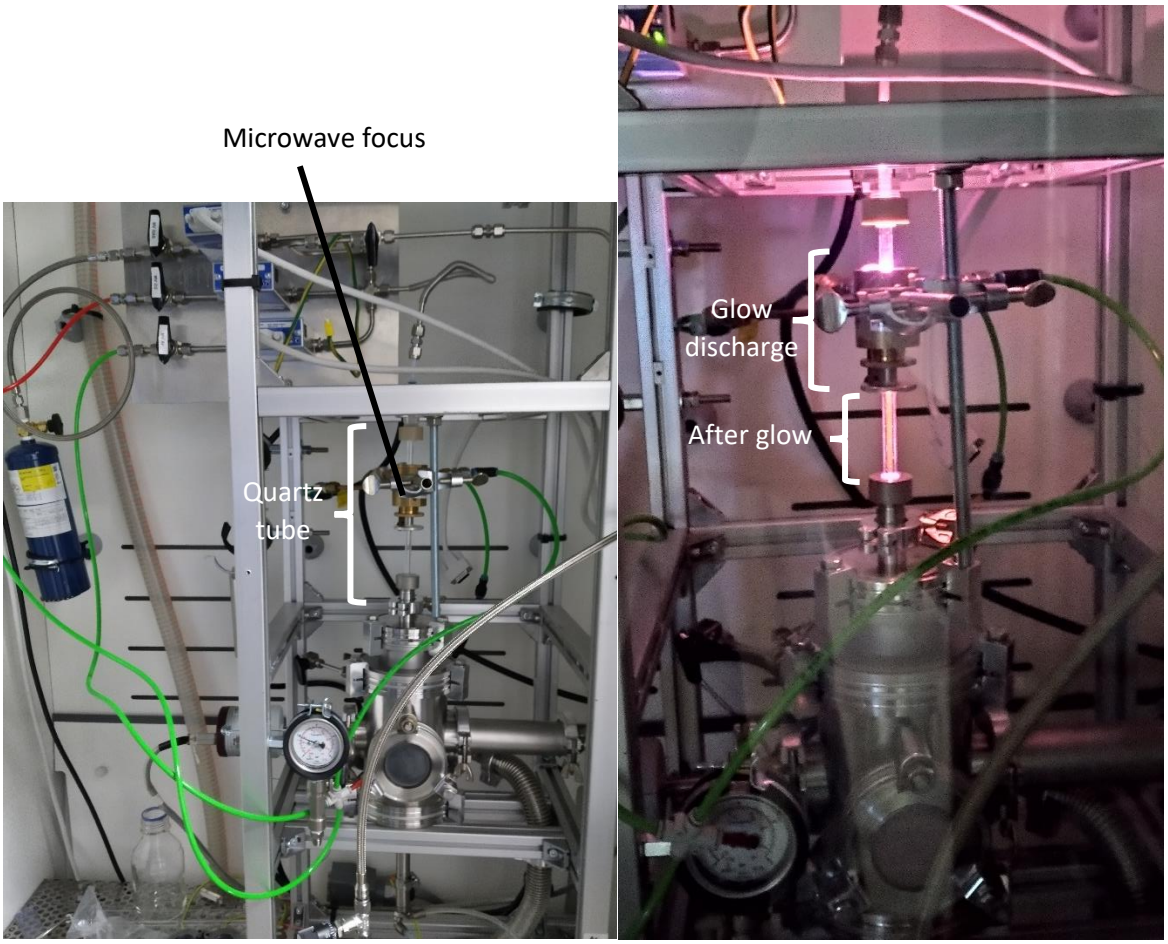

Figure 51 Third version of the prototype with a microwave plasma source where the glow discharge and the afterglow are visible

3.3.2 Results associated with the 3rd version

As stated above the deposition were done with nitrogen remote plasma activation unlike the 2nd version where we used argon plasma. The reason for that was the visual realisation that no after glow could be observed with argon while nitrogen had an orange afterglow that could be seen. Moreover, the first depositions carried out with argon activation produce no hydrophobicity while the one deposited with nitrogen were rendered hydrophobic (droplet on the surface test).

Ten samples were produced and characterized with XPS. Table 17 shows the process parameters used to produce the samples, the flow of HFBD and PSVE were kept constant at 10 sccm and 10% opening valve respectively, the deposition duration was also kept constant at 10 minutes. The pressure was not controllable and the was set by the feeding gas flow within the reactor. The first realisation is that

with the microwave plasma source we could sustain a glow discharge with much lower plasma power than it was possible with the inductive plasma source.

Table 17 Tabular description of samples produced with the process parameters used

Sample	Plasma power (W)	Nitrogen flow (sscm)	Substrate temp. (°C)	Pressure (mbar)
Ref	60	140	5	3
1	30	50	5	1.6
2	30	100	5	2.3
3	15	50	5	1.6
4	15	100	5	2.3
5	30	100	0	2.2
6	30	100	10	2.2
7	30	20	5	1

The reference sample was the first one produced with the parameters described in the above table. What we can see from Figure 52 is the expected large atomic percentage of carbon and fluorine. Nitrogen is also present in a large quantity which could be expected as nitrogen was used for polymerization activation. Oxygen occurs in an unexpected large quantity, which could be due to the presence of oxygen in PSVE but this large amount probably stems from contamination and from atmospheric leak in the reactor. The silicon substrate is barely visible (0.1%) which is a good thing considering the short deposition time (10 minutes) and therefore the large quantity of oxygen is not due to the silicon substrate.

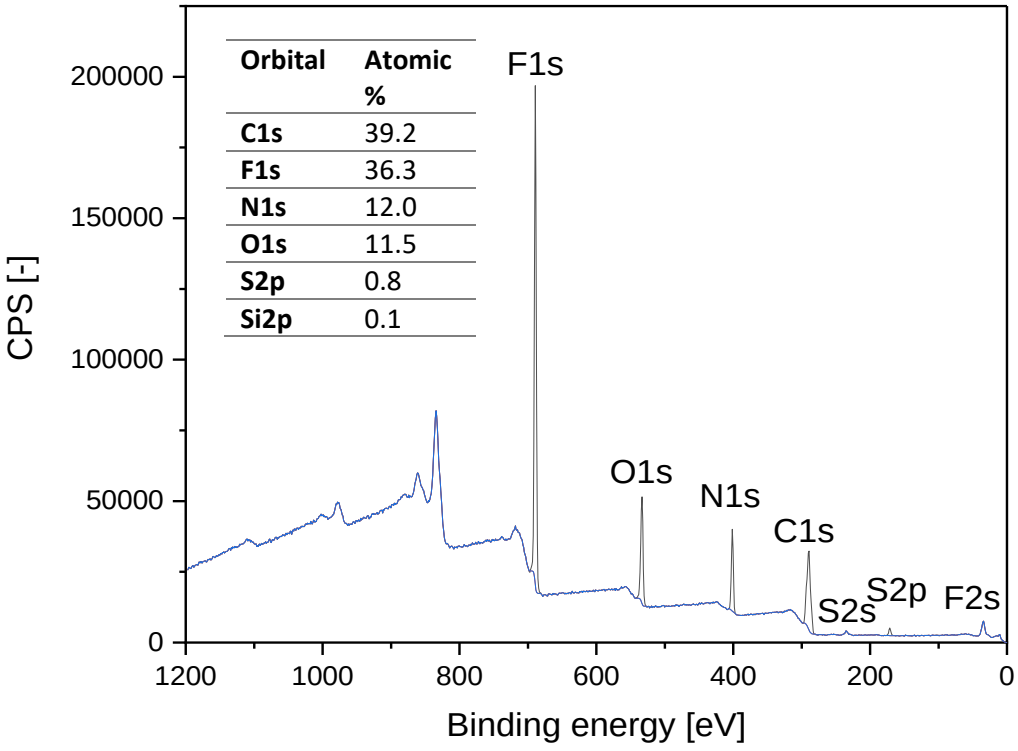

Figure 52 Survey spectrum for the reference sample with atomic percentage of each orbital

Figure 53 shows the high-resolution spectra for carbon, nitrogen and sulphur of the reference sample. The carbon 1s spectrum shows the fingerprint of several component. We can assertively state that the peak at 294 eV is the contribution of -CF_3, at 292 eV the contribution of -CF_2 and at 290 eV is -CF-[187]. The presence of oxygen and nitrogen in the film makes it complicated to assertively attribute the two peaks at 289 eV and 287.5 eV but one can assume that at 289 eV we have a contribution of -C-CF_x- and -O-C(O)- and for the peak at 287.5 eV a contribution due to ketone groups -C(O)- or -C-N-. The peak at 285 is typical of aliphatic groups -CH-/-C-C- which can be due to surface contamination when the sample was exposed to the atmosphere[214]. Due to precursors used (HFBD and PSVE) we can see that CF_2 and CF are present in the parent molecules and contribute to the C1s spectrum while CF_3 occurs due to the fragmentation of the molecules with incorporation of extra fluorine atoms in the film. The peaks at 289 eV and 287.5 eV are inherent to the process and are created due to the incorporation of contaminant atoms in the film.

The nitrogen spectrum sees one large contribution at 401.5 eV. This contribution is usually associated with -C-NH_2 type of contribution[215]. Due to the width of the peak the carbon to which nitrogen is attached to can be in various oxidation states.

The S2p deconvolution gives several contributions to the peak. The first observation concerns the peak of -SH which is much smaller than with the previous version of the prototype (see Figure 49b for reference). The contribution of -SO_2F is the dominant one in this reference sample compared to the previous version of the prototype which is a huge accomplishment since it was the main motivation for this third upgrade of the prototype. Even more interesting is the occurrence of a -SO_3 contribution, the oxygen must be added due to the oxygen contamination of the deposition. This gives an interesting perspective for the development of proton exchange membranes as the -SO_2F must be converted to -SO_3H to be active. Usually, this step involves a post treatment of the membrane with a Brönsted base (e.g. NaOH or KOH) to replace the fluorine in -SO_2F with an oxygen atom to give -SO_3^- Na^+ and a subsequent acidic treatment to wash off the sodium and replace it with an acidic hydrogen atom to give -SO_3H. The oxygen, which has been seen as a contaminant, actually gives rise to an interesting perspective to deposit a proton exchange film with the activation of -SO_2F in a one step process.

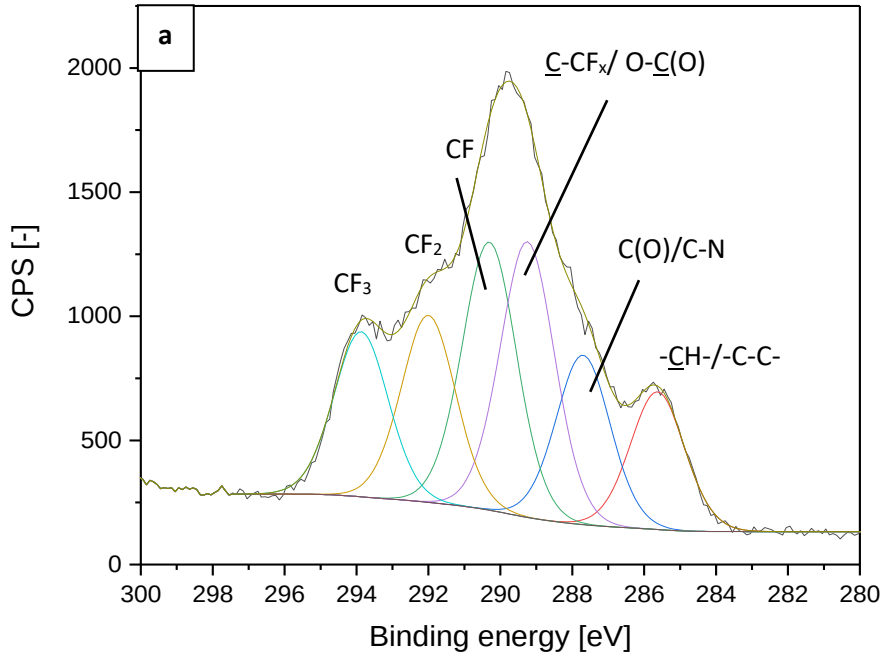

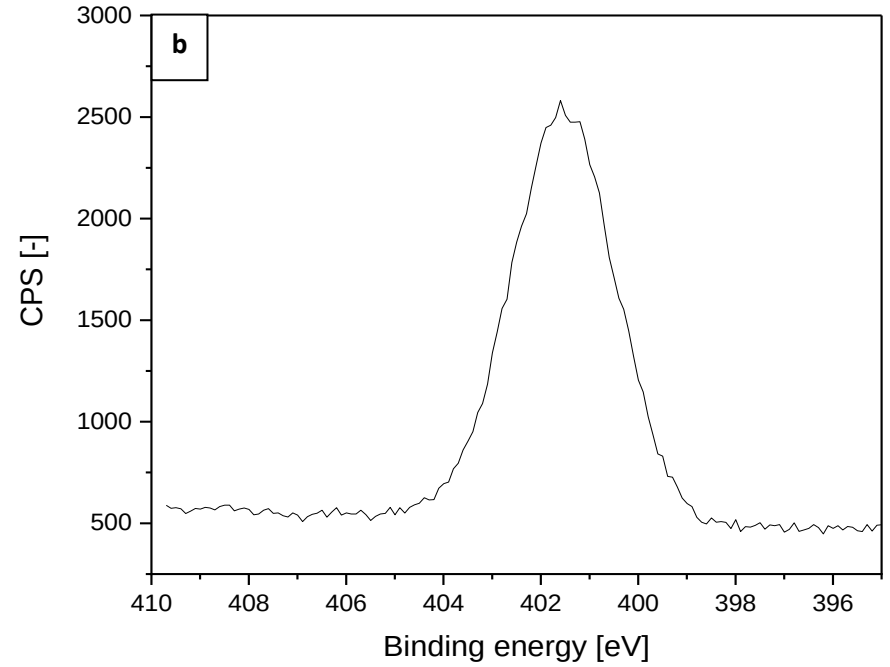

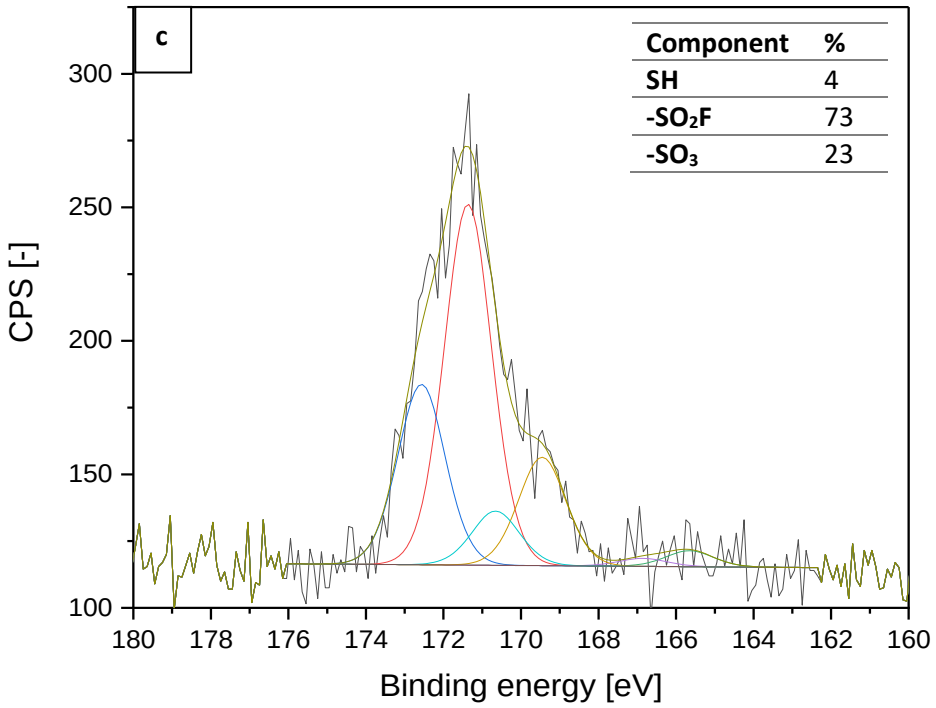

Figure 53 High resolutions spectra for the reference sample (a) C1s with deconvolution, (b) N1s, (c) S2p with deconvolution

Table 18 shows the comparison between the samples produced with this third prototype version. Samples 1, 3 and 7 have the highest content in silicon and as previously said, the plasmonic effect of silicon gives a peak at 170 eV which prevents the deconvolution of the S2p peak to single out the contribution of sulphur only. All those sample had a nitrogen flow below 100 sccm (50, 50 and 20 sccm respectively) which led us to think that a higher nitrogen increases the film deposition rate, sample 7 being the one with the lowest nitrogen flow and the highest percentage of silicon. On the other hand, these four samples also have a high sulphur content which could mean that the PSVE incorporate in the film at a higher rate, while this is a good thing, the low deposition rate is problematic and as seen previously, Nafion™ and Aquivion™ have a sulphur content of approximately 1%. These four samples also have the lowest content in carbon and fluorine which shows further that the film is too thin due to the low deposition rate.

Nitrogen content is stable over the range of the samples, but we can see that the lowest contents are for samples where the substrate is visible which shows that the nitrogen only incorporate in the polymer film. The oxygen content on the other hand increases for sample where the substrate is visible as silicon wafers contain oxygen.

The S2p deconvolution content is quite interesting as it varies a lot. For a starter, the content in -SH groups remain stable and low which is interesting as this is a chemical function that testifies of the degradation of PSVE precursor. The balance here occurs between $-SO_2F$ and $-SO_3$ groups. The highest content in $-SO_3$ occurs for sample 4 where the plasma power is the lowest (15 W) which led us to think that the lower the power the higher the $-SO_2F$ content is replaced by $-SO_3$. At plasma power of 30 W, the content of $-SO_2F$ increases. When we changed the substrate temperature from 0 to 10°C (sample 2 at 5°C, sample 5 at 0°C and sample 6 at 10°C) with a plasma power of 30 W and a nitrogen flow rate of 100 sccm, we see that the optimal point for the substitution of $-SO_2F$ with $-SO_3$ is at 5°C, this could be a good temperature for the substitution but with only 3 temperatures we cannot assume that as a general rule. These three films are very similar in terms of atomic percentage and further analysis should be carried to investigate the temperature substrate temperature influence on the film deposition such as the deposition rate for example, we unfortunately don't have such data's.

Table 18 Tabular description of XPS characterization for all samples from the third prototype version with the atomic percentage and the various contribution to the S2p peak (with total atomic percentage in the film)

Sample	C1s	F1s	N1s	O1s	S2p	Si2p	S2p deconvolution		
							SH (tot. %)	SO_2F (tot. %)	SO_3 (tot. %)
ref	39.2	36.3	12.0	11.5	0.8	0.1	4 (0.03)	73 (0.58)	23 (0.18)
1	38.4	30.0	12.9	14.6	1.6	2.5	No data		
2	38.6	31.6	13.6	15.0	1.0	0.1	6 (0.06)	54 (0.54)	39 (0.39)
3	34.7	28.7	10.2	15.3	2.9	8.2	No data		
4	36.6	34.1	11.9	15.3	1.6	0.4	3 (0.05)	48 (0.77)	49 (0.78)
5	38.6	33.6	13.0	13.7	1.1	0.0	5 (0.06)	69 (0.76)	26 (0.29)
6	39.3	32.6	13.4	13.5	1.0	0.0	3 (0.03)	71 (0.71)	26 (0.26)
7	26.5	23.6	7.1	19.4	5.2	18.3	No data		

4 CONCLUSION

In this third chapter we focused on the synthesis of proton exchange membranes via remote plasma chemical vapour deposition. The initial scope of the present thesis was to use the PRODOS system to deposit such films, but this was not proven successful, and the equipment was used to produce elaborated gas diffusion layers as described in chapter ll. Nevertheless, the idea of producing proton exchange membrane via remote plasma deposition was not forgotten and a prototype was set up to overcome the limitations of the PRODOS system. Three distinct versions of the prototype were produced in an evolutive way to reach such a goal. The deposition of reference was the copolymerization of perfluoro(3-oxapent -4-ene) sulfonyl fluoride (also abbreviated PSVE) and hexafluoro-1,3- butadiene (HFBD). PSVE is a precursor of Aquivion™ which is a proton exchange membrane commercialized by Solvay® and is a short side chain (dangling bond) membrane conferring better proton conductivity compared to Nafion™ for example. HFBD was used as the polymer backbone from where the dangling bonds (PSVE) are attached. The choice for this precursor was based on its two double bonds which provides the possibility to ramify the polymer backbone chain. Ramifying the polymer chain can provide mechanical resistance without relying on the crystallization of linear backbone segments which in turn allows us to increase the quantity of dangling bond to

increase the proton conductivity. Aquivion™ and Nafion™ are dependent on this crystalline phase to be self-supported but a crosslinked membrane could also make it self-supported.

The copolymerization reaction results were used as the benchmark to upgrade the prototype. The first version was based on the PRODOS™ and was a smaller version of it, the injection of HFBD was going through the inductive plasma unit, the PSVE being injected in the deposition chamber after the plasma zone. The results were not concluding as when we were trying to deposit films of HFBD, no deposition was obtain based on water contact test (surface should be hydrophobic). Further tests were obtained with optical emission spectroscopy, and we expected to see the CF_x light emission pattern but only argon (diluent gas) could be seen. The conclusion was that no film could be deposited on the substrate and the deposition occurred in the plasma chamber. This led us to rethink completely the technique to use.

The second version was designed based on the first remote plasma technique used. Only non-polymerizable gas can flow through the plasma to prevent deposition in the plasma chamber so we diverted the injection of HFBD to a ring located right above the substrate surface. A double O ring stack was designed to inject HFBD in one ring and PSVE in the other one and right above the substrate surface. Argon, nitrogen, oxygen can be activated in the plasma and make reactions occur downstream by reacting with the injected species in the double O ring. This upgrade was necessary to obtain films and the first attempts were successful in obtaining depositions. Depositing HFBD and PSVE was done by activating argon in the plasma chamber. The depositions were characterized with XPS, the films were mainly made out of carbon and fluorine. Sulphur was detected in the film showing that the incorporation of PSVE was successful. High resolution sulphur spectra were acquired and showed that three contributions were making the peaks (-SH, -SO_2 and -SO_2F). The contribution from -SO2F is the key group that we want to increase the predominance since we want to retain the conformation of the PSVE. Several samples were deposited by varying process parameters such as substrate temperature, plasma power, argon flow and substrate distance to the plasma zone in order to increase the contribution of -SO_2F. We could conclude from these samples that increasing the flow of argon was not interesting as it was destroying the film formation. With regard to the quantity of -SO_2F, low to no improvement could be observed from varying these parameters. The distance to the plasma showed the most improvement when the substrate was closer to the plasma zone, but no difference could be concluded from varying the other parameters. Cross analysis with TOF-SIMS were made and the presence of the PSVE parent precursor was observed showing that the -SO_2F signature was due to the incorporation of PSVE with conformation retention. With this second version we experimented new limitations that stems from the plasma unit. The process parameters that we wanted to modify were always in contradiction with the inductive plasma stability. Decreasing plasma power to prevent

fragmentation of the precursors was problematic to the stability of the glow discharge. Moving the substrate closer to the plasma also injected the precursors closer to the plasma zone which would destabilise the glow discharge. Higher argon flow is good for plasma stability, but we observed that increasing it would impede the formation of the film. A higher flow of precursors could also increase the film deposition rate but increasing the quantity of precursors would also be problematic to the sustainability of the glow discharge. These limitations were extremely problematic to improve the quality of the films which led us to the conclusion that the plasma source should be changed.

The purpose of this 3rd and last version is to be able to increase the ratio of $-SO_2F$ in the film by lowering the plasma power which could not be attained with the previous plasma unit. From discussions with the plasma group in LIST, they had a spare microwave plasma source that we could borrow for the last month of the thesis. With their advice we could mount this new plasma unit with minor changes to the previous version. The microwave source borrowed can withstand low (0.01 mbar) and high pressure (atmospheric pressure plasma) while maintaining a homogeneous microwave glow discharge even with low power value which is what we were looking for after the limitations encountered in the second version of the prototype. With this version the activating gas was changed to nitrogen because the after glow was much more intense than with argon. The characterization of the films used, once again, XPS as the reference. The samples were synthesized with much lower power (15 W to 60 W) than with the inductive plasma source, thanks to the stability of the microwave glow discharge. The first results were excellent, the quantity of -SH in the film remained extremely low in all the samples and the quantity of $-SO_2F$ group was drastically increase. Even more surprising was the occurrence of $-SO_3$ unit in the film, we observed a high oxygen contamination in the film and some of the $-SO_2F$ groups were converted by substitution of fluorine with oxygen. As the proton exchange membranes must be activated by the conversion of sulfonyl fluoride to sulfonate groups, this discovery came out as an interesting finding worth investigating. Furthermore, we observed that the lower the plasma power (e.g. 15 W) the higher the $-SO_3$ content. The film studied showed that a nitrogen flow below 100 sccm would yield a thin film highlighting the low deposition rate at lower nitrogen flow rate. These few findings helped us to consider low plasma power with high nitrogen flow rate to be the best parameters for proton exchange membranes deposition from PSVE and HFBD. The good results obtained were considered to be due to the microwave plasma source and the possibility to use low plasma power. Nitrogen could also be responsible for the soft activation of the polymerization but further investigation should be carried out to affirm this allegation.

This chapter was mostly a description of the evolution of the prototype. The third version left us with extremely promising results and a lot of unanswered questions. Unfortunately, the PhD time came to an end which left us with a lot of perspective and prospects to investigate. The next steps that would

have been undertaken would have been to optimize the deposition as this last prototype version seemed satisfactory with the few results that we obtained from it.

5 PERSPECTIVES

The first thing to do would be to investigate where the oxygen incorporated in the film comes from. This oxygen contaminant turned out to be a major advantage on the deposition of proton exchange membranes, but full control of the oxygen injection would be a powerful asset to investigate. The etching of the quartz tube and the stripping of oxygen could be a cause of the oxygen presence.

Argon (and other noble gases) from the has the advantage to not alter the chemistry of the films formed unlike nitrogen which can incorporate in films. We tried to use argon as the activating gas, but the depositions were unsuccessful in the present configuration. Further tests could be carried out by lowering the microwave focuser height and put it closer to the deposition chamber so we can increase the plasma power and obtain an effective after glow discharge.

Hydrogen plasma activation could also be an interesting opportunity. As hydrogen cannot make chemical functionalities, the hydrogen atoms could possibly provoke the polymerization without adding new chemical functionalities in the film (unlike nitrogen).

The optimization of the film in terms of deposition rate (reach higher thicknesses in a short time), quantity of $-SO_3$ functionalities and the role of substrate temperature should be further investigated.

A fine control of the deposition chamber pressure could be an interesting asset to have. In order to reach that, a new pump with larger volume evacuation capability should be connected. The base pressure would remain the same, but the flow of gases would not play a role in the total pressure measured. Additionally, a device to regulate the pressure inside the chamber could be mounted (e.g. a automatic pressure regulation valve).

GENERAL CONCLUSION AND PERSPECTIVES

This concludes the four years of PhD spent in the Luxembourg Institute of Science and Technology (LIST) as an employee of the Material and Research Department (MRT) and with the affiliation as a PhD student at the University of Luxembourg.

The field in which the research took place is at the crossroad between the hydrogen circular economy and chemical vapour deposition. Hydrogen will play a significant role in the energy transition from fossil fuels to more renewable and more sustainable energy sources. As it can be produced from renewable energy sources, hydrogen will play a role of secondary energy source or energy storage mainly to smoothen the energy supply to match the energy demand. As of now, 95% of the total industrial hydrogen is industrially produced from non-renewable fossil fuel sources. Efforts on producing hydrogen in a green way is essential and several path ca be undertaken such as electrolysis, biomass gasification, photocatalysis, microorganisms' hydrogen synthesis or even hydrogen mining among other methods. Hydrogen is needed in the steelmaking industry, fertilizer production and also aims at taking a significant portion of transportation fuelling to replace fossil fuels (heavy transports and light transports). The danger of climate shift and the reliance on untrustworthy energy sources suppliers accelerated the decision making toward the green transition in the European Union and other parts of the world. Strategies to make this transition happen always include a significant portion of hydrogen production and hydrogen infrastructure building planning (e.g. Fit for 55 and REPowerEU). This shows that the landscape of countries will significantly change in the next years and that we will see more and more hydrogen infrastructures like hydrogen refuelling stations, pipelines and electrolysers.

Hydrogen can be converted to electricity with devices called fuel cells. Different types of fuel cells exist but, in this PhD, we focused on the proton exchange membrane fuel cell (PEMFC). This type of device is made out of a membrane electrode assembly (anode, proton exchange membrane and cathode) sandwiched between two gas diffusion layers. Each component is essential and can be improved with scientific research to improve the overall fuel cell efficiency and decrease the overall cost of fuel cell installations. In this PhD we focused on the proton exchange membrane which is a copolymer of carbon backbone with ionic bearing dangling groups and the gas diffusion layers. The aim was to improve the quality of these components by using chemical vapour deposition. CVDs are considered important future industrial tools that utilize gases instead of liquids to perform bottoms up chemistry. The CVD techniques are advantageous because they are dry processes, coat complex surfaces, use

gases to overcome immiscibility, produce high quality pure films among other advantages. Meeting the fuel cells requirements with CVD is sure to have an interesting impact on the roll out of hydrogen technologies. Many CVD techniques exist and can be classified accordingly with their activation methods and in this thesis, we used a remote plasma activation of the precursors. Using remote plasma is interesting to softly activate the polymerization of fragile precursors (e.g. organics) and to keep a plasma chamber free of contaminations.

In the second chapter we showed the results associated with the deposition of perfluorinated films in the PRODOS-200 PVPD™ R&D System from methane and tetrafluoromethane. The PRODOS system is a chemical vapour deposition that uses a remote plasma unit to deposit thin films on 8 inches in diameter substrate. A remote plasma system should be carefully considered as gas phase reactions takes place and the inactivation of species due to gas phase reaction and gas to wall reaction inactivate the active gaseous species. That's why we used a mix of an etching agent (CF_4) and a fast-depositing agent with a high sticking coefficient (CH_4). In a remote plasma, the mix of fluorinated gases and a gas with high deposition rate work against each other, producing surface and gas phase reaction preventing the deposition of a film in the plasma chamber and allowing for a longer life-time of a the generated species in the gas phase. In a remote plasma, several steps will take place from the plasma chamber to the remotely located substrate. Due to its etching properties, CF_4 will prevent the deposition of an amorphous carbon film (due to the presence of CH_4) while adding fluorinated atoms in the chemical structure of generated volatile species.[172]

The first part of the results includes the physico-chemical characterization of the deposited films that varied with regard to the deposition process parameters (substrate temperature, total feeding gas flow, flow ratio between CH_4 and CF_4). The second part studied the potential use of these films to enhance carbon fibres fabric and their use as gas diffusion layers for PEMFC.

The first part showed the results published in VACUUM (Elsevier)[216]. We studied the deposited films and characterized them with WCA, SEM, profilometry, topographic AFM, XPS, XRD. From these results we showed that the films had various water contact angle ranging from hydrophobic to ultrahydrophobic. Correlating these results with topographic AFM, we could see that the rougher the surface of the deposition the higher the hydrophobicity. Thicknesses were assessed via profilometry and correlated the temperature of the substrate with the thickness of the deposition (the lower the temperature, the thicker the deposition). SEM imaging revealed one very peculiar sample with *rose petals* morphologies at the surface, that sample also occurred to have the highest roughness, the thickest deposition and an ultrahydrophobic behaviour. XPS shows two categories of profiles depending on the feeding gas ratio of CF_4 and CH_4. At a ratio of 80% CF_4, the chemistry of the film is

made out of linear oligomeric chains with the formula $CF_3(CF_2)_nCF_3$, while when we have a ratio of 70% CF_4, the chemistry becomes more complex with reticulation of the polymer and the addition of aliphatic groups under the form of carbon black dust. XRD measurement showed us that the one sample showing the *rose petals* structures is crystalline while all the others were amorphous. This led us to think that when linear oligomeric chains are deposited at a specific temperature (20°C) with a sufficiently high enough total feeding gas flow, a nucleation process is taking place forming crystallites that in turns form grains that look like *rose petals*.

The GDL's are commonly made out of a support of diffusion which undergoes a hydrophobic treatment or the application of a microporous layer. Plasma treatments can be used when one desire conformally coat carbon fibres. The hydrophobization of carbon cloth fabrics with the present process was used to produce elaborated gas diffusion layers. A methodology was developed using techniques such as X-ray tomography, SEM, HIM-SIMS, atmospheric SEM, fuel cell test bench and conductive AFM to deeply understand the behaviour of the produce samples as GDL's. High resolution electron microscopy revealed that the *rose petals* structures observed when the film was deposited on silicon wafer also appear on the carbon fibres cloth. HIM-SIMS shows us also that the process coats the carbon fabric in a non-line of sight fashion wrapping the carbon threads even at the lowest point in the deposition chamber without decreasing the thickness of the deposition. Electron microscopy in atmospheric chamber gives us the hindsight to compare the behaviour when water condensate on the fabric. When no perfluorinated coating is applied the sample tends to soak up the water to wrap the carbon fibres with water while when a coating is deposited, water droplets are formed without interacting with the fibres and are roundly shaped and squeezed between the threads highlighting the high hydrophobicity of the material. Results in testbench allows to probe the behaviour of a fuel cell, our three different samples were successively used in a cell and two tests were carried out at different level of humidity while maintaining a constant cell temperature at 75°C. Initially the idea to hydrophobized carbon fabrics fabric was to enhance the water management of the cell. The control sample (uncoated) shows that the humidity of the gas interacts with the hydrophilic surface and adsorb water which impacts the electrical conductivity of the gas diffusion layer which in turn poison the cell and makes the voltage drop to zero at an early stage. When we take a uniformly coated sample (40C with homogeneous fluorinated film) the behaviour is even worse and the voltage drops quickly to zero, though at higher humidity level a slight improvement is observed. The sample showing the occurrence of *rose petals* on the other, shows a steady behaviour with slow decrease in voltage throughout the ohmic region. The explanation for these two behaviours was explained with conductivity AFM. Sample 40C, having a homogeneous non conductive layer of perfluorinated film has a drastic drop in the ohmic region because of the high resistance to electrical contact in the cell.

Sample 20C on the other, having those *rose petals* structures, has conductive area and non_conductive areas, which confers a lower conductivity than when no coating is deposited but much higher than when the film is uniformly deposited. At the end of the day, sample 20C shows a respectful performance without reaching the mass transfer limitation over the range of current used in the test bench owing its good performance to the *rose petals* structure which confer a sufficient conductivity to withstand the high ohmic losses observed with the two other samples.

The third chapter focused on the synthesis of proton exchange membranes via remote plasma chemical vapour deposition. The initial scope of the present thesis was to use the PRODOS system to deposit such films, but this was not proven successful, and the equipment was used to produce elaborated gas diffusion layers as described in chapter ll. Nevertheless, the idea of producing proton exchange membrane via remote plasma deposition was not forgotten and a prototype was set up to overcome the limitations of the PRODOS system. Three distinct versions of the prototype were produced in an evolutive way to reach such a goal. The deposition of reference was the copolymerization of perfluoro(3-oxapent -4-ene) sulfonyl fluoride (also abbreviated PSVE) and hexafluoro-1,3- butadiene (HFBD). PSVE is a precursor of Aquivion™ which is a proton exchange membrane commercialized by Solvay® and is a short side chain (dangling bond) membrane conferring better proton conductivity compared to Nafion™ for example. HFBD was used as the polymer backbone from where the dangling bonds (PSVE) are attached. The choice for this precursor was based on its two double bonds which provides the possibility to ramify the polymer backbone chain. Ramifying the polymer chain can provide mechanical resistance without relying on the crystallization of linear backbone segments which in turn allows us to increase the quantity of dangling bond to increase the proton conductivity. Aquivion™ and Nafion™ are dependent on this crystalline phase to be self-supported but a crosslinked membrane could also make it self-supported.

The copolymerization reaction results were used as the benchmark to upgrade the prototype. The first version was based on the PRODOS™ and was a smaller version of it, the injection of HFBD was going through the inductive plasma unit, the PSVE being injected in the deposition chamber after the plasma zone. The results were not concluding as when we were trying to deposit films of HFBD, no deposition was obtain based on water contact test (surface should be hydrophobic). Further tests were obtained with optical emission spectroscopy, and we expected to see the CF_x light emission pattern but only argon (diluent gas) could be seen. The conclusion was that no film could be deposited on the substrate and the deposition occurred in the plasma chamber. This led us to rethink completely the technique to use.

The second version was designed based on the first remote plasma technique ever conceived. Only non-polymerizable gas can flow through the plasma to prevent deposition in the plasma chamber so we diverted the injection of HFBD to a ring located right above the substrate surface. A double O ring stack was designed to inject HFBD in one ring and PSVE in the other one and right above the substrate surface. Argon, nitrogen, oxygen can be activated in the plasma and make reactions occur downstream by reacting with the injected species in the double O ring. This upgrade was necessary to obtain films and the first attempts were successful in obtaining depositions. Depositing HFBD and PSVE was done by activating argon in the plasma chamber. The depositions were characterized with XPS, the films were mainly made out of carbon and fluorine. Sulphur was detected in the film showing that the incorporation of PSVE was successful. High resolution sulphur spectra were acquired and showed that three contributions were making the peaks (-SH, -SO_2 and -SO_2F). The contribution from -SO2F is the key group that we want to increase the predominance since we want to retain the conformation of the PSVE. Several samples were deposited by varying process parameters such as substrate temperature, plasma power, argon flow and substrate distance to the plasma zone in order to increase the contribution of -SO_2F. We could conclude from these samples that increasing the flow of argon was not interesting as it was destroying the film formation. With regard to the quantity of -SO_2F, low to no improvement could be observed from varying these parameters. The distance to the plasma showed the most improvement when the substrate was closer to the plasma zone, but no difference could be concluded from varying the other parameters. Cross analysis with TOF-SIMS were made and the presence of the PSVE parent precursor was observed showing that the -SO_2F signature was due to the incorporation of PSVE with conformation retention. With this second version we experimented new limitations that stems from the plasma unit. The process parameters that we wanted to modify were always in contradiction with the inductive plasma stability. Decreasing plasma power to prevent fragmentation of the precursors was problematic to the stability of the glow discharge. Moving the substrate closer to the plasma also injected the precursors closer to the plasma zone which would destabilise the glow discharge. Higher argon flow is good for plasma stability, but we observed that increasing it would impede the formation of the film. A higher flow of precursors could also increase the film deposition rate but increasing the quantity of precursors would also be problematic to the sustainability of the glow discharge. These limitations were extremely problematic to improve the quality of the films which led us to the conclusion that the plasma source should be changed.

The purpose of this 3rd and last version is to be able to increase the ratio of -SO_2F in the film by lowering the plasma power which could not be attained with the previous plasma unit. From discussions with the plasma group in LIST, they had a spare microwave plasma source that we could borrow for the last month of the thesis. With their advice we could mount this new plasma unit with minor changes to

the previous version. The microwave source borrowed can withstand low (0.01 mbar) and high pressure (atmospheric pressure plasma) while maintaining a homogeneous microwave glow discharge even with low power value which is what we were looking for after the limitations encountered in the second version of the prototype. With this version the activating gas was changed to nitrogen because the afterglow was much more intense than with argon. The characterization of the films used, once again, XPS as the reference. The samples were synthesized with much lower power (15 W to 60 W) than with the inductive plasma source, thanks to the stability of the microwave glow discharge. The first results were excellent, the quantity of -SH in the film remained extremely low in all the samples and the quantity of $-SO_2F$ group was drastically increase. Even more surprising was the occurrence of $-SO_3$ unit in the film, we observed a high oxygen contamination in the film and some of the $-SO_2F$ groups were converted by substitution of fluorine with oxygen. As the proton exchange membranes must be activated by the conversion of sulfonyl fluoride to sulfonate groups, this discovery came out as an interesting finding worth investigating. Furthermore, we observed that the lower the plasma power (e.g. 15 W) the higher the $-SO_3$ content. The film studied showed that a nitrogen flow below 100 sccm would yield a thin film highlighting the low deposition rate at lower nitrogen flow rate. These few findings helped us to consider low plasma power with high nitrogen flow rate to be the best parameters for proton exchange membranes deposition from PSVE and HFBD. The good results obtained were considered to be due to the microwave plasma source and the possibility to use low plasma power. Nitrogen could also be responsible for the soft activation of the polymerization, but further investigation should be carried out to affirm this allegation.

This left us with interesting perspectives for future investigations with this last upgrade. The first thing to do would be to investigate where the oxygen incorporated in the film comes from. This oxygen contaminant turned out to be a major advantage on the deposition of proton exchange membranes, but full control of the oxygen injection would be a powerful asset to investigate. The etching of the quartz tube and the stripping of oxygen could be a cause of the oxygen presence. Argon (and other noble gases) from the has the advantage to not alter the chemistry of the films formed unlike nitrogen which can incorporate in films. We tried to use argon as the activating gas, but the depositions were unsuccessful in the present configuration. Further tests could be carried out by lowering the microwave focuser height and put it closer to the deposition chamber so we can increase the plasma power and obtain an effective after glow discharge. Hydrogen plasma activation could also be an interesting opportunity. As hydrogen cannot make chemical functionalities, the hydrogen atoms could possibly provoke the polymerization without adding new chemical functionalities in the film (unlike nitrogen). The optimization of the film in terms of deposition rate (reach higher thicknesses in a short time), quantity of $-SO_3$ functionalities and the role of substrate temperature should be further

investigated. A fine control of the deposition chamber pressure could be an interesting asset to have. In order to reach that, a new pump with larger volume evacuation capability should be connected. The base pressure would remain the same, but the flow of gases would not play a role in the total pressure measured. Additionally, a device to regulate the pressure inside the chamber could be mounted (e.g. a automatic pressure regulation valve).

ANNEX 1: LIST OF PUBLICATIONS, CONFERENCES AND ECTS

PUBLICATIONS

- **Chemical Vapor Deposition for Advanced Polymer Electrolyte Fuel Cell Membranes**

  Nicolas Bellomo, Dr. Marc Michel, Dr. Bianca Rita Pistillo, Dr. Robin J. White, Dr. Emanuele Barborini, Dr. Damien Lenoble

  First published: 25 November 2021

  https://doi.org/10.1002/celc.202101019

  ChemELectroChem (IF: 4.782)

- **Dry gaseous remote plasma deposition of perfluorinated material with tuneable crystallinity and hydrophobic properties**

  Nicolas Bellomo, Kevin Menguelti, Yves Fleming, Christèle Vergne, Bianca Rita Pistillo, Emanuele Barborini, MarcMichel

  https://doi.org/10.1016/j.vacuum.2022.111190

  VACUUM (IF: 4.11)

- **Elaboration of efficient gas diffusion layer by gas phase hydrophobization of conductive carbon fibres cloths**

  Nicolas Bellomo, Charlotte Stoffels, Patrick Grysan, Gregor Hoogers, Vishnu Pullangatil, Marc Michel

  To be published…

- **Introduction to Fuel Cell, Electrolyser, and Battery Technologies: low temperature fuel cells and electrolysers – Athens 14/09/2019-21/09/2019**

- **6th Plasma Workshop: talk about PRAP-CVD – Luxembourg 14 & 15 November 2019**

Vision Dynamics
Science & Entrepreneurship

- **Carbon 2022 – Carbon for a cleaner future - The world conference on carbon – Hosted by British carbon group – Imperial College London (3rd -8th of July 2022)**

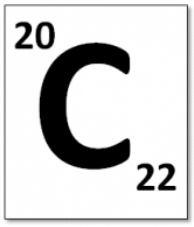

- **ECOSS35 – European Conference On Surface Science (29th of august – 02 September 2022)**

ECTS

Total ECTS awarded	**20**
Disciplinary/Interdisciplinary ECTS	9
Transferable Skills ECTS	11

Disciplinary / Interdisciplinary ECTS

Activity Title	Place	Date(s)/Period	ECTS
Characterization of Polymers and Plastics	University of Luxembourg	19-23.04.2021	1
Joint European Summer School 2019 on Fuel Cell, Electrolyser and Battery Technologies	Vouliagmeni, Athens, Greece	15.09 - 21.09.2019	2
Microscopy and chemical analysis using charged particles	University of Luxembourg	17.11 - 08.12.2020	1
PLASMA Science and Entrepreneurship Workshop	Luxembourg Institute of Science and Technology	14.11 - 15.11.2019	2
Solar Cells Basics - Thermodynamics	University of Luxembourg	16-27.09.2021	1
Structural and chemical characterization of materials	University of Luxembourg	05.10 - 05.11.2021	1
Poster presentation at Carbon 2022 conference in London	Imperial College London	03-07-2022 to 08-07-2022	1
		Total	**9**

Transferable Skills ECTS

Activity Title	Place	Date(s)/Period	ECTS
8th IDEATION Camp	University of Luxembourg	27.4 - 1.5.2021	3
Developing Writing Skills at Doctoral Level (Advanced)	University of Luxembourg	18.10 - 19.10.2019	1
Italian Course A2-B1	University of Luxembourg	Winter Semester 2019 - 2020	1
Reduce your stress and develop more focus	University of Luxembourg	13.11 - 11.12.2019	1
Research Integrity & Ethics	Virt2ue blended learning	30.09 - 01.10.2021	1
Science Communication	University of Luxembourg	08.11 - 15.12.2021	2
Scientific Publication: an Editor's Point of View	University of Luxembourg	13-20.10.2021	1
Fundamental of Project Management	Université du Luxembourg	16-03-2022 to 18-03-2022	1
		Total	**11**

a

ACKNOWLEDGEMENT

I would like to acknowledge and give my warmest thanks to my supervisor Marc Michel who made this work possible. His guidance and advice carried me through all the stages of research in this project.

Thanks to Stéphanie Roualdès and Andreas Michels for being part of this journey for the last four years as CET members.

I would also like to thank the jury members Stéphanie Roualdès-Boutevin, Andreas Michels, Jérôme Polesel and Vincent Ball for being part of this defense and bringing their knowledge along to open for discussion.

I would like to thank my former supervisers Bianca Rita Pistillo and Damien Lenoble for their support in the beginning of the thesis.

I would give a special thank to Kevin Menguelti, Julien Jacob, Jérémy Raguin, Vincent Rogé for their valuable professional help.

I would also like to give special thanks to my family as a whole for their continuous support and understanding when undertaking my research and writing my project.

Last but not least I would like to thank my friends and colleagues for being there and make this whole experience bearable on a social aspect.

BIBLIOGRAPHY

[1] M. Ball, M. Weeda, *Int. J. Hydrogen Energy* **2015**, *40*, 7903–7919.

[2] O. Z. Sharaf, M. F. Orhan, *Renew. Sustain. Energy Rev.* **2014**, *32*, 810–853.

[3] E. I. Ortiz-Rivera, A. L. Reyes-Hernandez, R. A. Febo, *2007 IEEE Conf. Hist. Electr. Power, HEP 2007* **2007**, *2*, 117–122.

[4] V. A. Goltsov, T. N. Veziroglu, *Int. J. Hydrogen Energy* **2001**, *26*, 909–915.

[5] K. L. Cashdollar, I. A. Zlochower, G. M. Green, R. A. Thomas, M. Hertzberg, *J. Loss Prev. Process Ind.* **2000**, *13*, 327–340.

[6] E. Dündar-Tekkaya, Y. Yürüm, *Int. J. Hydrogen Energy* **2016**, *41*, 9789–9795.

[7] B. Zhang, S. X. Zhang, R. Yao, Y. H. Wu, J. S. Qiu, *J. Electron. Sci. Technol.* **2021**, *19*, 1–15.

[8] T. Smolinka, in (Ed.: J.B.T.-E. of E.P.S. Garche), Elsevier, Amsterdam, **2009**, pp. 394–413.

[9] A. Hodges, A. L. Hoang, G. Tsekouras, K. Wagner, C. Y. Lee, G. F. Swiegers, G. G. Wallace, *Nat. Commun.* **2022**, *13*, 1–11.

[10] M. F. Ahmad Kamaroddin, N. Sabli, T. A. Tuan Abdullah, S. I. Siajam, L. C. Abdullah, A. Abdul Jalil, A. Ahmad, *Membranes (Basel).* **2021**, *11*, 1–27.

[11] J. G. Speight, in (Ed.: J.G.B.T.-T.R. of the F. (Second E. Speight), Gulf Professional Publishing, **2020**, pp. 515–548.

[12] T. Marzoughi, F. Samimi, M. R. Rahimpour, *Chem. Prod. Process Model.* **2021**, DOI doi:10.1515/cppm-2021-0029.

[13] G. L. Chiarello, E. Selli, *Photocatalytic Production of Hydrogen*, Woodhead Publishing Limited, **2014**.

[14] C. T. Gray, H. Gest, *Science (80-.).* **1965**, *148*, 186–192.

[15] I. Ntaikou, in (Eds.: S. Dutta, C.B.T.-S.F.T.H. Mustansar Hussain), Academic Press, **2021**, pp. 315–337.

[16] A. Prinzhofer, I. Moretti, J. Françolin, C. Pacheco, A. D'Agostino, J. Werly, F. Rupin, *Int. J. Hydrogen Energy* **2019**, *44*, 5676–5685.

[17] E. Deville, A. Prinzhofer, *Hydrogène Naturel: La Prochaine Révolution Énergétique?*, Belin Éditeur, **2017**.

[18] A. Prinzhofer, C. S. Tahara Cissé, A. B. Diallo, *Int. J. Hydrogen Energy* **2018**, *43*, 19315–19326.

[19] J. Guélard, V. Beaumont, V. Rouchon, F. Guyot, D. Pillot, D. Jézéquel, M. Ader, K. D. Newell, E. Deville, *Geochemistry, Geophys. Geosystems* **2017**, *18*, 1841–1865.

[20] V. A. Nivin, V. V Pukha, A. V Lovchikov, R. G. Rakhimov, *Dokl. Earth Sci.* **2016**, *471*, 1261–1264.

[21] B. S. Lollar, G. Lacrampe-Couloume, K. Voglesonger, T. C. Onstott, L. M. Pratt, G. F. Slater, *Geochim. Cosmochim. Acta* **2008**, *72*, 4778–4795.

[22] V. A. Nivin, *Appl. Geochemistry* **2016**, *74*, 44–55.

[23] N. Larin, V. Zgonnik, S. Rodina, E. Deville, A. Prinzhofer, V. N. Larin, *Nat. Resour. Res.* **2015**, *24*, 369–383.

[24] V. Zgonnik, V. Beaumont, E. Deville, N. Larin, D. Pillot, K. M. Farrell, *Prog. Earth Planet. Sci.* **2015**, *2*, 31.

[25] I. Moretti, H. Pierre, *N march* **2018**, 28.

[26] I. Moretti, M. E. Webber, *Renew. matter* **2021**.

[27] I. Dincer, *Int. J. Hydrogen Energy* **2012**, *37*, 1954–1971.

[28] R. Yukesh Kannah, S. Kavitha, Preethi, O. Parthiba Karthikeyan, G. Kumar, N. V. Dai-Viet, J. Rajesh Banu, *Bioresour. Technol.* **2021**, *319*, 124175.

[29] N. Bellomo, M. Michel, B. R. Pistillo, R. J. White, E. Barborini, D. Lenoble, *ChemElectroChem* **2022**, *9*, e202101019.

[30] Oxford Economics, *BEIS Res. Pap.* **2020**, *2020/010*, 233.

[31] T. Yamada, M. Ishihara, J. Kim, M. Hasegawa, S. Iijima, *Carbon N. Y.* **2012**, *50*, 2615–2619.

[32] H. Şakalak, K. Yılmaz, M. Gürsoy, M. Karaman, *Chem. Eng. Sci.* **2020**, *215*, 115466.

[33] B. Van Aken, M. Dorenkamper, C. Devilee, M. Heijna, J. Loffler, W. J. Soppe, *Roll to Roll Fabrication Process of Thin Film Silicon Solar Cells on Steel Foil*, **2009**.

[34] C. Cheng, M. Gupta, *Ind. Eng. Chem. Res.* **2018**, *57*, 11675–11680.

[35] C. Spiegel, in (Ed.: C.B.T.-P.E.M.F.C.M. and S.U.M. Spiegel), Academic Press, Burlington, **2008**,

pp. 49–76.

[36] C. Qin, *J. Electrochem. Soc.* **2015**, *162*, F1036–F1046.

[37] P. M. Wilde, M. Mändle, M. Murata, N. Berg, *Fuel Cells* **2004**, *4*, 180–184.

[38] M. Mathias, J. Roth, J. Fleming, W. Lehnert, in *Handb. Fuel Cells - Fundam. Technol. Appl.*, **2003**, pp. 517–537.

[39] E. Sadeghi, M. Bahrami, N. Djilali, *J. Power Sources* **2008**, *179*, 200–208.

[40] Y. Utaka, Y. Tasaki, S. Wang, T. Ishiji, S. Uchikoshi, *Int. J. Heat Mass Transf.* **2009**, *52*, 3685–3692.

[41] G. H. Yoon, Y. il Park, *Int. J. Precis. Eng. Manuf.* **2012**, *13*, 1153–1159.

[42] C. M. Lee, Y. H. Pai, J. M. Zen, F. S. Shieu, *Mater. Chem. Phys.* **2009**, *114*, 151–155.

[43] C. Lim, C. Y. Wang, *Electrochim. Acta* **2004**, *49*, 4149–4156.

[44] W. M. Yan, C. Y. Hsueh, C. Y. Soong, F. Chen, C. H. Cheng, S. C. Mei, *Int. J. Hydrogen Energy* **2007**, *32*, 4452–4458.

[45] F. B. Weng, C. Y. Hsu, M. C. Su, *Int. J. Hydrogen Energy* **2011**, *36*, 13708–13714.

[46] T. Kitahara, H. Nakajima, M. Morishita, *J. Power Sources* **2012**, *214*, 100–106.

[47] T. Kitahara, H. Nakajima, K. Mori, *J. Power Sources* **2012**, *199*, 29–36.

[48] M. J. Leeuwner, D. P. Wilkinson, E. L. Gyenge, *Fuel Cells* **2015**, *15*, 790–801.

[49] G. Velayutham, *Int. J. Hydrogen Energy* **2011**, *36*, 14845–14850.

[50] S. Latorrata, M. Sansotera, M. Gola, P. G. Stampino, W. Navarrini, G. Dotelli, *Fuel Cells* **2020**, *20*, 166–175.

[51] S. Latorrata, P. Gallo Stampino, C. Cristiani, G. Dotelli, *Int. J. Hydrogen Energy* **2014**, *39*, 5350–5357.

[52] A. L. Ong, A. Bottino, G. Capannelli, A. Comite, *J. Power Sources* **2008**, *183*, 62–68.

[53] C. S. Kong, D. Y. Kim, H. K. Lee, Y. G. Shul, T. H. Lee, *J. Power Sources* **2002**, *108*, 185–191.

[54] R. Lan, S. Tao, *Front. Energy Res.* **2014**, *2*.

[55] U. B. Demirci, *J. Power Sources* **2007**, *169*, 239–246.

[56] R. K. Shah, U. Desideri, K. L. Hsueh, A. V Vikar, B. Sunden, J. Vilemas, *Adv. Heat Transf. Eng. Proc.* **2003**.

[57] G. Jeerh, M. Zhang, S. Tao, *J. Mater. Chem. A* **2021**, *9*, 727–752.

[58] U. Lucia, *Renew. Sustain. Energy Rev.* **2014**, *30*, 164–169.

[59] L. Yang, J. Shui, L. Du, Y. Shao, J. Liu, L. Dai, Z. Hu, *Adv. Mater.* **2019**, *31*, 1–20.

[60] A. Eftekhari, *Int. J. Hydrogen Energy* **2017**, *42*, 11053–11077.

[61] T. Ioroi, Z. Siroma, S. ichi Yamazaki, K. Yasuda, *Adv. Energy Mater.* **2019**, *9*, 1–20.

[62] E. Quartarone, S. Angioni, P. Mustarelli, *Materials (Basel).* **2017**, *10*, 687.

[63] S. J. Peighambardoust, S. Rowshanzamir, M. Amjadi, *Int. J. Hydrogen Energy* **2010**, *35*, 9349–9384.

[64] J. Walkowiak-Kulikowska, J. Wolska, H. Koroniak, *Phys. Sci. Rev.* **2017**, *2*, 1–34.

[65] W. A. Meulenberg, M. E. Ivanova, J. M. Serra, S. Roitsch, in *Adv. Membr. Sci. Technol. Sustain. Energy Environ. Appl.*, **2011**, pp. 541–567.

[66] E. M. W. Tsang, S. Holdcroft, in *Polym. Sci. A Compr. Ref. 10 Vol. Set*, Elsevier B.V., **2012**, pp. 651–689.

[67] T. Kumagai, H. Okuyama, in *Encycl. Interfacial Chem. Surf. Sci. Electrochem.*, Elsevier, **2018**, pp. 64–73.

[68] J. Wei, *Proton-Conducting Materials Used as Polymer Electrolyte Membranes in Fuel Cells*, Elsevier Inc., **2018**.

[69] J. Walkowiak-Kulikowska, J. Wolska, H. Koroniak, *Biopolymer Membranes in Fuel Cell Applications*, Elsevier Inc., **2020**.

[70] M. Toupin, K. Malek, A. Mokrini, *World Electr. Veh. J.* **2016**, *8*, 431–442.

[71] A. Ennajdaoui, S. Roualdes, P. Brault, J. Durand, *J. Power Sources* **2010**, *195*, 232–238.

[72] J. Friedrich, *Plasma Process. Polym.* **2011**, *8*, 783–802.

[73] Z. Jiang, Z. J. Jiang, *RSC Adv.* **2012**, *2*, 2743–2747.

[74] Z. Jiang, Z. J. Jiang, *Int. J. Hydrogen Energy* **2012**, *37*, 11276–11289.

[75] J. Bassil, S. Roualdès, V. Flaud, J. Durand, *J. Memb. Sci.* **2014**, *461*, 1–9.

[76] A. J. Kinfack Leoga, L. Youssef, S. Roualdès, V. Rouessac, *Thin Solid Films* **2018**, *660*, 506–515.

[77] S. M. Smith, S. A. Voight, H. Tompkins, A. Hooper, A. A. Talin, J. Vella, *Thin Solid Films* **2001**, *398–399*, 163–169.

[78] S. H. Cho, Z. T. Park, J. G. Kim, J. H. Boo, *Surf. Coatings Technol.* **2003**, *174–175*, 1111–1115.

[79] J. G. Riess, *Artif. Cells. Blood Substit. Immobil. Biotechnol.* **2005**, *33*, 47–63.

[80] J. Thery, S. Martin, V. Faucheux, L. Le Van Jodin, D. Truffier-Boutry, A. Martinent, J. Y. Laurent, *J. Power Sources* **2010**, *195*, 5573–5580.

[81] T. J. Wood, J. P. S. Badyal, *ACS Appl. Mater. Interfaces* **2012**, *4*, 1675–1682.

[82] H. C. Chien, L. D. Tsai, C. M. Lai, J. N. Lin, C. Y. Zhu, F. C. Chang, *J. Power Sources* **2013**, *226*, 87–93.

[83] G. Urstöger, R. Resel, G. Koller, A. M. Coclite, *J. Appl. Phys.* **2016**, *119*.

[84] P. Bosso, A. Milella, V. Armenise, F. Fanelli, F. Fracassi, *Vacuum* **2021**, *184*, 109933.

[85] A. M. Coclite, P. Lund, R. Di Mundo, F. Palumbo, *Polymer (Guildf).* **2013**, *54*, 24–30.

[86] A. M. Coclite, R. M. Howden, D. C. Borrelli, C. D. Petruczok, R. Yang, J. L. Yagüe, A. Ugur, N. Chen, S. Lee, W. J. Jo, A. Liu, X. Wang, K. K. Gleason, *Adv. Mater.* **2013**, *25*, 5392–5423.

[87] C. Ranacher, R. Resel, P. Moni, B. Cermenek, V. Hacker, A. M. Coclite, *Macromolecules* **2015**, *48*, 6177–6185.

[88] V. V. Volkov, N. A. Platé, A. Takahara, T. Kajiyama, N. Amaya, Y. Murata, *Polymer (Guildf).* **1992**, *33*, 1316–1320.

[89] K. Honda, M. Morita, H. Otsuka, A. Takahara, *Macromolecules* **2005**, *38*, 5699–5705.

[90] A. M. Coclite, Y. Shi, K. K. Gleason, *Adv. Funct. Mater.* **2012**, *22*, 2167–2176.

[91] A. C. Jones, M. L. Hitchman, Eds. , in *Chem. Vap. Depos. Precursors, Process. Appl.*, The Royal Society Of Chemistry, **2009**, pp. 1–36.

[92] C. D. Petruczok, N. Chen, K. K. Gleason, *Langmuir* **2014**, *30*, 4830–4837.

[93] J. Batey, E. Tierney, *J. Appl. Phys.* **1986**, *60*, 3136–3145.

[94] N. Gherardi, S. Martin, F. Massines, *J. Phys. D. Appl. Phys.* **2000**, *33(19)*, 104–108.

[95] S. K. Ray, C. K. Maiti, S. K. Lahiri, N. B. Chakrabarti, *J. Vac. Sci. Technol. B Microelectron.*

Nanom. Struct. **1992**, *10*, 1139.

[96] S. K. Ray, C. K. Maiti, S. K. Lahiri, N. B. Chakrabarti, *Adv. Mater. Opt. Electron.* **1996**, *6*, 73–82.

[97] P. Lunca Popa, J. Crêpellière, R. Leturcq, D. Lenoble, *Thin Solid Films* **2016**, *612*, 194–201.

[98] R. Puurunen, J. Saarilahti, H. Kattelus, *ECS Trans.* **2007**, *11 (7)*, 3–14.

[99] J. P. Lock, J. L. Lutkenhaus, N. S. Zacharia, S. G. Im, P. T. Hammond, K. K. Gleason, *Synth. Met.* **2007**, *157*, 894–898.

[100] S. Lee, K. K. Gleason, *Adv. Funct. Mater.* **2015**, *25*, 85–93.

[101] T. Wang, H. W. Xin, Z. M. Zhang, Y. B. Dai, H. S. Shen, *Diam. Relat. Mater.* **2004**, *13*, 6–13.

[102] T. P. Martin, S. E. Kooi, S. H. Chang, K. L. Sedransk, K. K. Gleason, *Biomaterials* **2007**, *28*, 909–915.

[103] J. J. Yu, I. W. Boyd, *Appl. Phys. A Mater. Sci. Process.* **2002**, *75*, 489–491.

[104] K. K. Gleason, *Nat. Rev. Phys.* **2020**, *2*, 347–364.

[105] J. O. Carlsson, P. M. Martin, *Chemical Vapor Deposition*, Elsevier Ltd., **2010**.

[106] K. K. Gleason, *CVD Polym. Fabr. Org. Surfaces Devices* **2015**, *1*, 1–11.

[107] A. C. Jones, M. L. Hitchman, **2009**.

[108] L. Sun, G. Yuan, L. Gao, J. Yang, M. Chhowalla, Gharahcheshmeh, M. Heydari, K. K. Gleason, Y. S. Choi, B. H. Hong, Z. Liu, *Nat. Rev. Methods Prim.* **2021**, *1*, 1–20.

[109] A. Khlyustova, Y. Cheng, R. Yang, *J. Mater. Chem. B* **2020**, *8*, 6588–6609.

[110] K. L. Choy, *Prog. Mater. Sci.* **2003**, *48*, 57–170.

[111] B. Reeja-Jayan, P. Kovacik, R. Yang, H. Sojoudi, A. Ugur, D. H. Kim, C. D. Petruczok, X. Wang, A. Liu, K. K. Gleason, *Adv. Mater. Interfaces* **2014**, *1*, 1–30.

[112] J. S. Goela, R. L. Taylor, *J. Mater. Sci.* **1988**, *23*, 4331–4339.

[113] E. G. J. Staring, D. Braun, G. L. J. A. Rikken, R. J. C. E. Demandt, Y. A. R. R. Kessener, M. Bouwmans, D. Broer, *Synth. Met.* **1994**, *67*, 71–75.

[114] V. Verlaan, R. Bakker, C. H. M. van der Werf, Z. S. Houweling, Y. Mai, J. K. Rath, R. E. I. Schropp, *Surf. Coatings Technol.* **2007**, *201*, 9285–9288.

[115] K. S. Yeung, Y. W. Lam, *Thin Solid Films* **1983**, *109*, 169–178.

[116] N. Menou, H. Kuwabara, H. Funakubo, *Jpn. J. Appl. Phys.* **2007**, *46*, 2139–2142.

[117] M. T. Laugier, *J. Mater. Sci.* **1986**, *21*, 2269–2272.

[118] L. Lhermitte-Sebire, R. Colmet, R. R. Naslain, J. G. Desmaison, G. Gladel, *Thin Solid Films* **1986**, *138*, 221–233.

[119] Q. He, D. C. Joy, D. J. Keffer, *J. Power Sources* **2013**, *241*, 634–646.

[120] S. Zhang, Y. Shao, G. Yin, Y. Lin, *J. Mater. Chem.* **2009**, *19*, 7995–8001.

[121] P. K. Bachmann, D. Leers, H. Lydtin, *Diam. Relat. Mater.* **1991**, *1*, 12.

[122] P. Tägtström, U. Jansson, *Thin Solid Films* **1999**, *352*, 107–113.

[123] L. Vandenbulcke, *Thin Solid Films* **1983**, *102*, 149–160.

[124] A. Abrutis, M. Lukosius, Z. Saltyte, R. Galvelis, P. K. Baumann, M. Schumacher, J. Lindner, *Thin Solid Films* **2008**, *516*, 4758–4764.

[125] K. L. Kim, W. Lee, S. K. Hwang, S. H. Joo, S. M. Cho, G. Song, S. H. Cho, B. Jeong, I. Hwang, J. H. Ahn, Y. J. Yu, T. J. Shin, S. K. Kwak, S. J. Kang, C. Park, *Nano Lett.* **2016**, *16*, 334–340.

[126] S. Bonomi, L. Malavasi, *J. Vac. Sci. Technol. A* **2020**, *38*, 060803.

[127] K. J. Blakeney, C. H. Winter, *Chem. Mater.* **2018**, *30*, 1844–1848.

[128] J. C. Hierso, C. Satto, R. Feurer, P. Kalck, *Chem. Mater.* **1996**, *8*, 2481–2485.

[129] A. Blum, *Environ. Health Perspect.* **2015**, *123*, A107–A111.

[130] S. H. Baxamusa, S. G. Im, K. K. Gleason, *Phys. Chem. Chem. Phys.* **2009**, *11*, 5227–5240.

[131] M. E. Alf, A. Asatekin, M. C. Barr, S. H. Baxamusa, H. Chelawat, G. Ozaydin-Ince, C. D. Petruczok, R. Sreenivasan, W. E. Tenhaeff, N. J. Trujillo, S. Vaddiraju, J. Xu, K. K. Gleason, *Adv. Mater.* **2010**, *22*, 1993–2027.

[132] P. Karfa, K. C. Majhi, R. Madhuri, in *Two-Dimensional Nanostructures Biomed. Technol. A Bridg. between Mater. Sci. Bioeng.*, Elsevier B.V., **2019**, pp. 35–71.

[133] B. B. Van Aken, M. Dörenkämper, C. Devilee, M. C. R. Heijna, in *Int. Conf. Coatings Glas. Plast.*, **2008**, pp. 001381–001385.

[134] H. Şakalak, K. Yılmaz, M. Gürsoy, M. Karaman, *Chem. Eng. Sci.* **2019**, 115466.

[135] K. D. Kreuer, *Chem. Mater.* **2014**, *26*, 361–380.

[136] S. Holdcroft, *Chem. Mater.* **2014**, *26*, 381–393.

[137] J. Miyake, K. Miyatake, *Polym. J.* **2017**, *49*, 487–495.

[138] R. J. Goldston, *Introduction to Plasma Physics*, CRC Press, **2020**.

[139] K. Wiesemann, *arXiv Prepr. arXiv1404.0509* **2014**.

[140] E. Yiğit, in *Atmos. Sp. Sci. Ionos. Plasma Environ. Vol. 2*, Springer International Publishing, Cham, **2018**, pp. 1–19.

[141] J. A. Bittencourt, in *Fundam. Plasma Phys.*, Springer New York, New York, NY, **2004**, pp. 1–32.

[142] A. Z. Akcasu, L. H. Wald, *Phys. Fluids* **1967**, *10*, 1327–1335.

[143] H. Conrads, M. Schmidt, *Plasma Sources Sci. Technol* **2000**, *9*, 441–454.

[144] F. Paschen, *Wied. Ann* **1889**, *37*, 69–96.

[145] J.-M. Torres, R. S. Dhariwal, *Microsyst. Technol.* **1999**, *6*, 6–10.

[146] W. S. Boyle, F. E. Haworth, *Phys. Rev.* **1956**, *101*, 935–938.

[147] G. Francis, *The Glow Discharge at Low Pressure*, **1956**.

[148] M. A. Lieberman, A. J. Lichtenberg, *MRS Bull.* **1994**, *30*, 899–901.

[149] Y. Setsuhara, *Plasma Sources in Thin Film Deposition*, Elsevier, **2014**.

[150] J. Hopwood, *Plasma Sources Sci. Technol.* **1992**, *1*, 109.

[151] W. Ahmed, H. Sein, M. Jackson, C. Rego, I. U. Hassan, K. Subramani, J. Yazdani, in *Micro Nano Technol.* (Eds.: K. Subramani, W.B.T.-E.N. in D. Ahmed), William Andrew Publishing, Boston, **2012**, pp. 239–272.

[152] T. Ishijima, Y. Nojiri, H. Toyoda, H. Sugai, *Jpn. J. Appl. Phys.* **2010**, *49*, 86002.

[153] P. D. Richard, R. J. Markunas, G. Lucovsky, G. G. Fountain, A. N. Mansour, D. V. Tsu, *J. Vac. Sci. Technol. A Vacuum, Surfaces, Film.* **1985**, *3*, 867–872.

[154] G. Lucovsky, P. D. Richard, D. V Tsu, R. J. Markunas, *MRS Proc.* **1985**, *54*, 529.

[155] S. E. Alexandrov, M. L. Hitchman, S. Shamlian, *Adv. Mater. Opt. Electron.* **1993**, *2*, 301–312.

[156] G. R. Nowling, S. E. Babayan, V. Jankovic, R. F. Hicks, *Plasma Sources Sci. Technol.* **2002**, *11*, 97–103.

[157] M. J. Kushner, *J. Appl. Phys.* **1992**, *71*, 4173–4189.

[158] G. Lucovsky, D. V. Tsu, *J. Vac. Sci. Technol. A Vacuum, Surfaces, Film.* **1987**, *5*, 2231–2238.

[159] M. J. Kushner, *J. Appl. Phys.* **1993**, *74*, 6538–6553.

[160] A. Gallagher, *Int. J. Sol. Energy* **1987**, *5*, 311–322.

[161] M. Bavafa, H. Ilati, B. Rashidian, *Semicond. Sci. Technol.* **2008**, *23*, DOI 10.1088/0268-1242/23/9/095023.

[162] D. Mataras, S. Cavadias, D. Rapakoulias, *J. Appl. Phys.* **1989**, *66*, 119–124.

[163] D. J. Dagel, C. M. Mallouris, J. R. Doyle, *J. Appl. Phys.* **1996**, *79*, 8735–8747.

[164] R. J. Buss, *J. Appl. Phys.* **1986**, *59*, 2977–2982.

[165] M. Hori, T. Goto, *Appl. Surf. Sci.* **2007**, *253*, 6657–6671.

[166] I. Pérès, M. J. Kushner, *Plasma Sources Sci. Technol.* **1996**, *5*, 499–509.

[167] N. Bellomo, K. Menguelti, Y. Fleming, B. Rita, E. Barborini, M. Michel, **2022**, *202*, 0–6.

[168] K. Tachibana, M. Nishida, H. Harima, Y. Urano, *J. Phys. D. Appl. Phys.* **1984**, *17*, 1727–1742.

[169] O. V. Balachova, M. A. R. Alves, J. W. Swart, E. S. Braga, L. Cescato, *Microelectronics J.* **2000**, *31*, 213–215.

[170] J. H. Wang, in *Woodhead Publ. Ser. Biomater.* (Ed.: M.B.T.-C. for B.A. Driver), Woodhead Publishing, **2012**, pp. 143–175.

[171] L. G. Jacobsohn, D. F. Franceschini, M. E. H. Maia da Costa, F. L. Freire, *J. Vac. Sci. Technol. A Vacuum, Surfaces, Film.* **2000**, *18*, 2230.

[172] C. Suzuki, K. Sasaki, K. Kadota, *Japanese J. Appl. Physics, Part 1 Regul. Pap. Short Notes Rev. Pap.* **1998**, *37*, 5763–5766.

[173] G. Cunge, J. P. Booth, *J. Appl. Phys.* **1999**, *85*, 3952–3959.

[174] W. Schwarzenbach, G. Cunge, J. P. Booth, *J. Appl. Phys.* **1999**, *85*, 7562–7568.

[175] R. d'Agostino, F. Cramarossa, F. Fracassi, F. Illuzzi, in *Plasma Depos. Treat. Etch. Polym.*, Chapter, **1990**, pp. 95–162.

[176] D. G. Castner, P. Favia, B. D. Ratner, in *Surf. Modif. Polym. Biomater.*, **1996**, pp. 45–52.

[177] I. T. Martin, G. S. Malkov, C. I. Butoi, E. R. Fisher, I. T. Martin, G. S. Malkov, C. I. Butoi, E. R.

Fisher, **2009**, *227*, DOI 10.1116/1.1638779.

[178] R. d'Agostino, F. Cramarossa, F. Fracassi, F. Illuzzi, in *Plasma–Materials Interact.* (Ed.: R.B.T.-P.D. d'Agostino Treatment, and Etching of Polymers), Academic Press, San Diego, **1990**, pp. 95–162.

[179] H. Yasuda, in (Ed.: H.B.T.-P.P. Yasuda), Academic Press, **1985**, pp. 334–369.

[180] Y. Momose, T. Takada, S. Okagaki, in *Proc. ACS Div. Polym. Mater. Denver*, **1987**, p. 236.

[181] D. W. Grainger, C. W. Stewart, *ACS Symp. Ser.* **2001**, *787*, 1–14.

[182] J. B. Gilbert, M. F. Rubner, R. E. Cohen, *Proc. Natl. Acad. Sci. U. S. A.* **2013**, *110*, 6651–6656.

[183] M. Wojdyr, *J. Appl. Crystallogr.* **2010**, *43*, 1126–1128.

[184] O. S. Ovchinnikova, N. Borodinov, A. A. Trofimov, S. T. King, M. Lorenz, W. Lamberti, D. Abmayr, A. V Ievlev, *ACS Appl. Polym. Mater.* **2021**, *3*, 3478–3484.

[185] N. Bellomo, K. Menguelti, Y. Fleming, C. Vergne, B. R. Pistillo, E. Barborini, M. Michel, *Vacuum* **2022**, *202*, 111190.

[186] H. Yasuda, T. Hirotsu, *J. Polym. Sci. Polym. Chem. Ed.* **1978**, *16*, 743–759.

[187] J. Piwowarczyk, R. Jedrzejewski, D. Moszyński, K. Kwiatkowski, A. Niemczyk, J. Baranowska, *Polymers (Basel).* **2019**, *11*, 1–13.

[188] G. Beamson, D. R. Briggs, **1992**.

[189] Y. A. Lebedev, Y. M. Korolev, A. V. Rebrov, L. N. Ignat'eva, E. M. Antipova, *Crystallogr. Reports* **2010**, *55*, 615–620.

[190] F. Song, Q. Wang, T. Wang, *Tribol. Int.* **2016**, *93*, 1–10.

[191] Q. H. Trinh, D. B. Nguyen, M. M. Hossain, Y. S. Mok, *Surf. Coatings Technol.* **2019**, *361*, 377–385.

[192] S. Orazbayev, R. Zhumadilov, A. Zhunisbekov, M. Gabdullin, Y. Yerlanuly, A. Utegenov, T. Ramazanov, *Appl. Surf. Sci.* **2020**, *515*, 146050.

[193] S. Orazbayev, M. Gabdullin, T. Ramazanov, M. Dosbolayev, D. Omirbekov, Y. Yerlanuly, *Appl. Surf. Sci.* **2019**, *472*, 127–134.

[194] J. Berndt, H. Acid, E. Kovacevic, C. Cachoncinlle, T. Strunskus, L. Boufendi, *J. Appl. Phys.* **2013**, *113*, DOI 10.1063/1.4789949.

[195] D. M. Lopes, S. M. M. Ramos, L. R. De Oliveira, J. C. M. Mombach, *RSC Adv.* **2013**, *3*, 24530–24534.

[196] D. O'hagan, *Chem. Soc. Rev.* **2008**, *37*, 308–319.

[197] R. W. Collins, J. M. Cavese, *Appl. Phys. Lett.* **1986**, *49*, 1207–1209.

[198] P. M. Winkler, P. E. Wagner, *J. Aerosol Sci.* **2022**, *159*, 105875.

[199] V. Talanquer, *J. Chem. Educ.* **2002**, *79*, 877.

[200] A. Rudin, P. Choi, in (Eds.: A. Rudin, P.B.T.-T.E. of P.S.& E. (Third E. Choi), Elsevier Inc., Boston, **2013**, pp. 1–62.

[201] T. A. Saleh, in *Polym. Hybrid Mater. Nanocomposites* (Ed.: T.A. Saleh), Elsevier Inc., **2021**, pp. 59–103.

[202] Z. H. Wang, C. Y. Wang, *ASME Int. Mech. Eng. Congr. Expo. Proc.* **2000**, *2000-S*, 27–33.

[203] W. Chanpeng, Y. Khunatorn, *Energy Procedia* **2011**, *9*, 316–325.

[204] L. Merlo, C. Oldani, M. Apostolo, V. Arcella, *Fuel Cells* **2012**, 34.

[205] A. Kraytsberg, Y. Ein-Eli, *Energy and Fuels* **2014**, *28*, 7303–7330.

[206] S. M. Slade, T. R. Ralph, C. P. De León, S. A. Campbell, F. C. Walsh, *Fuel Cells* **2010**, *10*, 567–574.

[207] J. Han, D. G. Cho, R. Mauchauffé, S. Y. Moon, *Rev. Sci. Instrum.* **2020**, *91*, DOI 10.1063/1.5136284.

[208] S. Iordanova, I. Koleva, *Spectrochim. Acta Part B At. Spectrosc.* **2007**, *62*, 344–356.

[209] J. S. Park, D. S. Seo, H. W. Kim, S. J. Hong, *J. Korean Phys. Soc.* **2009**, *55*, 1873–1876.

[210] M. Schulze, M. Lorenz, N. Wagner, E. Gülzow, *Fresenius. J. Anal. Chem.* **1999**, *365*, 106–113.

[211] E. A. Hoffmann, Z. A. Fekete, L. S. Korugic-Karasz, F. E. Karasz, E. Wilusz, *J. Polym. Sci. Part A Polym. Chem.* **2004**, *42*, 551–556.

[212] A. Kusoglu, A. Z. Weber, **2017**.

[213] N. Mannella, G. Gabetta, F. Parmigiani, *Appl. Phys. Lett.* **2001**, *79*, 4432–4434.

[214] D. J. Morgan, *C* **2021**, *7*, 51.

[215] J. Wu, W. Wang, Z. Wang, *Nanomaterials* **2020**, *10*, 1–16.

[216] N. Bellomo, **n.d.**

ELECTRONIC SOURCES

[a]https://ec.europa.eu/eurostat/databrowser/view/NRG_BAL_S__custom_1946578/bookmark/table?lang=en&bookmarkId=8760d5fb-bdbe-4cfe-9b79-c0dc3eaafe8f

[b] https://ec.europa.eu/commission/presscorner/detail/en/IP_22_4544